

DISSERTATION

**Third- and Fifth-order Nonlinear Time-resolved
Spectroscopies for Ultrafast Molecular Dynamics
in Carotenoids**

Takeshi Miki

INAUGURAL - DISSERTATION

zur
Erlangung der Doktorwürde
der
Naturwissenschaftlich-Mathematischen Gesamtfakultät
der
Ruprecht-Karls Universität Heidelberg

vorgelegt von
M. Sci. Takeshi Miki
aus Yamaguchi (Japan)

Heidelberg am Neckar 2017

Tag der mündlichen Prüfung: 23.06.17

Third- and Fifth-order Nonlinear Time-resolved Spectroscopies for Ultrafast Molecular Dynamics in Carotenoids

Gutachter:

Prof. Dr. Marcus Motzkus

Prof. Dr. Andreas Dreuw

Abstract

Multipulse optical technique is an essential tool on the direct observation of electron-nuclear motions responsible for various molecular properties. For example, light-energy harvesting or anti-oxidation, which flora and fauna have achieved along the course of evolution, are initiated by the molecular dynamics in conjugated hydrocarbons such as conjugated polyenes or porphyrin rings. In the case of the conjugated systems in photosynthetic pigments, a part of the dynamics has been revealed as an electronic-state dynamics. However, it is required to disentangle the remaining part of the molecular dynamics mainly consisting of the vibronic interactions induced by nuclear motions. In the scope of this thesis, the vibronic interactions between the electronic states having B_u or A_g symmetries in conjugated polyenes were detected by use of pump-probe and pump-degenerate four-wave mixing (DFWM) experiments. In addition, as an example of multimodal time-resolved spectroscopies, the combination of the two optical experiments was demonstrated to overcome analytical problems related to precision and accuracy of functional analysis for pump-probe spectra.

The significant influences of the vibronic interactions between the electronic states with A_g - A_g or B_u - B_u symmetries were observed by pump-DFWM experiments for a series of the conjugated polyenes having four different conjugated double bond length $N = 9, 10, 11$ and 13 . The frequency shifts of C–C (1100 cm^{-1}) and C=C (1500 cm^{-1} for B_u state, 1800 cm^{-1} for A_g states) stretching modes indicated the features and some difference of the two couplings. The coupling between A_g^- states appeared for all polyenes under the existence of the excited state with A_g symmetry. On the other hand, the coupling between B_u states only appeared for the polyenes with $N = 9$ and 10 , in which strong degeneracy of two B_u states can exist. In addition, solvent polarizability changed the coupling strength which was examined for lutein ($N = 9.5$) in three different solvents (hexane, THF and benzene). While the coupling appeared in hexane and in THF, it was absent in benzene since the degeneracy of the ionic B_u^+ state and covalent B_u^- state were very sensitive to solvent polarizability. The observation could be connected to environmental effects on the photosynthetic polyenes surrounded by proteins and lipids in photosynthetic apparatus.

In addition, an example of multimodal approach, which combines two different optical experiments, was demonstrated by the simultaneous analysis of a pair of data sets recorded by pump-probe and pump-DFWM experiments. This approach overcame conventional analytical problems of rotation ambiguity and local minimum in global target fitting. While the characterization of the relaxation model for rhodamine 6G was not uniquely done by global target fitting, the multimodal approach uniquely determined the appropriate kinetic model by the evaluation of four error functions. Moreover, the interpretation of the spectral and temporal elements were based on the response functions of pump-probe and pump-DFWM experiments.

The direct detection of vibronic coupling and the methodological development to disentangle the ultrafast molecular dynamics contributes to the investigation of nonadiabatic processes which is crucial to understand molecular properties.

Kurzzusammenfassung

Die Technik mit mehreren optischen Pulsen ist ein wesentliches Instrument zur direkten Beobachtung von Elektronen-Kern-Bewegungen, die für verschiedene molekulare Eigenschaften verantwortlich sind. Beispielsweise werden Licht Energy Harvesting oder Antioxidation, die Flora und Fauna im Laufe der Evolution erreichten, durch die Molekulardynamik in konjugierten Kohlenwasserstoffen wie konjugierten Polyenen oder Porphyrinringen initiiert. Im Falle konjugierter Systeme in photosynthetischen Pigmenten wurde ein Teil der Dynamik elektronischen Zuständen zugeordnet. Es ist jedoch erforderlich, den verbleibenden Teil molekularer Dynamik zu enthüllen, der hauptsächlich auf durch Kernbewegungen hervorgerufenen vibronischen Wechselwirkungen zurückzuführen ist. Im Rahmen dieser Arbeit wurden die vibronischen Wechselwirkungen zwischen elektronischen Zuständen mit B_u oder A_g Symmetrien in konjugierten Polyenen unter Verwendung von Pump-Probe und Pump-Degenerate Four-Wave Mixing (DFWM) Experimenten untersucht. Darüber hinaus wurde als Beispiel für multimodale zeitaufgelöste Spektroskopie die Kombination der beiden optischen Experimente gezeigt, um analytische Probleme im Zusammenhang mit Präzision und Genauigkeit der Funktionsanalyse für Pump-Probe-Spektren zu überwinden.

Die signifikanten Einflüsse der vibronischen Wechselwirkungen zwischen den elektronischen Zuständen mit A_g - A_g oder B_u - B_u Symmetrien wurden durch Pump-DFWM-Experimente für eine Reihe der konjugierten Polyene mit vier verschiedenen konjugierten Doppelbindungslängen $N = 9, 10, 11$ und 13 beobachtet. Die Frequenzverschiebungen von C-C (1100 cm^{-1}) und C = C (1500 cm^{-1} für den B_u Zustand, 1800 cm^{-1} für den A_g Zustand) Streckschwingungen zeigten die Merkmale und einen Unterschied der beiden Kopplungen an. Die Kopplung zwischen A_g Zuständen erschien für alle Polyene unter der Existenz des angeregten Zustands mit A_g Symmetrie. Auf der anderen Seite erschien die Kopplung zwischen B_u Zuständen nur für Polyene mit $N = 9$ und 10 , in denen starke Degeneration zwischen zwei B_u Zuständen existieren kann. Darüber hinaus änderte die Lösungsmittelpolarisierbarkeit die in drei verschiedenen Lösungsmitteln (Hexan, THF und Benzol) untersuchte Kopplungsstärke für Lutein ($N = 9,5$). Während die Kopplung in Hexan und THF auftrat, fehlte sie in Benzol, da die Degeneration des ionischen B_u^+ Zustandes und des kovalenten B_u^- Zustands sehr empfindlich gegenüber Lösungsmittelpolarisierbarkeit waren. Die Beobachtung könnte mit Umweltauswirkungen auf die photosynthetischen Polyene verbunden sein, die von Proteinen und Lipiden in photosynthetischen Apparaten umgeben sind.

Darüber hinaus wurde ein Beispiel eines multimodalen Ansatzes, der zwei verschiedene optische Experimente kombiniert, durch die gleichzeitige Analyse eines Paares von Datensätzen, die durch Pump-Probe und Pump-DFWM Experimente gemessen wurden, gezeigt. Dieser Ansatz überwand die konventionellen analytischen Probleme der Rotations-Ambiguität und des lokalen Minimums in der globalen Anpassung. Während die Charakterisierung des Relaxationsmodells für Rhodamin 6G durch eine globale Anpassung nicht eindeutig erfolgt, bestimmte der multimodale Ansatz durch die Auswertung von vier Fehlerfunktionen eindeutig das entsprechende kinetische Modell. Darüber hinaus basiert die Interpretation der spektralen und zeitlichen Elemente auf den Reaktionsfunktionen von Pump-Probe und Pump-DFWM Experimenten.

Die direkte Beobachtung der vibronischen Kopplung und die methodische Entwicklung, um ultraschnelle Molekulardynamik aufzudecken, trägt zur Untersuchung von nichtadiabatischen Prozessen bei, die für das Verständnis molekularer Eigenschaften entscheidend sind.

Contents

1	Introduction	1
2	Material and Experimental Methods	5
2.1	Carotenoids	5
2.1.1	Functions of Carotenoids	
2.1.2	Structural and Spectroscopic Features	
2.1.3	Geometrical Symmetries and Energy Levels	
2.1.4	Excited-state Dynamics and Energy Transfer	
2.2	Nonlinear Time-resolved Spectroscopies	11
2.2.1	Pump-probe and Pump-DFWM Experiments	
2.2.2	Phase Matching Condition	
2.2.3	Response Functions for Pump-probe and Pump-DFWM Experiments	
2.3	Functional Analysis for Time-resolved Spectra	17
2.3.1	Decomposition of Spectral Data	
2.3.2	Coefficient Matrix (C-matrix)	
2.3.3	Rate Equations	
2.3.4	Error Functions	
2.3.5	Relationship between Rotation Ambiguity and Precision	
2.3.6	Multimodal Approach	
3	Detecting Vibronic Coupling by Pump-probe and Pump-DFWM Experiments	25
3.1	Introduction	25
3.2	Experimental Methods	27
3.2.1	Extraction and Purification of Carotenoids	
3.2.2	Pump-probe and Pump-DFWM Experiments	
3.3	Results and Discussion	30
3.3.1	Pump-DFWM Transients at Four Detection Wavelengths	
3.3.2	Ultrafast Molecular Dynamics in the Carotenoids ($N = 9, 10, 11$ and 13)	
3.3.3	Time Evolution of Vibrational Frequencies	
3.3.4	Effect of Overlapping Contributions on the Evolution of Frequencies	
3.3.5	Vibronic Effects on Degenerate Energy Levels	
3.3.6	Vibronic Coupling Enhanced via Solvation	
3.4	Conclusions	43

4	Combination of Pump-probe and Pump-DFWM Experiments by Functional Analysis	45
4.1	Introduction	45
4.2	Experimental Methods	47
4.2.1	Pump-probe and Pump-DFWM Experiments	
4.2.2	Data Analysis	
4.3	Results and Discussion	48
4.3.1	TA spectra and Pump-DFWM Signals of Rhodamine 6G	
4.3.2	Singular Value Decomposition (SVD)	
4.3.3	Functional Analysis and Ambiguities	
4.3.4	Error Function in Multimodal TRS	
4.2.5	Multimodal TRS for Rhodamine 6G	
4.4	Conclusions	62
5	Summary and Outlook	63
5.1	Summary	63
5.1.1	Time-resolved Spectroscopies on the Femtosecond Timescale	
5.1.2	Vibronic Effects in the Poylenes with $N = 9, 10, 11$ and 13	
5.1.3	Multimodal Approach for Ultrafast Molecular Dynamics	
5.2	Outlook	65
5.2.1	Functions of Vibronic Coupling in Photosynthetic Polyenes	
5.2.2	Multimodal Approach	
	Appendix	67
Appendix A.	Symmetrical Operators and Symmetry of Molecular Orbital	
Appendix B.	Theoretical Description for Pump-probe and Pump-DFWM Experiments	
Appendix C.	Density Matrix and Time Evolution Operator	
Appendix D.	Intermediate Equations for the Response Functions	
Appendix E.	Rate Equations	
Appendix F.	Adiabatic Approximation	
Appendix G.	Nonadiabatic Process	
Appendix H.	Hellmann-Feynman Theorem for Electronic Hamiltonian	
	References	92
	Acknowledgement	98

Chapter 1

Introduction

Many kinds of molecular properties and reactions are initiated by the structural changes induced by the excitation of molecules. Such ultrafast nuclear motions occur even within a picosecond timescale.¹⁻⁵ Hence, a thorough understanding of the ultrafast molecular dynamics is indispensable for describing the mechanisms behind molecular properties. In order to probe ultrafast electron-nuclear motion, many kinds of optical techniques and theoretical frameworks have been developed in the last century. Especially, evolution from pure steady state methods to time-resolved methods was achieved by the introduction of pulsed light sources, typically pulsed lasers with Q-switching or mode locking.⁶⁻⁸ Moreover, the development of pulsed laser sources that can produce optical pulses from ~100's ps, e.g. from pulsed laser diodes, to as short as ~50 as using high harmonic generation has permitted the direct observation of electronic and vibrational state interactions.⁹⁻¹² In general, many molecular dynamics studies have been utilized such femtosecond methodologies, based on titanium-sapphire technologies.¹³

From the data obtained, the observed behavior has been usually explained in the framework of adiabatic approximation^{14,15}, in which electron-nuclear motion is described by dynamically separated vibrational and electronic states while the interactions between electronic states induced by nuclear motion are ignored. However, in order to reveal the electron-nuclear motions accurately, such interactions have a significant importance especially for electronic-state dynamics, which readily occur on a femtosecond timescale or at a conical intersection.¹⁶⁻¹⁹ Since the effects induced by nuclear motion are ignored in adiabatic approximation, adiabatic energy levels, a product of an electronic and a nuclear wavefunction, are not enough to describe the interactions evoked by nuclear motion.* As a result, the effects are usually called *vibronic* (*v*ibronal + *e*lectronic) effects. Many ideas to describe such nonadiabatic processes have been suggested during the last 40 years for various kinds of the quantum systems. For example, the significant nonadiabatic effects appearing on the stationary absorption spectrum were explained for the butatriene by use of the comparison between the observation and the calculations with/without the nonadiabatic effects.¹⁶ On the other hand, in the case of the polyenes having the number of the conjugated double bonds $N > 4$, the nonadiabatic effects have been partially revealed between an excited state and the ground state.²⁰⁻²³ For example, polyenes that contain conjugation lengths of $N > 5$, where N is the number of conjugated double bonds, electronic states with A_g^- symmetry may undergo strong coupling due to the C=C (A_g) stretching modes.²²⁻²⁴ Such vibronic effects lead to the modification not only of the potential energies but also of the vibrational frequencies. However, it is still difficult to examine the interactions between short-lived excited states (< 1 ps), while such dynamics could be crucial for molecular properties and reactions. As a result, the unrevealed dynamics on the short-lived excited states in polyenes has caused a huge argue about the existence of some optically-dark electronic states.²⁵⁻²⁸ Since every kind of reaction usually occurs with a nuclear rearrangement, disentanglement of nonadiabatic effects, usually performed by time-resolved optical experiments, is required to reveal accurate molecular mechanisms.

* Recently, some literature introduced a new framework to describe the exact molecular wavefunctions as a product of an electronic and a nuclear wavefunction.^{29,30} In this work, we employed the theoretical framework based on the conventional adiabatic approximations discussed in Appendix F to define the meanings of the words.

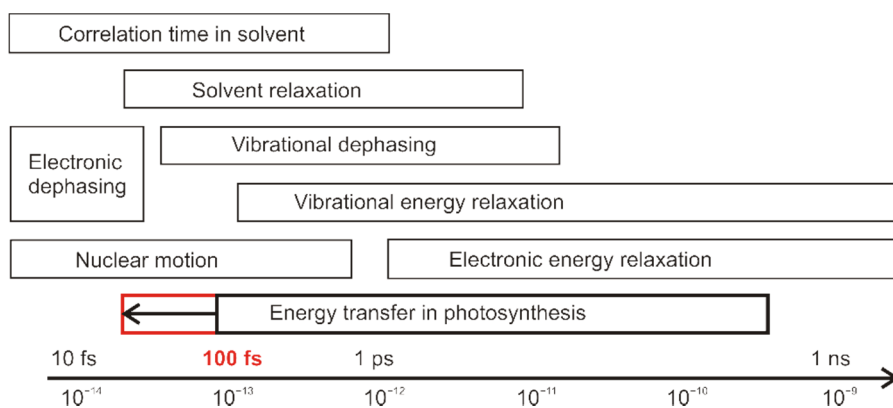


Figure 1.1: Ultrafast phenomena with relevant timescale.² As an improvement of the time resolution of experimental techniques, ultrafast phenomena occurring below 100 fs have been intensively investigated for some molecular dynamics such as photosynthetic mechanisms.³¹⁻³⁴

When dealing with studies involving time-resolved spectroscopy in the femtosecond timescale there are various issues, but two of particular relevance that we shall highlight: (i) breakdown of the adiabatic approximation^{17,18} and (ii) strong overlap between the signals that contribute to the measured data. The first point we have already mentioned in the previous paragraph. To reiterate, the adiabatic approximation is the basic idea that allows us to consider the electron and nuclear wavefunctions separately.³⁵ Much of the research performed in the picosecond timescale employs the adiabatic approximation to interpret molecular dynamics, as the picosecond timescale mainly consists of electronic and vibrational energy relaxations (Figure 1.1).³⁶⁻³⁸ On the other hand, the femtosecond dynamics contain many additional phenomena, one of which is the nuclear motions that couple to the molecular orbital dynamics. While their time evolutions can be ignored at the picosecond level their contribution becomes too significant at the femtosecond level. Regarding the second point mentioned, decomposition of the overlapping signals, this is more challenging at the femtosecond regime due to the existence of additional physical phenomena such as solute-solvent or intramolecular interactions.^{39,40} The serious mathematical complexity in the data obtained using simpler time-resolved methods has led to the development of more sophisticated analytical tools, and also the introduction of more complicated experimental techniques that look to produce cleaner, less convoluted data. For example, many kinds of multi-dimensional vibrational spectroscopies have been developed to show specific features in femtosecond molecular dynamics, although they inherently introduce some disadvantages at the same time.

In regards to the problems outlined previously, many approaches to disentangle nonadiabatic effects and to control them by use of optical experiments have been introduced. Much of these techniques are grouped into 3rd-order or 5th-order nonlinear time-resolved spectroscopies.⁴¹⁻⁴⁵ For example, the pump-probe experiment, which is a kind of the 3rd-order nonlinear optical spectroscopies (four-wave mixing), can basically observe population dynamics of excited states in addition to the nuclear motions appearing as wavepacket motion.⁴⁶ The optical technique can effectively record molecular dynamics as a series of absorption and emission spectra as a function of pump-probe pulse delay time. Note that the pump-probe delay time is variable and is equivalent to the timescale of (photo)reaction progression (Figure 1.2) while it is convoluted with an instrumental response function. The acquired spectra contains a variety of information, including but not limited to the transient dipole of the relevant energy levels. In addition, the spectral analysis is often based on functional analysis in which the spectra are decomposed and reconstituted with the simultaneous fittings of possible kinetic models (Figure 1.2). Consequently, it is a technique often used to evaluate population dynamics described by the adiabatic energy levels. On the other hand, pump-degenerate four-wave mixing

(DFWM) experiment, which is a kind of the 5th-order nonlinear optical experiment (six-wave mixing), can disentangle the wavepacket motion in more detail by the direct observation of vibrational and vibronic coherences during the population relaxation.^{42,47,48} Especially in the femtosecond timescale, the time evolution of the vibrational frequencies could contain the coupling effects between some short-lived electronic states. Therefore, the vibrational spectroscopy is a sophisticated tool to disentangle the nonadiabatic effects. In general, such advantages of the optical spectroscopies are always accompanied with some disadvantages compared with the other techniques. Due to there being no “one best method”, we suggest a combination of two complementary time-resolved spectroscopies to disentangle ultrafast dynamics. The two that we choose to focus on are the pump-probe methodology and pump-DFWM. The experimental results obtained in both optical techniques can be examined by the use of functional analyses.

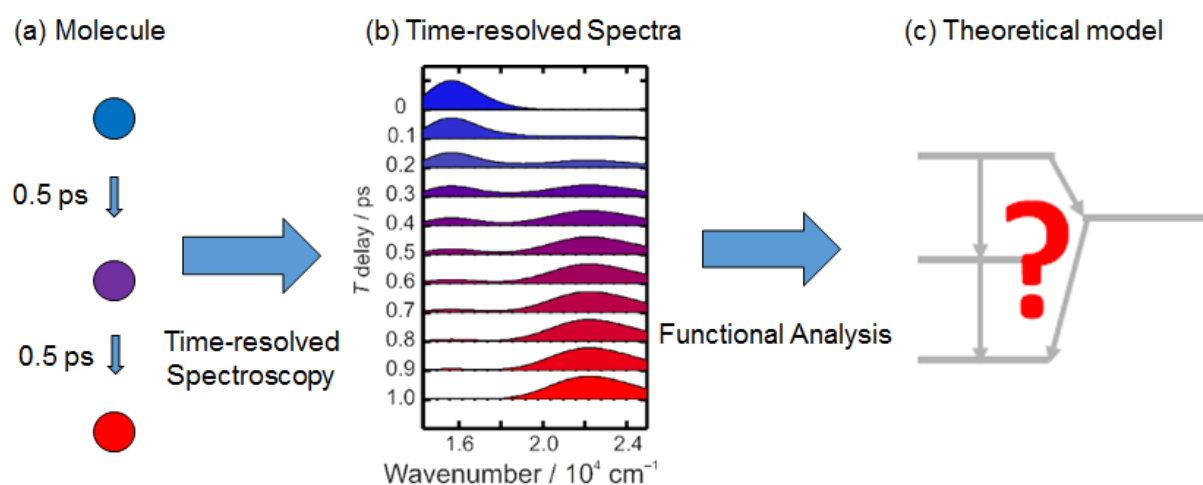


Figure 1.2: Framework of the research to reveal ultrafast molecular dynamics by use of time-resolved spectroscopy. Molecular dynamics such as (a) the color changing of molecule is observed by some spectroscopies as (b) a series of transient spectra. The interpretation of the spectral data is determined by the comparison between theoretical model and decomposed spectral data usually through functional analysis.

The work within this thesis is centered on the use of pump-probe and pump-DFWM experiments, to detect the ultrafast molecular dynamics of photosynthetic polyenes. In particular, we focused on the vibronic coupling and the experimental issues originated from the interaction between the polyene electronic states. Since the two optical techniques can observe molecular dynamics from different aspects, it is possible to improve conventional analytical method by use of the advantages of the two experiments. An example of the new approach, which we refer to as multimodal time-resolved spectroscopy, has led to a new means to decompose and reconstitute a pair of spectral data sets observed by both pump-probe and pump-DFWM experiments. Chapter 2 introduces the background material needed to understand the polyenes, also known as carotenoids, used in the experiments. Additionally, a thorough account of the theoretical description behind the high order processes involved in pump-probe and pump-DFWM is also given. The final part of chapter 2 is an in depth explanation of what functional analysis is, and how it is used in the analysis of the time-resolved data. The principles behind the multimodal time-resolved spectroscopy that was developed are explained in brief in chapter 2. Moving to the results of the thesis, chapter 3 evaluates the ultrafast relaxation of quasi-degenerated coupled potential surfaces in a series of carotenoids by use of pump-DFWM. We show that by changing solvent polarizabilities, one can change the degeneracy of the potential surfaces, which leads to modification of

the coupling effects that only appear at very early times (< 100 fs). In chapter 5, we demonstrate the power of combining pump-probe and pump-DFWM experiments by functional analysis. The new approach we have designed decomposes the signals observed in two complementary time-resolved spectroscopies simultaneously. The combination of 3rd-order and 5th-order nonlinear spectroscopies with simultaneous data analysis allows one to acquire a less ambiguous solution with the spectral elements described by the light-matter interactions commonly observed in the two optical experiments. Finally, chapter 6 concludes the research which was undertaken and explores future work and outlooks.

Chapter 2

Materials and Experimental Methods

In this thesis, ultrafast photochemical reactions occurring in degenerate energy levels is investigated by pump-probe and pump-Degenerate Four-Wave Mixing (DFWM) experiments.⁴⁷ A series of carotenoids having unique degenerate excited states^{28,49} was employed in order to detect vibronic couplings between the electronic states of B_u^+ , B_u^- or A_g^- symmetries. In addition, rhodamine 6G, having a well-known two-state system in the visible wavelengths,⁵⁰⁻⁵² was used as an example to examine the appearance of vibrational and vibronic coherence in each optical technique and functional analysis. The spectral data were analyzed by functional analysis⁵³⁻⁵⁸ which decompose and reconstitute spectra based on some appropriate theoretical model. Regarding the background and experimental methods, this chapter has three sections for Carotenoids 2.1, Nonlinear Time-resolved Spectroscopies 2.2 and Functional Analysis 2.3.

2.1 Carotenoids

2.1.1 Functions of Carotenoids

Carotenoids are naturally occurring polyenes having two essential roles in photosynthesis: light energy harvesting and photoprotection.^{34,59} In the early stage of photosynthesis, light absorption through chlorophylls is accompanied by light absorption through carotenoids. In many plants and bacteria, carotenoids serve as accessory light-harvesting pigments in the visible region where chlorophylls cannot effectively work. The energy absorbed by carotenoids are transferred to chlorophylls in the form of electronic singlet excitations.^{60,61} On the other hand, carotenoids can be a main light absorber in some case such as the pigment-protein complex extracted from *Amphidinium carterae* (a species of dinoflagellate)⁶². Thus, the carotenoids are indispensable elements in the light energy harvesting. In the photoprotection, they prevent photodestruction in photosynthetic apparatus *via* quenching of chlorophyll triplet states, singlet oxygen scavenging or excess energy dissipation through the singlet internal conversion processes.⁶³⁻⁶⁶ In addition, they are beneficial for living organisms as antioxidants⁶⁷ or as a source of vitamins derived from carotenoids with a β -ring. Due to the important features of carotenoids, P. Karrer and R. Kuhn received Nobel Prize in 1937 and 1938, respectively. P. Karrer determined the correct constitutional formula for β -carotene, and it was the first time that the structure of a vitamin or provitamin had been established. The chromophores possess low-lying $\pi\pi^*$ electronic transitions whose energies and oscillator strengths are sensitive to substituents and to interactions with proteins. In spite of the intense research, their electronic structure and nuclear dynamics still remain uncertain.

2.1.2 Structural and Spectroscopic Features

The diverse functions of carotenoids derive from their molecular structure and electronic properties. They have a conjugated π -system of C=C double bonds in all-*trans* configuration as shown in Figure 2.1. The conjugated π -electron system is responsible for most of the spectroscopic properties of carotenoids. For example, the highly delocalized electrons in carotenoids lead to its strong yellow-red colors of the pigments. The longer the conjugation of double bonds of the polyene backbone, or in

other words the more delocalized the electrons are, the longer the wavelength at which light is absorbed. Figure 2.2 shows the absorption spectra of carotenoids and the bathochromic shift induced by the delocalization of π -electron on the conjugated chain. Carotenoids can absorb radiation in the visible region where chlorophyll is not an efficient absorber. Therefore, the shorter-chain carotenoids are selectively bound to LH2 antenna complexes for the light-harvesting function. On the other hand, the delocalized electrons in longer-chain carotenoids make them quite suitable for photoprotection by physically quenching singlet oxygen or even by chemical reactions^{59,68}. In addition, depending on the degree of substitution, the terminal rings can also strongly influence the overall properties of the carotenoids as previously seen in *Amphidinium carterae* (the pigment-protein complex of the dinoflagellate contains peridinin which have a significantly high efficiency of energy transfer due to their end group)⁶².

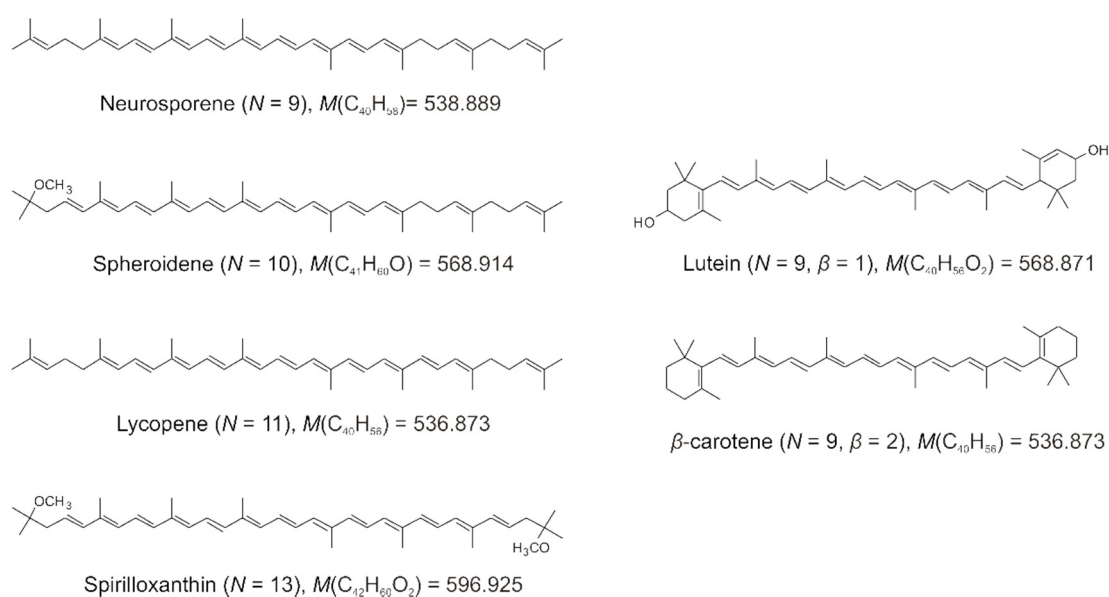


Figure 2.1: Molecular structures of carotenoids with the conjugation length $N = 9 - 13$. The parameter, β , refers to the conjugation extended to a terminal ring.

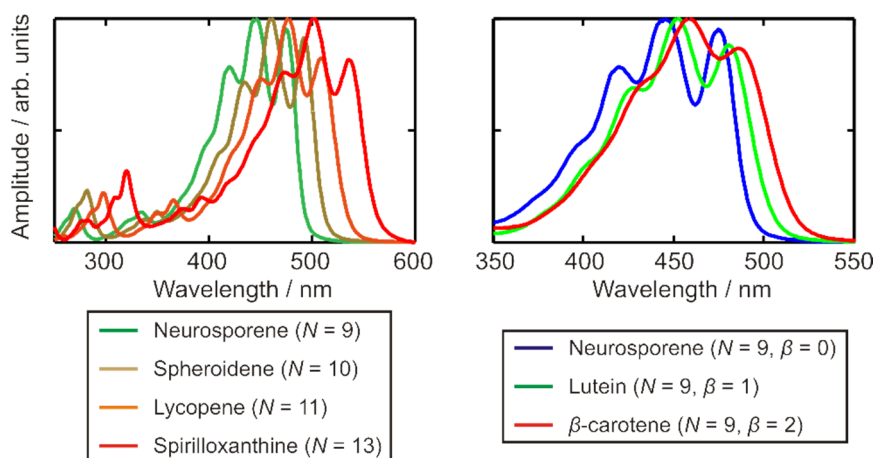


Figure 2.2: Absorption spectra of carotenoids for $N = 9 - 13$. The higher the conjugation length N becomes, the more the spectra shift to the red.

The vibronic structure of absorption or emission spectra is usually governed by progressions of totally symmetric vibrations (Franck-Condon progressions¹⁶).⁶⁹ In the series of carotenoids shown in Figure 2.2, the vibronic structure is formed by two totally symmetric modes, the prominent C=C stretch ($\sim 1500\text{ cm}^{-1}$) and a slightly less active C-C stretch ($\sim 1100\text{ cm}^{-1}$).^{70,71} Their activity results from changes in carbon-carbon bond lengths upon electronic excitation. Raman spectroscopies are often used to observe structural rearrangements in carotenoids since the two modes are strongly active in the Raman spectra.^{72,73}

2.1.3 Geometrical Symmetries and Energy Levels

The electronic states of all-*trans* carotenoids are usually described by the geometrical features of the π -electron conjugated systems with C_{2h} symmetry. The molecular orbitals of polyenes follow the four symmetry rules (E, C_2 , i and σ_h) of C_{2h} symmetrical point group. Taking *trans*-2-butene as an example of a simple polyene with C_{2h} symmetry, they have molecular orbitals with the symmetrical labels as shown in Figure 2.3. Depending on the combination of the symmetry elements, the molecular orbitals are described by the four irreducible representations of A_g , A_u , B_g and B_u (Appendix A contains more detailed information). The capital letter used, 'A' or 'B', distinguishes symmetric or antisymmetric response of the orbital with respect to a C_2 operation. Moreover, the subscripts of 'g' (gerade) and 'u' (ungerade) refer to symmetric and antisymmetric response to an inversion operation. The symmetry labels adequately describe wavefunctions of double occupancy (two electron present) for *trans*-2-butene as shown in Figure 2.3b.

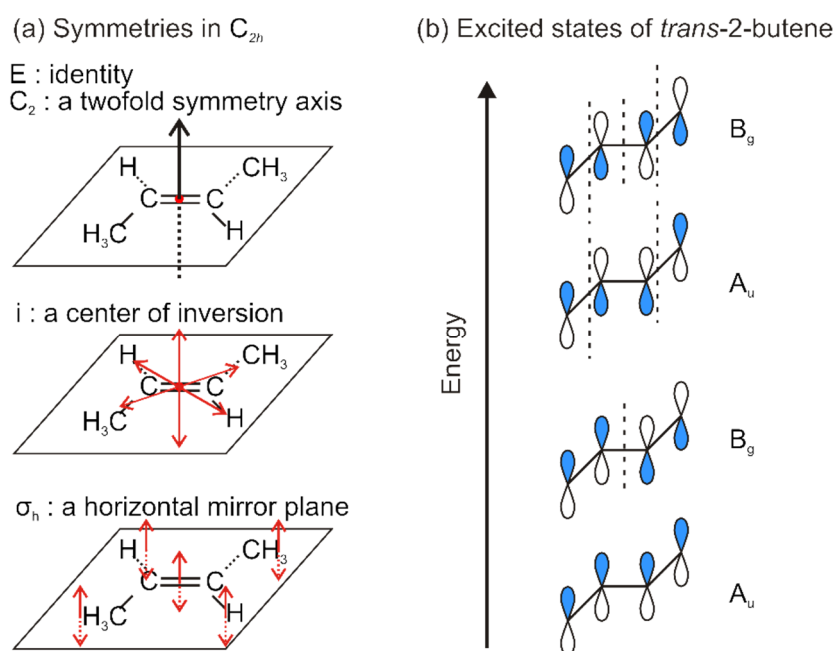


Figure 2.3: (a) The C_{2h} point group contains four symmetry elements: the identity operator (E), twofold symmetry axis (C_2), center of inversion (i) and a horizontal mirror plane (σ_h). (b) The molecular orbitals of *trans*-2-butene (C_{2h}) are labeled according to the symmetry properties as belonging to one of the four irreducible representation (A_g , A_u , B_g , B_u) of the C_{2h} point group.

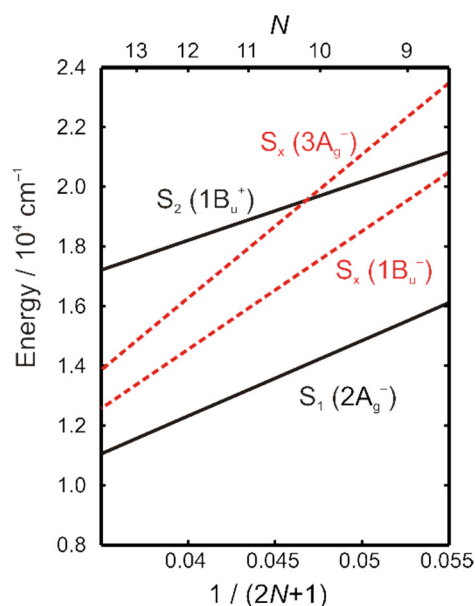


Figure 2.4: Energy diagram for polyenes with $N = 9 - 13$. Dependence of the energies of carotenoid excited states on conjugation length are shown. The energies of the S_1 and S_x states were firstly expected by the calculation⁷⁴ and later experimentally proved by resonance-Raman excitation profiles⁷⁵. The energies of the S_2 state are obtained from absorption spectra of each carotenoid in THF solution.

Interestingly, the order of the electronic states has a strong dependence on the polyene chain length. Usually, they are aligned in a specific order of alternating parity (even, odd, even, odd...) with increasing energy and nodes. However, due to strong electronic correlation in the π -electron conjugated systems, polyenes with $N > 5$ have ‘reverse’ ordering of the excited states, which is a central feature of naturally occurring carotenoids^{76,77}.

The first example of the unusual structure of electronic states was revealed in 1972.^{20,78} Theory and experiment indicated that the $2A_g^-$ state lies below the $1B_u^+$ state for α,ω -diphenyloctatetraene. Later, Tavan and Schulten theoretically indicated the presence of $1B_u^+$, $3A_g^-$, $1B_u^-$ and $2A_g^-$ states and their energies as linear function of $1/(2N+1)$ for the polyene with $N = 5 - 8$ ^{74,76}. For the carotenoids with $N = 9 - 13$, the energies of the singlet excited states are determined by measurement of resonance-Raman excitation profiles as shown in Figure 2.4⁷⁵.

In Figure 2.4, all of the carotenoids with $N = 9 - 13$ have a high-lying optically-allowed S_2 ($1B_u^+$) state, a low-lying optically-forbidden S_1 ($2A_g^-$), and S_x ($1B_u^-$ and $3A_g^-$) states with respect to the transitions from/to the ground S_0 ($1A_g^-$) state^{79,80}. Here, each states carry ‘+’ and ‘-’ superscripts which denotes the pseudoparity character (even “+” or odd “-” against inversion operation) of the electronic configuration⁷⁹. The number in front of the symmetry symbols indicates the order of the each type of electronic states from the lowest to the higher energies. Here, to avoid ambiguity and confusion in the assignment, the traditional state designations $S_2(1B_u^+)$, $S_1(2A_g^-)$, $S_0(1A_g^-)$ and $S_x(1B_u^-$ and $3A_g^-)$ will be used for singlet excited states.

2.1.4 Excited-state Dynamics and Energy Transfer

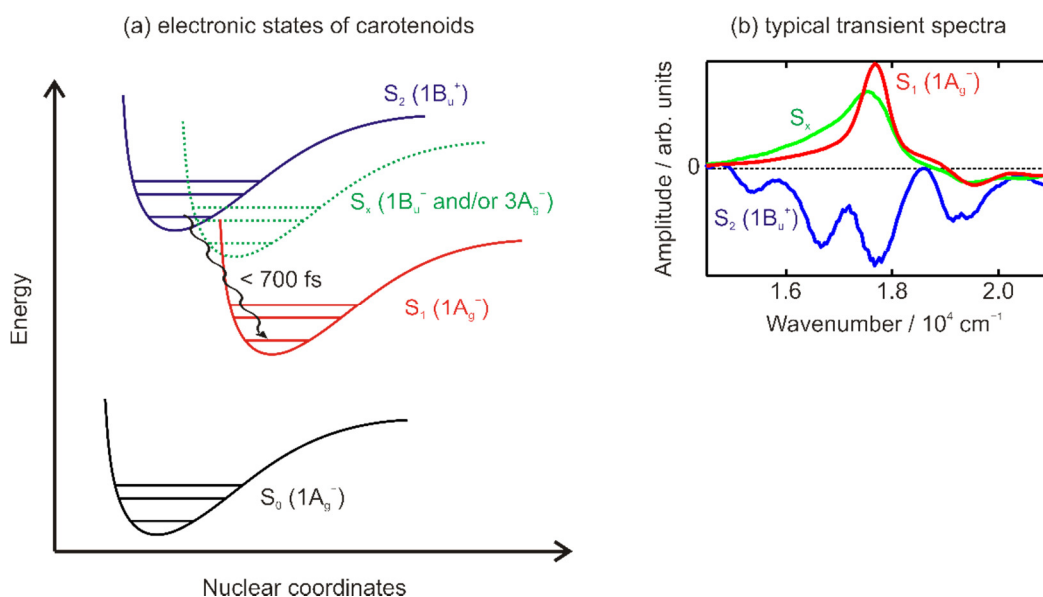


Figure 2.5: (a) The electronic states of carotenoids for $N \geq 9$. (b) Typical transient spectra of the S_2 , S_x and S_1 states of lycopene observed by pump-probe experiment.

In order to increase our understanding of the function of carotenoids in photosynthesis, it is of prime interest to study the kinetic behavior of their excited states. The deactivation following photoexcitation of carotenoids for $N = 9 - 13$ always go through the singlet internal-conversion process of $S_2 \rightarrow S_1 \rightarrow S_0$ as shown in Figure 2.5.⁸¹⁻⁸³ Since the relaxation to $S_1 (2A_g^-)$ after photo excitation to the $S_2 (1B_u^+)$ state occurs in a very short timescale (< 700 fs), there is still huge argue about the detail mechanism between S_2 and S_1 states. The S_1 state is observed as an absorption signal of $S_1 \rightarrow S_N$ transition (Figure 2.5b) in pump-probe experiment in the visible wavelength region⁸⁴. The $S_1 (2A_g^-)$ state deactivates back to ground state as the excited-state absorption disappears. The lifetime of the excited states of carotenoids have strong dependence on their conjugation length; the longer the conjugation length becomes, the faster the relaxation occurs.³ Such feature of the electronic states in carotenoids are often related to their functions.

In light harvesting complexes, the radiationless decay of the S_1 state is a primary process which competes with the singlet energy transfer to Q_y state of chlorophyll as shown in Figure 2.6. The lifetime of the S_1 state (donor) determines the transfer efficiency; the faster the relaxation on S_1 state occurs, the lower the energy transfer efficiency becomes.³ In addition, the energy transfer rates have a quadratically dependence on the electronic coupling and linearly on the spectral overlap between the relevant states of carotenoids and chlorophylls.³² The overall transfer efficiencies for Car \rightarrow Chl transfer have been measured by fluorescence excitation spectroscopy, showing a variability between different species and light-harvesting complexes. According to the literature³, the transfer efficiency is 88 % in *Rhodobacter sphaeroides* G1C (neurosporene, $N = 9$), 84 % in *Rhodobacter Sphaeroides* 2.4.1 (spheroidene, $N = 10$) and ~ 50 % for *Rhodospirillum molischianum* (lycopene and rhodopsin, $N = 11$) and *Rhodopseudomonas acidophila* (Rhodopin glucoside, $N = 11$). The energy transfer efficiency drastically decreases for the polyenes with $N = 11$ ($\eta \sim 50$ %) compared with shorter-chain polyene $N = 10$ ($\eta \sim 90$ %), which cannot be explained only by the kinetic behavior of S_1 state.

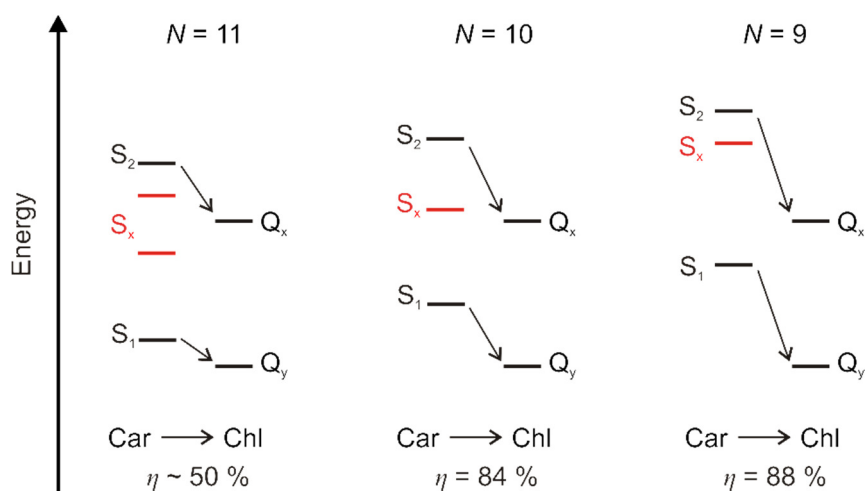


Figure 2.6: Energy transfer efficiency (η) from carotenoids to (bacterio)chlorophyll in LH2 antenna complex. In literature³, the singlet excitation energy transfer through two pathways ($S_2 \rightarrow Q_x$ and $S_1 \rightarrow Q_y$) were shown.

As alluded to earlier in Figure 2.4, it has been proposed that the spectroscopic properties and relaxation dynamics of carotenoids are affected by the presence of additional low-lying excited states (S_x) residing between S_1 ($2A_g^-$) and S_2 ($1B_u^+$) states. While there is still huge argue about the kinetic behavior of the S_x ($1B_u^-$ and $3A_g^-$) states, it is suggested that the $1B_u^-$ state for the polyene with $N = 9$ and 10 stays energetically above the Q_x state of chlorophylls.^{36,38,74} Therefore, how S_x states evolve in time and how they participate as a donor in the energy transfer process are central to understanding the molecular properties. To reveal such ultrafast phenomena, nonlinear time-resolved spectroscopies are usually employed.

2.2 Nonlinear Time-resolved Spectroscopies

The time-dependent photophysical and photochemical properties of molecules are usually tracked by multi-pulse optical experiments typically called nonlinear spectroscopy. Each optical technique has different features originated from the geometrical design of the specific pulse sequence. Some techniques can effectively and accurately determine molecular dynamics within adiabatic approximation, but other technique is suitable to detect the interaction between electronic states (nonadiabatic process). In fs timescale, while it is possible to detect nuclear motion directly, the population dynamics is often accompanied with vibronic interaction induced by nuclear motion. Thus, in nonlinear time-resolved spectroscopies, characterization of optical signals has been intensively investigated till achieving the theoretical description for the optical experiments.⁴¹ In this section, two nonlinear spectroscopic signals, pump-probe and pump-DFWM experiments, are introduced as a tool to disentangle adiabatic and nonadiabatic processes.

2.2.1 Pump-probe and Pump-DFWM Experiments

The pump-probe and pump-DFWM experiments are well-known as a kind of four-wave mixing or six-wave mixing spectroscopies, respectively. The major part of the signal in each technique is described by unified principles described in literature^{41,46,85}. The two techniques have pulse sequences shown in Figure 2.7. It is important to note that the number of the pulses in the experiments and the number of the light-matter interactions to generate signals are not exactly the same in some case. When we carefully see the momentum conservation in pump-probe experiment, there must be two interactions of the pump pulse and one interaction of a probe pulse to gain the signal collinear with probe pulse. Thus, the 3rd-order nonlinear optical susceptibility is mainly observed in pump-probe experiment (although there can be 5th-, 7th- or much higher-order nonlinear responses as minor contributions). On the other hand, five interactions are required in the momentum conservation of pump-DFWM experiment. Thus, pump-DFWM experiment is a kind of 5th-order nonlinear spectroscopy. The geometry of the pulses has significant importance in time-resolved spectroscopies.

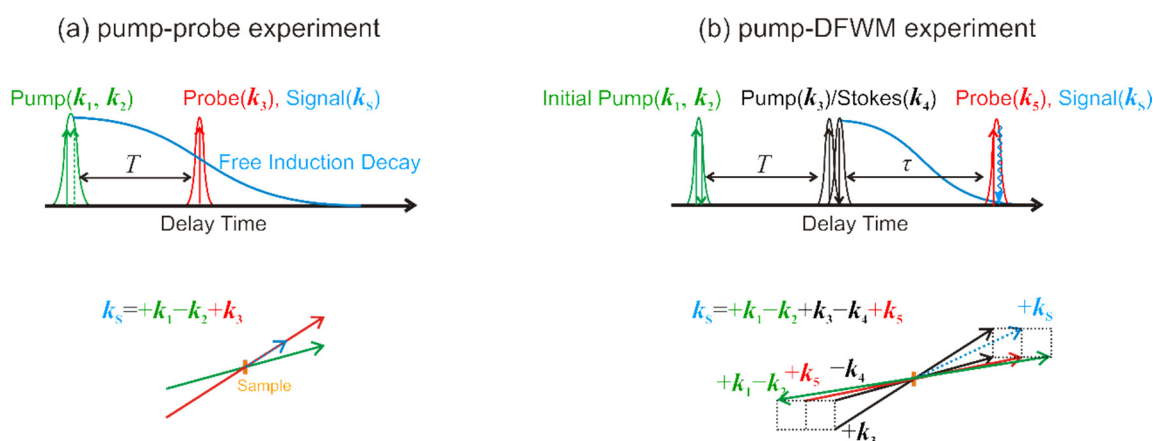


Figure 2.7: Pulse sequence for (a) pump-probe and (b) pump-DFWM experiments. The geometry of the pulses is expressed by the vectors for each electric field.

The coherence is induced by the synchronization of coherent oscillations in quantum states with external electric field. In pump-probe and pump-DFWM experiments, dephasing of the coherence, often referred as free induction decay (FID) as shown in Figure 2.7, is detected at the femtosecond level. The coherent emission usually decays exponentially at the dephasing rate in pure dephasing process. However, since dephasing is often accompanied with nuclear rearrangement, FID observed in ultrafast time-resolved spectroscopies contains much information not only about population dynamics but also about the interactions between electronic states. Obviously, the interaction becomes stronger when nuclear rearrangement changes rapidly at the crossing point of two electronic states. Thus, it is often challenging to determine ultrafast dynamics having many electronic states.

2.2.2 Phase Matching Condition

The experimental beam geometry and pulse sequence, often referred as phase matching condition, play a central role in time-resolved spectroscopies. By carefully designing of the phase matching in a given experiment, one can select specific signals. Many kinds of geometries were already carried out and reported in literature⁴¹. For example, pump-probe and pump-DFWM experiments have phasing matching condition with $k_s = k_1 - k_2 + k_3$ and $k_s = k_1 - k_2 + k_3 - k_4 + k_5$, respectively, as shown in Figure 2.8. The observed signal (k_s) always appears at the certain direction which is determined by the compensation of the relevant vectors as shown in the bottom panels. In other words, the signal observed at the position is only generated by the combination of the interactions of electric fields. The series of interactions of each electric field are often used for the interpretation of the spectral data as shown in 2.2.3.

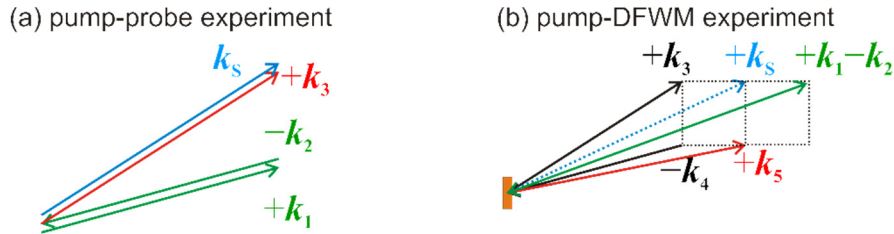


Figure 2.8: Phase matching conditions of (a) pump-probe and (b) pump-DFWM experiments. The pump-DFWM experiment has a BOXCARS geometry in the four-wave mixing sequence (k_3 , k_4 and k_5).

The intensity of optical signals is also determined by phase matching condition and detection method. For example, in pump-probe experiments, the 3rd-order nonlinear signals appear in the same direction with probe pulse. Thus, the signals are overlapped and detected together with the intensity of the probe pulse by self-heterodyne detection. Therefore, the intensity of the signal is enhanced as $|E^{(3)} + E_{pr}|^2$. On the other hand, in pump-DFWM experiment, the signal is observed by background-free homodyne detection which gives rise to the signal intensity of $|E^{(5)}|^2$.⁴⁷

2.2.3 Response Functions for Pump-probe and Pump-DFWM Experiments

The observables in optical experiments are often expressed as a set of response functions which contains the patterns of the interactions between the density matrix and dipole operators. A comprehensive discussion on the different terms and details can be found in literature⁴¹. In this section, the response functions appearing in pump-probe and pump-DFWM experiments are selected for consideration.

In general, light-matter interaction is approximately described by optical polarizations⁴¹. The 3rd-order polarization, $P^{(3)}(\mathbf{x}, t)$, created by the electric fields, $E^{(3)}(\mathbf{x}, t, t_3, t_2, t_1)$, in pump-probe experiment has a set of 3rd-order response functions, $R^{(3)}(t_3, t_2, t_1)$, as shown in Eq. (1)-(4). Detailed information and intermediate equations are written in Appendix B. The time interval, t_n , between the relevant electric fields are defined as shown in Figure B.1 in Appendix B. As shown in Eq. (4), there are four response functions with their complex conjugates.

$$P^{(3)}(\mathbf{x}, t) = \int_0^\infty dt_3 \int_0^\infty dt_2 \int_0^\infty dt_1 R^{(3)}(t_3, t_2, t_1) E^{(3)}(\mathbf{x}, t, t_3, t_2, t_1) \quad , \quad (1)$$

where

$$R^{(3)}(t_3, t_2, t_1) = \left(\frac{i}{\hbar}\right)^3 \theta(t_1)\theta(t_2)\theta(t_3) \sum_{n=1}^4 [R_n^{(3)} - R_n^{(3)*}] \quad , \quad (2)$$

$$E^3(\mathbf{x}, t, t_3, t_2, t_1) = E(\mathbf{x}, t - t_3)E(\mathbf{x}, t - t_3 - t_2)E(\mathbf{x}, t - t_3 - t_2 - t_1) \quad , \quad (3)$$

$$\left. \begin{aligned} R_1^{(3)}(t_1, t_2, t_3) &= \text{Tr}[\mu U_0(t_3)\mu U_0(t_2)\mu U_0(t_1)\mu \hat{\rho} U_0^\dagger(t_1)U_0^\dagger(t_2)U_0^\dagger(t_3)] \\ R_2^{(3)}(t_1, t_2, t_3) &= \text{Tr}[\mu U_0(t_3)U_0(t_2)U_0(t_1)\mu \hat{\rho} U_0^\dagger(t_1)\mu U_0^\dagger(t_2)\mu U_0^\dagger(t_3)] \\ R_3^{(3)}(t_1, t_2, t_3) &= \text{Tr}[\mu U_0(t_3)U_0(t_2)\mu U_0(t_1)\hat{\rho}\mu U_0^\dagger(t_1)U_0^\dagger(t_2)\mu U_0^\dagger(t_3)] \\ R_4^{(3)}(t_1, t_2, t_3) &= \text{Tr}[\mu U_0(t_3)\mu U_0(t_2)U_0(t_1)\hat{\rho}\mu U_0^\dagger(t_1)\mu U_0^\dagger(t_2)U_0^\dagger(t_3)] \end{aligned} \right\} \quad (4)$$

where $\theta(t)$ is the Heaviside step function, $\hat{\mu}$ is the dipole operator, $\hat{U}(t, t_0)$ is the time evolution operator, $\hat{\rho}$ the density matrix, the Hermitian conjugate is defined as $|a\rangle^\dagger = \langle a|$. The sum of the trace elements given by four response functions $R_1^{(3)} \sim R_4^{(3)}$ with their complex conjugates and the electric fields constitute the 3rd-order polarization. Each term contains a different sequence of the dipole interactions as seen in Eq. (4). For example, the dipole interactions induced by the external electric field, k_1, k_2 , and k_3 , in $R_1^{(3)}$ have the sequence: ket interaction (k_1) \rightarrow time evolution t_1 \rightarrow ket interaction (k_2) \rightarrow time evolution t_2 \rightarrow ket interaction (k_3) \rightarrow time evolution t_3 \rightarrow signal. The signal decays with the dephasing processes containing population and vibrational contributions. The dephasings observed in each response function are created by the sequence of the dipole interactions to the density matrix. To visualize the observable coherence, dipole interactions and time evolutions applied to the density matrix are typically described by the double-sided Feynman diagram (Figure B.2 in Appendix B). Each term in the diagram is equivalent with the term shown in Eq. (4). It is very convenient to use the diagram to determine the observable signals for each experimental condition.

The observable coherence are determined by experimental condition and the interaction sequences shown in Eq. (4). For example, in pump-probe experiment where $k_{IP} = k_1 = k_2$ and the signal is observed at $k_s = k_1 - k_2 + k_3$ (or $k_s = -k_1 + k_2 + k_3$), there are contributions from excited-state absorption (ESA) pathway, excited-state emission (ESE) pathway, and ground-state bleaching (GSB) pathway. The coherence observed in pump-probe experiment is the superposition of the contributions. More detail information about the evaluation of the response functions is given in literature^{41,85} and Appendix B.4.

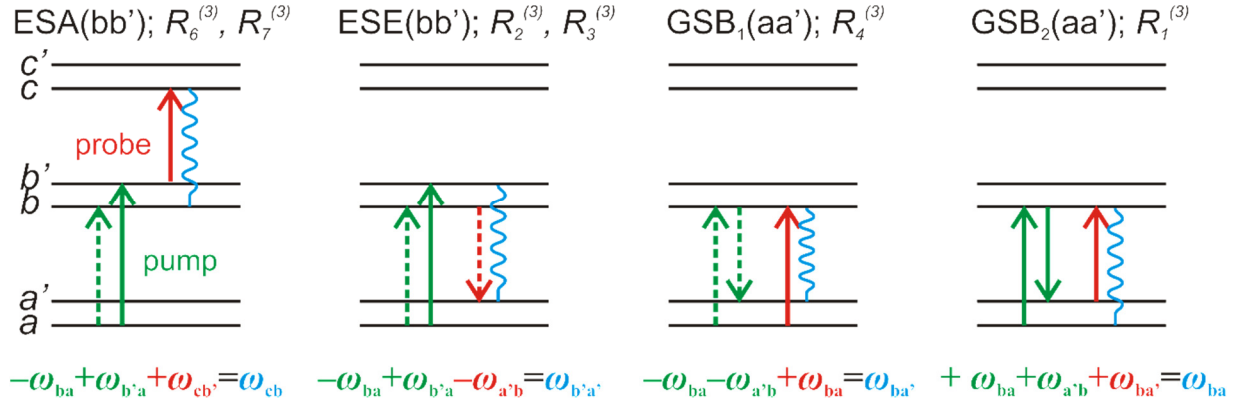


Figure 2.9: Diagrammatic representation of the selected categories from 3rd-order response functions in the pump-probe experiment.⁸⁵ The solid line and the broken lines are corresponding to the ket interaction or the bra interaction, respectively. The wavy line is corresponding to the energy of the emission. The color code is comparable with Figure 2.8a. Each signal survives with the lifetimes of the relevant dephasing processes. Each pathway contains the processes in which the electric fields prepare stationary or nonstationary states on the relevant potential surfaces. The emission signals contain vibronic frequencies of $\omega_{aa'}$ or $\omega_{bb'}$ generated by GSB pathway or ESA/ESE pathway, respectively. ESA – excited-state absorption, ESE – excited-state emission and GSB – ground-state bleaching.

As shown in Figure 2.9, ESA, ESE and GSB can be observed in pump-probe experiment. In $R_2^{(3)}$, $R_3^{(3)}$, $R_6^{(3)}$ and $R_7^{(3)}$, the first pulse ($k_{IP} = k_1 = k_2$) prepares a nonstationary vibrational state on an excited electronic potential surface. The dephasing dynamics is scanned by the probe pulse through excited-state absorption (ESA in Figure 2.9 $R_6^{(3)}$ and $R_7^{(3)}$) or stimulated emission (ESE in Figure 2.9 $R_2^{(3)}$ and $R_3^{(3)}$). In addition, the dephasing on the ground state is observed through the vibrational state on the ground state expressed as GSB pathways ($R_1^{(3)}$ and $R_4^{(3)}$). The intensity of each term has a dependence on the transition dipoles between the energy levels. Since the intensity of the probe pulse is also observed in pump-probe experiment, the time evolution of the frequency-domain transition dipoles of populated states (population relaxation) is efficiently observed as increasing or decreasing of the intensity of probe pulse. In addition, pure or ensemble dephasings appear as a fluctuation of the signal intensity on time axis. The oscillatory signals are induced by wavepacket motion on the ground state ($R_1^{(3)}$ and $R_4^{(3)}$) or the excited state ($R_2^{(3)}$, $R_3^{(3)}$, $R_6^{(3)}$ and $R_7^{(3)}$). As a result, the populations and the decoherences are observed in pump-probe experiment.

On the other hand, the pump-DFWM experiment, a kind of six-wave mixing, can effectively observe wavepacket motions as background-free signal. The 5th-order nonlinear response functions contain 16 terms and their complex conjugates as shown in Eq. (D5-4) of Appendix D. In pump-DFWM experiment, there are nine sequences of dipole interactions as shown in Eq. (B19) in Appendix B due to the degeneracy of the electric fields. Through the detail consideration shown in Appendix B.5, the interaction sequences of the observable signal are categorized into seven terms as expressed in Figure 2.10.

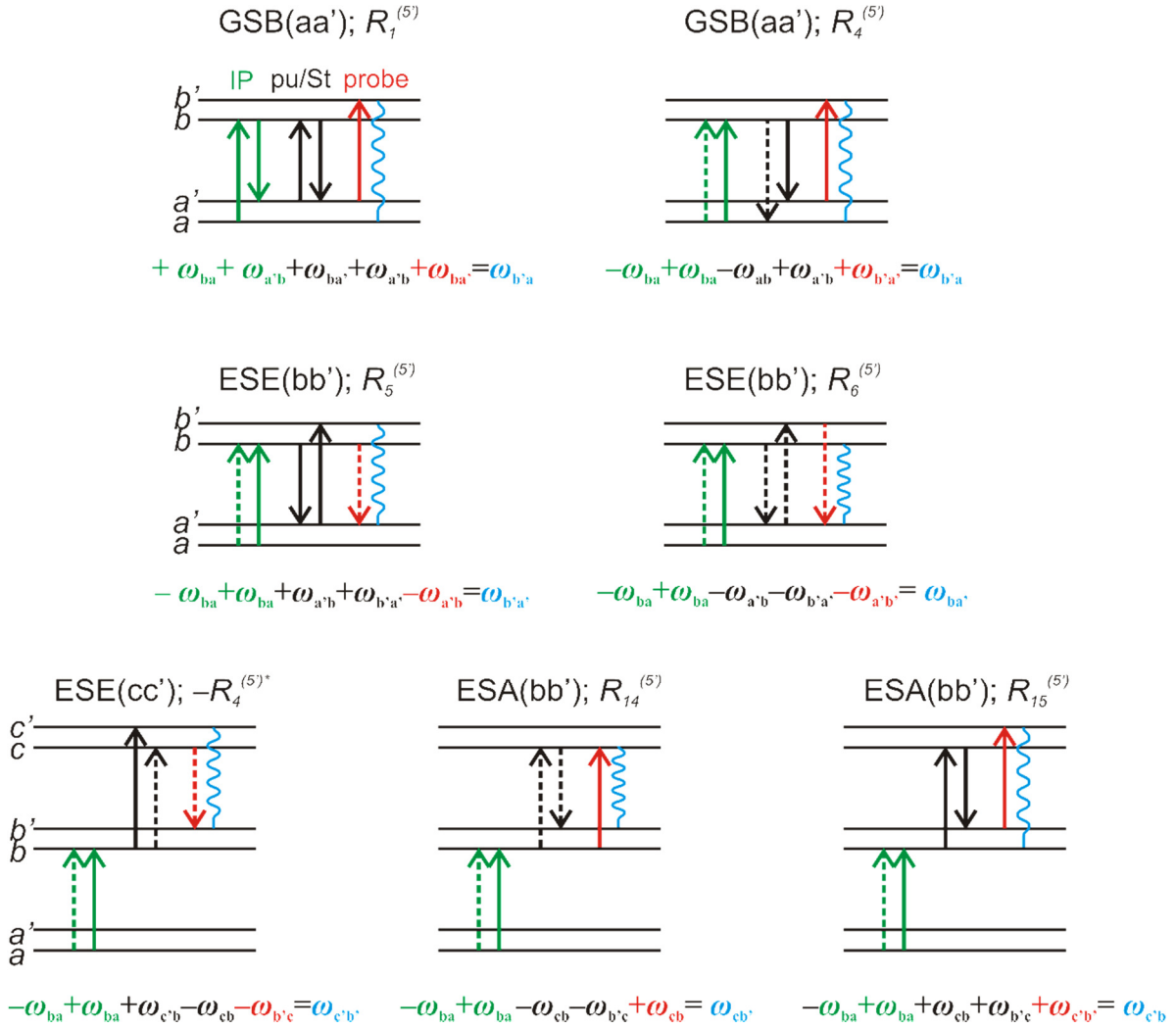


Figure 2.10: Diagrammatic representation of 5th-order response functions observed in pump-DFWM experiment. The solid line and the broken lines are corresponding to the ket interaction or the bra interaction, respectively. The wavy line is corresponding to the energy of the emission. The color code is comparable with Figure 2.8b. Each pathway contains the processes in which the electric fields prepare stationary or nonstationary states on the relevant potential surfaces. The emission signals contain vibronic frequencies of $\omega_{aa'}$, $\omega_{bb'}$ or $\omega_{cc'}$ generated by GSB pathway, ESE pathway or ESA pathway. ESA – excited-state absorption, ESE – excited-state emission and GSB – ground-state bleaching.

The optical signals generated by 5th-order nonlinear spectroscopy contain ESE, ESA and GSB with the coherence of each state as shown in Figure 2.10. Stimulated Emission Pumping (SEP) pathways, which are ESE pathways of the $R_4^{(5')}$, $R_5^{(5')}$ and $R_6^{(5')}$ in Figure 2.10, present a well-known process having a strong contribution to the total signal.⁸⁶⁻⁹⁰ In pump-DFWM experiment, compared with pump-probe experiment, it is possible to disentangle population dynamics and coherence in more detail by the τ axis. However, increasing the number of measurement axis often detracts the resolution of other axis. Since each scan on τ axis must be done for each T step in pump-DFWM experiment, the time resolution on T axis is sensitive to the experimental conditions, like noise or the drifting of laser intensity. Due to the differences on their signal generation mechanisms, the two techniques have some advantages and disadvantages. In short, pump-probe spectroscopy mainly contains 3rd-order nonlinear signals consisted of population dynamics with high temporal resolution. On the other hand, pump-DFWM contains 5th-order nonlinear contributions generated through highly characterized signal generation mechanisms. In the multimodal approach (Chapter 4), we combine two experiments to exploit the complementary features of the techniques.

2.3 Functional Analysis for Time-resolved Spectra

In general, spectral data is recorded as a multidimensional function having energy and time axes. The signal contains more than one contribution as indicated by the response functions in the previous section. Thus, many researchers employ functional analysis, usually called global target fitting or SVD analysis, to decompose and reconstruct spectral data based on some theoretical model.^{53-58,91} However, less attention has been paid for the reliability and accuracy of the analysis for time-resolved spectra. In addition, it is usually challenging to distinguish the correct model for the dynamics on the femtosecond timescale, compared with the picosecond timescale, due to the existence of many more phenomena. Since the transparency of analytical processes is strongly required due to such background, this section introduces the analytical process applied on time-resolved data sets in this work.

2.3.1 Decomposition of Spectral Data

Functional analysis is a strong tool to evaluate spectroscopic data. Since a raw data set often contains many different contributions, dynamical and spectral separations of each contributions are necessary for the unique interpretation of experimental results. If we assume a matrix \mathbf{A} ($m \times n$) which contains spectral information measured on the wavelength (λ -axis) axis for each time step (T -axis), the matrix can be expressed as a sum of the components as shown in Figure 2.11. While there are many ways to decompose the original signal, it is possible to obtain a set of the components having physical meanings by use of the simultaneous fitting with kinetic models or some simulations such as Franck-Condon Factor simulation⁹².

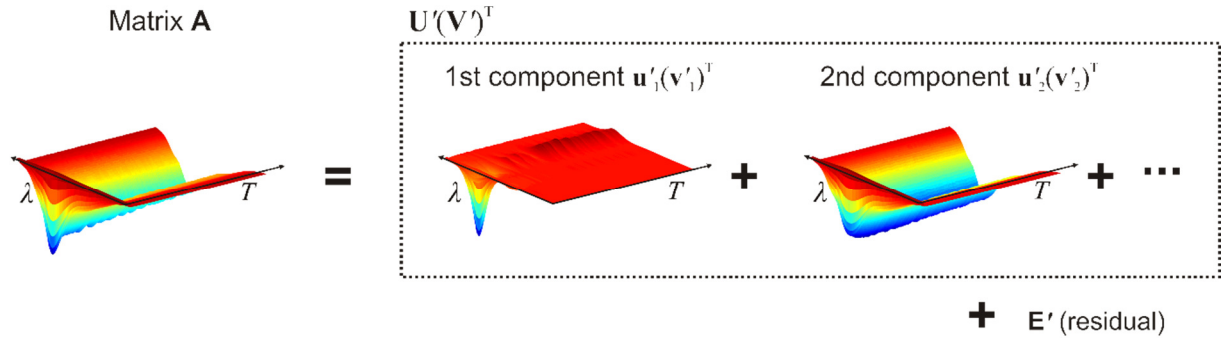


Figure 2.11: Functional analysis decomposes spectral data into several components which are the products of spectral and temporal elements.

The decomposition shown in Figure 2.11 is expressed as

$$\mathbf{A}(m, n) = \mathbf{U}'(m, k)\mathbf{V}'^T(k, n) + \mathbf{E}' = \sum_k \mathbf{u}'_k(m)\mathbf{v}'_k{}^T(n) + \mathbf{E}' \quad , \quad (5)$$

where the matrix \mathbf{A} ($m \times n$) contains spectral data with a time axis $T(m)$ and a wavelength axis $\lambda(n)$, the matrix \mathbf{U}' ($m \times k$) contains the temporal elements and the matrix \mathbf{V}'^T ($k \times n$) contains the spectral elements of k components, the matrix \mathbf{E}' ($m \times n$) contains the residual signal. The product of the k -th vectors, \mathbf{u}'_k and $\mathbf{v}'_k{}^T$, gives the k -th component shown in Figure 2.11.

2.3.2 Coefficient Matrix (C-matrix)

The analytical process shown in Figure 2.11 or in Eq. (5) consists of two steps: Singular Value Decomposition (SVD) and linear transformation. The SVD has been widely used for the systematic analyses of time-resolved spectra^{53,56,57}. The SVD operation on the matrix \mathbf{A} yields

$$\mathbf{A} = \sum_k \mathbf{u}_k s_k \mathbf{v}_k^T, \quad (6)$$

where s_k is the singular value obtained from diagonal elements, \mathbf{v}_k is the spectral element and \mathbf{u}_k is the temporal evolution of the k -th SVD component. $\{\mathbf{v}_k\}$ and $\{\mathbf{u}_k\}$ are both normalized and orthogonal sets of eigenvectors. For each eigenvectors, the following transformation is performed by use of a Coefficient matrix (C-matrix), \mathbf{C} ($k \times k$),

$$\mathbf{A} = \sum_i \mathbf{u}_i s_i \mathbf{v}_i^T = \sum_i s_i \mathbf{u}_i \mathbf{C} \mathbf{C}^{-1} \mathbf{v}_i^T = \sum_j \left[\left(\sum_i \sqrt{s_i} c_{ij} \mathbf{u}_i \right) \left(\sum_i \sqrt{s_i} c_{ji}^{-1} \mathbf{v}_i^T \right) \right] = \sum_j \mathbf{u}_j^r (\mathbf{v}_j^r)^T, \quad (7)$$

where the rotated vectors \mathbf{u}_j^r and \mathbf{v}_j^r contain the time-dependent concentration profiles and the characteristic spectra of the j -th component. In Eq. (7) the C-matrix performs a rotation of the orthogonal vectors $\{\mathbf{v}_k\}$ and $\{\mathbf{u}_k\}$. Figure 2.12 illustrates the analytical processes described in Eq. (7).

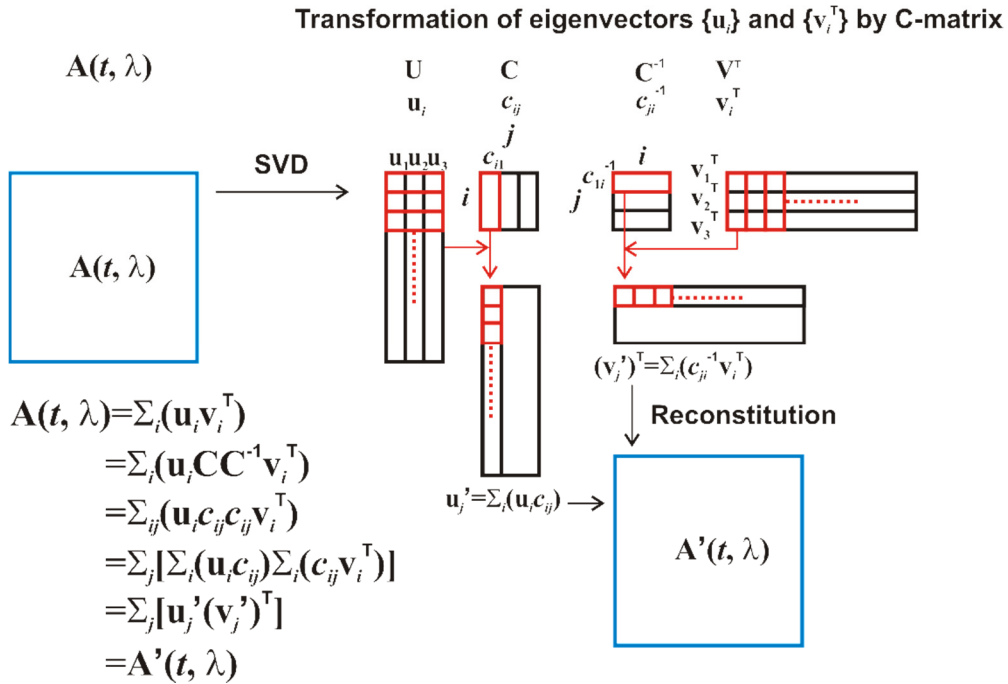


Figure 2.12: Decomposition and transformation for the spectral data matrix, \mathbf{A} .

The reconstituted data matrix, \mathbf{A}' , is calculated by the selected k' elements ($k' \leq k$). Then, the matrix \mathbf{A}' is expressed as

$$\mathbf{A}' = \sum_{j=1}^{k'} \mathbf{u}'_j (\mathbf{v}'_j)^T \quad . \quad (8)$$

The difference between the original spectra, \mathbf{A} , and the reconstituted spectra \mathbf{A}' must be the same with the sum of the components left out before the rotation operation. Thus, the reconstituted spectra shown in Eq. (8) cannot be used to evaluate the reliability of the analysis. For the proper decomposition of the spectral data, it is necessary to perform simultaneous fitting with all possible theoretical kinetic models accompanied with the rotation of the vectors.

2.3.3 Rate Equations

The kinetic model, $\{\mathbf{p}_i(T, \sigma, \tau_1, \dots, \tau_{k'})\}$, is simply given by the convolution of rate equations and instrumental response function, $\text{IRF}(T, \sigma)$. The kinetic model and Instrumental Response Function (IRF) have the axes of the delay time, T , Full Width at Half Maximum (FWHM) of IRF, σ , and lifetime τ_n . For example, the kinetic elements $\{\mathbf{p}_i\}$ of sequential model with 3 elements ($k' = 3$) are given by,



with the three profiles given by

$$\begin{aligned} p_A(T) &= [A]_0 e^{-k_1 t} * \text{IRF} \\ p_B(T) &= \left\{ \frac{k_1}{k_2 - k_1} [A]_0 (e^{-k_1 t} - e^{-k_2 t}) \right\} * \text{IRF} \\ p_C(T) &= \left\{ \frac{k_1 k_2}{(k_3 - k_2)(k_2 - k_1)(k_1 - k_3)} [A]_0 \{ (k_2 - k_3) e^{-k_1 t} + (k_3 - k_1) e^{-k_2 t} + (k_1 - k_2) e^{-k_3 t} \} \right\} * \text{IRF} \end{aligned} \quad (9)$$

where the exponential decay time constants are given by $k_n = \frac{1}{\tau_n}$. Figure 2.13 illustrates an example of the rate equations. Figure 2.13 (a) shows that the first component having $\tau_n = 40$ fs loses 63 % of the population by 40 fs. It is very important that 37% of the population is still remaining at $T = 40$ fs. There is a typical misunderstanding that all of the population disappears within the lifetime. In addition, the appearance of actual kinetic model used in the analysis is convoluted with IRF as shown in panel (c).

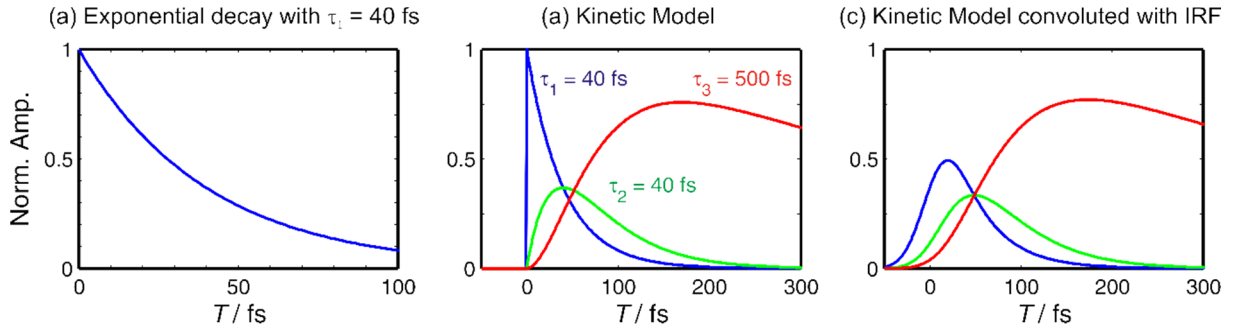


Figure 2.13: Kinetic elements $\{\mathbf{p}_i(T)\}$ for a sequential model with $k' = 3$. The lifetimes of the three species are $\tau_1 = 40$ fs (blue), $\tau_2 = 40$ fs (green) and $\tau_3 = 500$ fs (red) are shown. (a) The component with the lifetime of $\tau_1 = 40$ fs decays 63 % of the population in 40 fs. (b) Raw kinetic equations. (c) The convoluted kinetic equations shown in Eq. (9).

The temporal overlap in kinetic models leads to the difficulties to determine the adequate C-matrix due to the existence of some solutions having no physical meaning. In addition, the increasing of the overlap, in other words the increasing of the inner products in kinetic models, obviously lose the orthogonality of the resultants during the rotation operation. Since the C-matrix is often evaluated by the integrated errors among the whole signals or kinetic models, there can be several patterns of the C-matrix belonging to the same error values. Thus, there is often some ambiguity to determine the best C-matrix in the analysis. Since the ambiguity occurs on the rotation process, it is called rotation ambiguity.

The rotation ambiguity has a strong influence on the precision and accuracy of the analysis (detailed information is written in Chapter 4). Figure 2.14 shows the definitions of accuracy and precision in this kind of analyses.

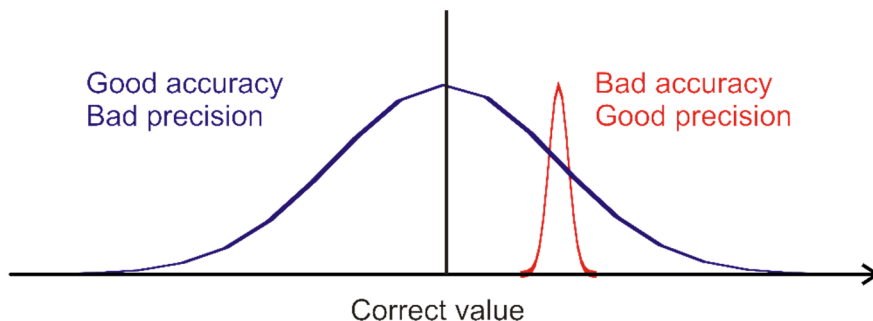


Figure 2.14: The typical relationship between the accuracy and precision of the analysis using rotation operation for simultaneous fitting with a theoretical model.

2.3.4 Error Functions

As shown in Figure 2.12, the determination of the C-matrix is the ultimate goal of the analysis. In order to optimize the C-matrix elements which can reconstitute signals based on a kinetic mode, the following error functions are introduced. In general, the error function has the axes of the elements in C-matrix and kinetic equation. The rotation of the vectors and simultaneous fitting with kinetic model are performed for all possible models to find minimum error value^{57,93}. The rotation of orthogonal vectors based on the kinetic model is often called global target fitting. This method is frequently used to analyze time-resolved transient absorption spectra. Then, the error matrices \mathbf{E}_s for time-resolved spectra, \mathbf{A}_{TA} , and \mathbf{E}_k for kinetic model are given by

$$\mathbf{E}_s(k', c_{ij}, \sigma, \tau_1, \dots, \tau_{k'}) = \mathbf{A}_{TA} - \sum_j \mathbf{p}_j (\mathbf{v}_j)^T, \quad (10)$$

$$\mathbf{E}_k(k', c_{ij}, \sigma, \tau_1, \dots, \tau_{k'}) = \sum_j (\mathbf{u}'_j - \mathbf{p}_j)^2. \quad (11)$$

The error matrices $\mathbf{E}_s(k', c_{ij}, \sigma, \tau_1, \dots, \tau_{k'})$ and $\mathbf{E}_k(k', c_{ij}, \sigma, \tau_1, \dots, \tau_{k'})$ are evaluated in an evolutionary algorithm (detail evaluation of the error functions are shown in 2.3.5 Rotation Ambiguity and Precision).

2.3.5 Relationship between Rotation Ambiguity and Precision

The relationship between rotation ambiguity and precision have a significant importance on the reliability of the analysis. In general, using many components decreases error value and increases ambiguity of rotation operation (which is often referred as “local minimum” or “rotation ambiguity”). Thus, it is strongly recommend to use a minimum number of k' which sums up to 90 % of the original signals to avoid strong overlap between the species. The singular values are useful references to choose

proper vectors for rotation operation. In addition, rotational ambiguity and precision also strongly depend on the nature of the molecules. While the population relaxation on two energy levels having a significant degeneracy often occur simultaneously, the separation of the two components often requires good separation of the components in the other axes. However, such degenerated energy levels often appear on some similar energies. Many of nonadiabatic processes or ultrafast dynamics on the femtosecond timescale often contain such molecular dynamics. Therefore, the precision and accuracy of the constants obtained in the analysis depends on the instrumental response function (IRF), rotation ambiguity and inherent degeneration of the molecular systems. In our research we take into account all of them by standard windowing and additional reference analysis⁹².

For our data analysis, the rotation and fitting are repeated till the error functions converge. To evaluate rotation ambiguity and precision of the analysis, we define the two quality functions \mathbf{q}_s and \mathbf{q}_k as

$$\mathbf{q}_s(k', c_{ij}, \sigma, \tau_1, \dots, \tau_{k'}) = \sqrt{\frac{\sum((\mathbf{A}_{TA})_{ij})^2}{\sum((\mathbf{E}_s)_{ij})^2}}, \quad (12)$$

$$\mathbf{q}_k(k', c_{ij}, \sigma, \tau_1, \dots, \tau_{k'}) = \sqrt{\frac{\sum(\mathbf{p}_j)^2}{\sum((\mathbf{E}_k)_{ij})^2}}. \quad (13)$$

Where the \mathbf{q}_s and \mathbf{q}_k describe the distribution of the error values \mathbf{E}_s and \mathbf{E}_k , respectively. The distribution of the error values are useful to evaluation the precision of the analysis. By use of Eq. (12) and (13), the precisions of each constant are determined by the Gaussian fitting as shown in Figure 2.15.

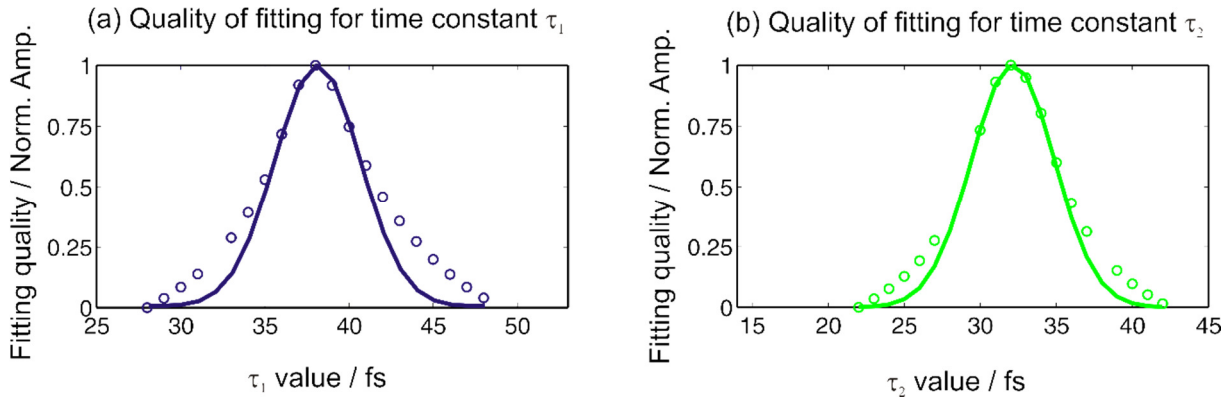


Figure 2.15: The precision of global target fitting for lutein in THF (Chapter 3.3.6). The precision of each constants are evaluated by the quality of fitting given by Eq. (13). The circles are the relative fitting qualities for an analysis of a sample data with $\tau_1 = 38 \pm 3$ fs and $\tau_2 = 32 \pm 3$ fs. A Gaussian fit (solid line) gives precision of each fitting parameter.

Regarding the functional analysis for time-resolved data in fs timescale, several ambiguities, such as local minimum or rotation ambiguity (see Chapter 4.3.3), detract the precisions of the resultants. Especially in the molecular system having quasi-degenerated states or conical intersection, the ambiguities tend to be strong due to the inherent features of the molecules. Therefore, a reliable principle

for the functional analysis for the time-resolved data in fs timescale is required to obtain unique and interpretation. In the next section 2.3.6, we suggest a new approach, Multimodal Time-resolved Spectroscopies (TRS), corresponding to the problem in ultrafast TRS.

2.3.6 Multimodal Approach

Multimodal TRS is a combination of two or more time-resolved spectroscopies to obtain the appropriate kinetic model for all experimental data sets. In the work, we demonstrate an example by use of the pump-probe and pump-DFWM experiments. The experimental data sets were decomposed simultaneously and evaluated by the error functions as shown in Figure 2.16. As a result, while all possible kinetic models are evaluated in both data sets, many wrong kinetic models are removed in the analysis. In addition, the analytical results have much evidences given by the two optical techniques. For example, the comparison of the 3rd-order and 5th order response functions indicates the signal generation pathways described by the interactions of electric fields for each components, since the analysis separates the signals generated through some of the pathways. Therefore, the multimodal approach has a totally different principle to separate the components compared with conventional SVD analyses.

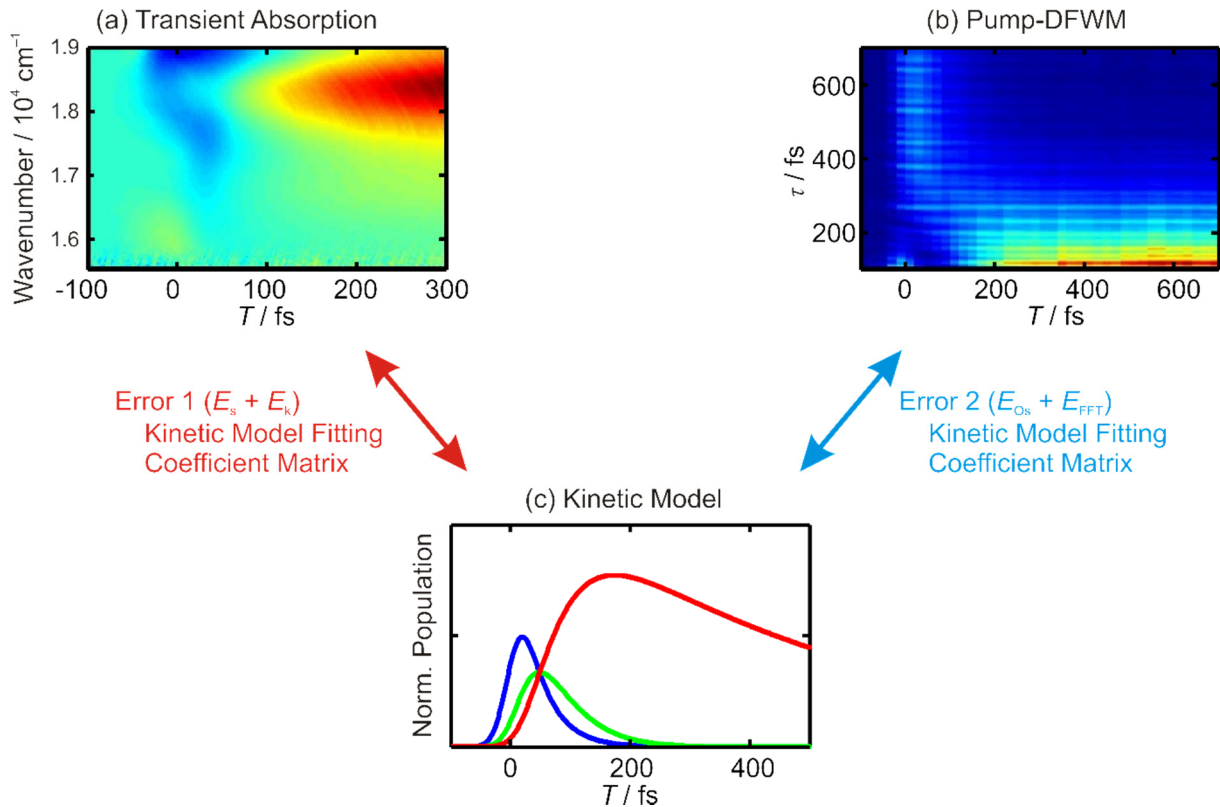


Figure 2.16: In Multimodal TRS, (c) the kinetic model is evaluated in (a) pump-probe and (b) pump-DFWM signals. The error functions are generated in both data sets. The adequate model is determined by the evaluation of the error values.

In pump-DFWM signal, the set of data is contained in a matrix \mathbf{A}_{Os} similar to the pump-probe data. However, due to the different generation mechanisms of the signals, the evaluation of kinetic models in pump-DFWM signals is performed by the components calculated by numerical simulations

instead of the singularvectors in the global target fitting. The definition of the error functions, similar to the error functions in global target fitting, are given by

$$\mathbf{E}_{\text{Os}}(k', \sigma, \tau_1, \dots, \tau_{k'}, a_{ij}, f_{ij}, \varphi_{ij}) = \mathbf{A}_{\text{Os}} - \sum_i \mathbf{p}_i^{(5)} (\mathbf{v}_i^{(5)})^T \quad . \quad (14)$$

In order to reduce the number of the calculations, Eq. (14) is evaluated in frequency domain, expressed as

$$\mathbf{E}_{\text{FFT}}(k', \sigma, \tau_1, \dots, \tau_{k'}, a_{ij}, f_{ij}) = \text{FFT}(\mathbf{A}_{\text{Os}}) - \text{FFT} \left(\sum_i \mathbf{p}_i^{(5)} (\mathbf{v}_i^{(5)})^T \right) \quad . \quad (15)$$

In Eq. (14) and Eq. (15) the following definition has been used:

$$\mathbf{v}_i^{(5)}(T, \tau, a_{ij}, f_{ij}, \varphi_{ij}) = \sum_j \theta(\tau) a_{ij} \cos(2\pi f_{ij} \tau + \varphi_{ij}) \quad , \quad (16)$$

where a_{ij} is the amplitude, f_{ij} is the frequency, φ_{ij} is the phase of the i -th mode in the j -th component and $\theta(\tau)$ is a step function. We perform numerical fitting of the pump-DFWM signals by use of the superposition of the orthogonal basis. The kinetic model, $\{\mathbf{p}_i^{(5)}(T, \tau, \sigma, \tau_1, \dots, \tau_{k'})\}$, has an additional time axis, τ , and is a squared quantity due to homodyne detection (Chapter 2.2.2). Concerning with the quality of the numerical calculation for pump-DFWM signals, the following definition has been used:

$$\mathbf{q}_{\text{Os}}(k', \sigma, \tau_1, \dots, \tau_{k'}, a_{ij}, f_{ij}, \varphi_{ij}) = \sqrt{\frac{\sum((\mathbf{A}_{\text{Os}})_{ij})^2}{\sum((\mathbf{E}_{\text{Os}})_{ij})^2}} \quad , \quad (17)$$

$$\mathbf{q}_{\text{FFT}}(k', \sigma, \tau_1, \dots, \tau_{k'}, a_{ij}, f_{ij}) = \sqrt{\frac{\sum((\mathbf{A}_{\text{Osi}})_{ij})^2}{\sum((\mathbf{E}_{\text{FFT}})_{ij})^2}} \quad . \quad (18)$$

As a result, the multimodal approach contains four error functions shown in Eq. (10), (11), (14) and (15): oscillatory signal error (\mathbf{E}_{Os}), frequency domain error (\mathbf{E}_{FFT}), 3rd-order signal error (\mathbf{E}_{s}) and kinetic model error (\mathbf{E}_{k}). For the simultaneous evaluation for each error function, we performed a loop of the calculations with stepwise changes by use of evolutionary algorithm having three steps:

- (I) Kinetic model fitting for TA and pump-DFWM (\mathbf{q}_{s} , \mathbf{q}_{Os} and \mathbf{q}_{k})
- (II) Fitting of Fourier transformed pump-DFWM transients (\mathbf{q}_{FFT} and \mathbf{q}_{k})
- (III) Phase fitting of pump-DFWM transients (\mathbf{q}_{Os} and \mathbf{q}_{k})

All three steps are repeated till the q -functions of Eq. (12), (13), (17) and (18) converge. The multimodal TRS has a smaller rotation ambiguity compared with global target analysis for pump-probe signal, due to the additional axes and many restrictions induced by pump-DFWM signal observing molecular dynamics from different aspect. Chapter 4 contains the application and results of multimodal TRS.

Chapter 3

Detecting Vibronic Coupling by Pump-probe and Pump-DFWM Experiments

3.1 Introduction

The formation of coupling on the excited-state manifold is an important factor in molecular dynamics. Many parameters in photochemical reaction, such as the relaxation pathway, lifetime, vibrational frequencies and transition dipole moments, which are strongly affected by vibronic coupling, induced by electron-nuclear motion.^{17,94} For example, the transition dipole moment of a coupled state can be enhanced by intensity borrowing from the other states.^{16,94,95} Moreover, the presence of the conical intersection in close-lying and strongly coupled electronic states may lead to some strong nonadiabatic effects.¹⁶ Many theoretical and experimental research have proved that the interactions between energy levels are essential to describe molecular dynamics.^{5,16,24}

The vibronic coupling has a unique dependence on the symmetries and degeneracy of energy levels. Theoretical description and experimental detection of the coupling dependence on the structure of excited-state manifold are a major topic in physical chemistry. In addition, vibronic coupling is very sensitive to the molecular environment. Environmental factors, such as solvent polarizability, temperature or other external interactions, are able to modify the energy levels and coupling strength. In fact, the pigments for light-energy harvesting are stored in a photosynthetic apparatus as a pigment-protein complex which gives rise to a unique absorption spectrum. For example, the retinal in rhodopsin has a unique bond selectivity, efficiency and dynamics which are strongly influenced by its surrounding.^{4,5,96} Therefore, the coupling can be a key feature to modify molecular properties in natural systems. In general, coupling is particularly important the larger the molecule becomes, due to the increased number of degree-of-freedom and close-lying electronic states.

In this work, vibronic coupling was experimentally evaluated in photosynthetic polyenes (carotenoids) as model molecules in which approximate C_{2h} symmetry gives rise to a set of low-lying singlet states with A_g or B_u symmetries. For example, the two low-lying electronic states (S_0 and S_1) having the same geometry, A_g , lead to a strong vibronic coupling through the A_g C=C stretching mode.^{22,23} The coupling between the $1A_g^-$ (S_0) and $2A_g^-$ (S_1) states in carotenoids increases the vibrational frequency of the C=C in S_1 by 100 – 150 cm^{-1} .²³ On the other hand, the early dynamics of the couplings occurring on the $S_2(1B_u^+)$ with $S_x(1B_u^-$ or $3A_g^-)$ states are still not clear. Interestingly, the degeneracy between S_2 and S_x states in the polyene is modified by the number of conjugated double bonds as shown in Figure 2.4 in Chapter 2. Thus, it is expected to observe some difference on the coupling strengths for each polyene in time-resolved optical experiments.

The interaction of electronic states induced by nuclear motion is effectively observed by pump-probe and pump-DFWM experiments with high time resolution. However, it is often difficult to distinguish the coupling dynamics out of population dynamics in pump-probe experiment. On the other hand, direct observation of wavepacket motion in pump-DFWM experiment leads to detail information about the vibronic interaction. The appearance of vibronic coupling and ultrafast molecular dynamics on the two optical experiments are compared in the work.

In this work, we demonstrate pump-probe and pump-DFWM experiments for a series of carotenoids with $N = 9, 10, 11$ and 13 having a set of energy levels with B_u^+ , B_u^- and A_g^- symmetries. The relaxation dynamics after the excitation of $S_0 \rightarrow S_2$ usually contains S_2 ($1B_u^+$), S_x ($3A_g^-$ or/and $1B_u^-$), S_1 ($2A_g^-$) and S_0 ($1A_g^-$). The dependence of vibronic effects on the conjugation length and solvent polarization are carefully examined. Depending on the number of conjugated double bonds, we will show that the shift of the C=C and C-C frequencies in the first 200 fs can be explained by the vibronic coupling between the $1B_u^-$ and $1B_u^+$ states. Moreover, by carefully changing the solvent, the strength of this coupling can be fine-tuned and, therefore, the vibrational dynamics can be modified.

3.2 Experimental Methods

3.2.1 Extraction and Purification of Carotenoids

All-*trans*-carotenoids named neurosporene ($N = 9$), spheroidene ($N = 10$), lycopene ($N = 11$), spirilloxanthin ($N = 13$) and lutein ($N = 9, \beta = 1$) were used in the research. Lycopene and lutein were extracted from tomato and spinach and purified in our laboratory. Neurosporene, spheroidene and spirilloxanthin were extracted from *Rhodobacter sphaeroides* G1C, *Rhodobacter sphaeroides* 2.4.1 and *Rhodospirillum rubrum* S1 and purified in Prof. Dr. Richard J. Cogdell group (University of Glasgow, United Kingdom), respectively. This section contains the experimental methods to prepare samples for the measurements.

The extraction and purification of lycopene ($N = 11$) and lutein ($N = 9, \beta = 1$) from tomato and spinach were carried out at room temperature under weak light condition to prevent isomerization of the pigments. In the extraction process, tomato for lycopene (spinach for lutein) were powdered after freeze drying. Pigment mixture was extracted from 100 g of the powdered sample with 200 ml of acetone. The mixture was percolated to obtain the solvent part. The extraction processes were repeated three times. After extraction, the solution part was evaporated by rotary evaporator to replace the solvent with acetone/hexane (1/1, v/v).

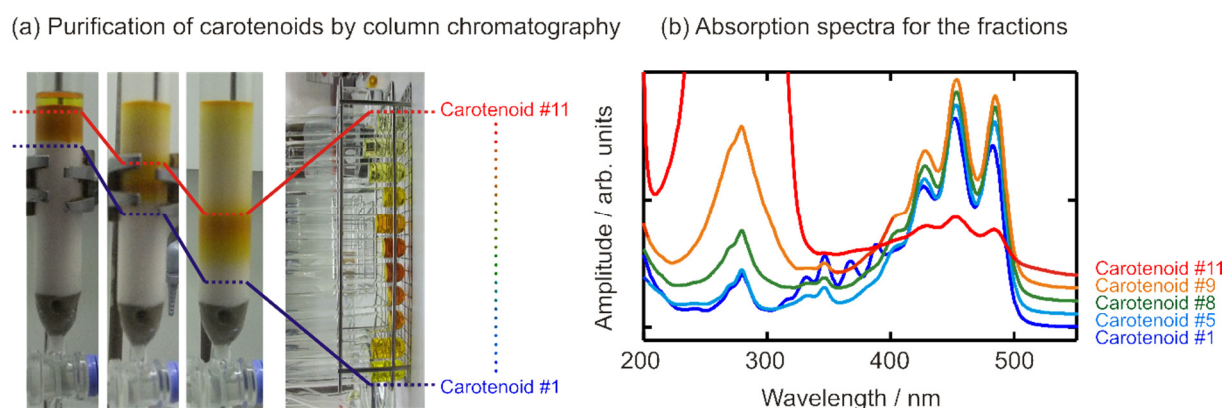


Figure 3.1: (a) Column chromatography (aluminium oxide) separates polyenes into the fractions having different (b) absorption spectra.

The purification of carotenoids was performed by two kinds of column chromatographies. The first column chromatography with Silica-gel (Merck, silica gel 60) was performed to remove chlorophylls roughly. The pigment mixture was dried up by rotary evaporator. The crude carotenoids were purified by a pair of alumina column chromatography (Merck, aluminium oxide 90 standardized) and the silica gel column chromatography. 30 – 60 % acetone in hexane was used as a stepwise gradient developer. The fractions containing pure carotenoid were selected by absorption spectra as shown in Figure 3.1. The set of column chromatographies was performed twice. Pure carotenoid was dissolved into hexane with a small amount of tetrahydrofuran (THF) and recrystallized under $-25\text{ }^{\circ}\text{C}$. The crystals were washed by hexane before dissolving in the solvent for the measurements.

Carotenoids were diluted in the solution (methanol, hexane, THF, or benzene) to be $\text{OD} = 2.0$ in 1 mm path at the 0-0 transition peak. All solutions were filtered through a syringe filter (KY61.1, Rotilabo) before measurement. During the measurement, the sample was exchanged continuously via a

flow cell with the thickness of 500 μm . The stability of the sample was checked by measuring the absorption spectrum before and after measurement.

3.2.2 Pump-probe and Pump-DFWM Experiments

The time-resolved pump-probe and pump-DFWM experiments were carried out by using the same experimental setup^{27,97,98} shown in Figure 3.2 under the comparative conditions. All pulses were generated using non-collinear optical parametric amplifiers (NOPA) which were pumped by the output of Ti:Sapphire-based amplifier with integrated oscillator and pump lasers (100 fs, 1kHz, $\lambda_{\text{cent}} = 795 \text{ nm}$, 1.8 W). The initial pump (IP) pulse (18 fs) was sent to a delay line (T -delay) and a chopper to implement time-resolved experiment, while two DFWM pulses (13 fs) were further delayed via the piezo stages. Pump and Stokes pulses were adjusted to be $\tau_{12} = 0$ to obtain the maximum intensity of nonlinear signals at phase matching position. DFWM beams were arranged in a folded BOXCARS geometry⁴² producing a spatially separate background-free signal. In pump-DFWM experiment, the signal appearing at $k_S = k_{\text{Pu}} - k_{\text{St}} + k_{\text{Pr}}$ was observed by a pair of photomultipliers at selected wavelengths by narrow-band pass filter. The pump-probe spectroscopy is carried out with the chopped IP pulse and white-light continuum as the probe pulse detected by silicon photo-diode array.

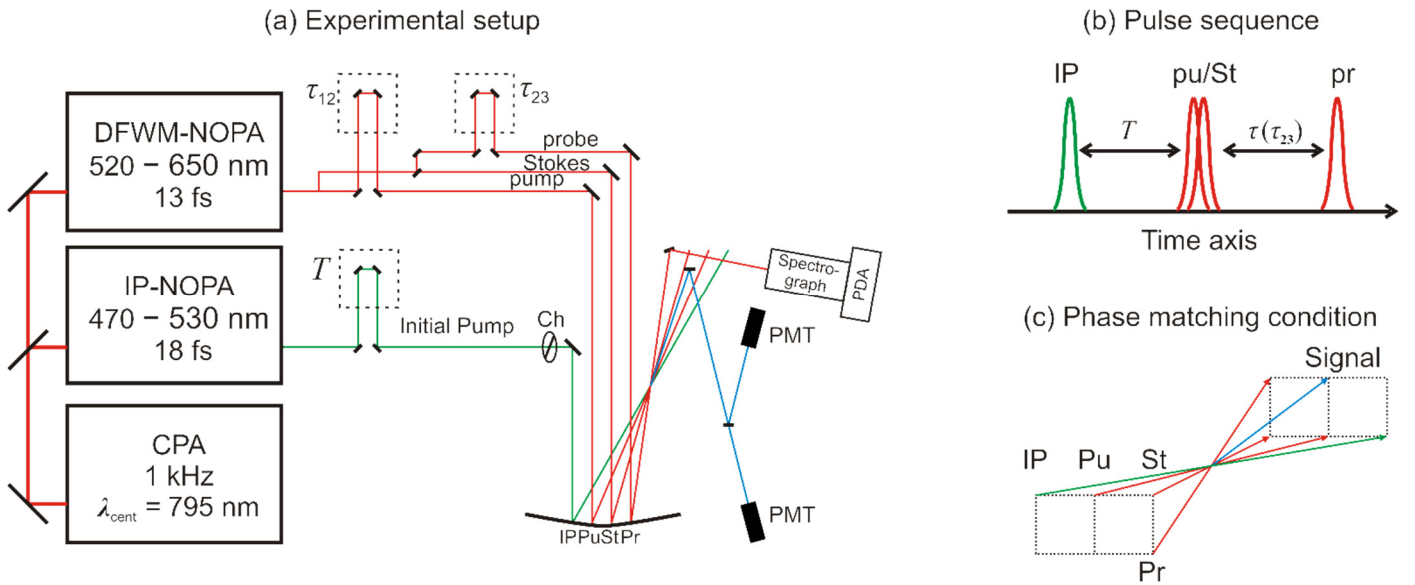


Figure 3.2: (a) Experimental setup, (b) pulse sequence and (c) phase matching condition for pump-probe (IP and Pr) and pump-DFWM experiments. The three pulses of four-wave mixing sequence, Pu, St and Pr, were aligned to construct a BOXCARS geometry⁴² at the focusing point. NOPA – Non-collinear Optical Parametric Amplifier, CPA – Chirped Pulse Amplifier, PDA – Photo-Diode Array, PMT – Photo-Multiplier Tube, IP – Initial Pump pulse, Pu – Pump pulse, St – Stokes pulse, Pr – Probe pulse, Ch – Chopper.

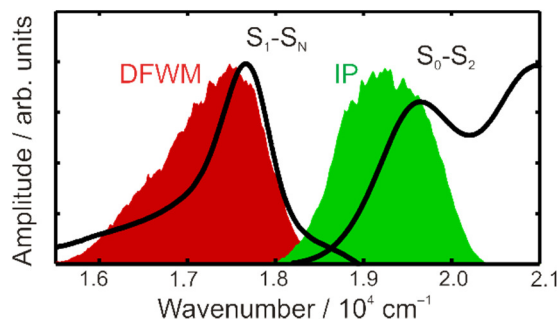


Figure 3.3: Interaction scheme of pump-probe and pump-DFWM experiments. The IP (green) and DFWM (red) excitation spectra of the time-resolved spectroscopies for lycopene as an example of the carotenoids are shown. The IP pulse is resonant with the excitation from the ground state to the lowest optically-active state. The DFWM pulses are resonant with the stimulated emission from the excited states. The resonant interaction of DFWM pulses with the excited state absorption (S_1-S_N) of the carotenoids leads to the enhancement of the coherence on the electronic states.

Figure 3.3 shows the excitation spectra and absorption spectra of lycopene in THF as an example of the carotenoids. The spectrum of DFWM pulses defines which optical transitions are probed after the initial excitation by the initial pump pulse.⁴⁷ In addition, the pump-DFWM signals were observed at selected wavelengths by use of 10 nm bandpass filter in front of PMT. The experimental condition allows one to observe the relaxation dynamics from the lowest optically-active excited states ($1B_u^+$) in pump-probe and pump-DFWM experiments.

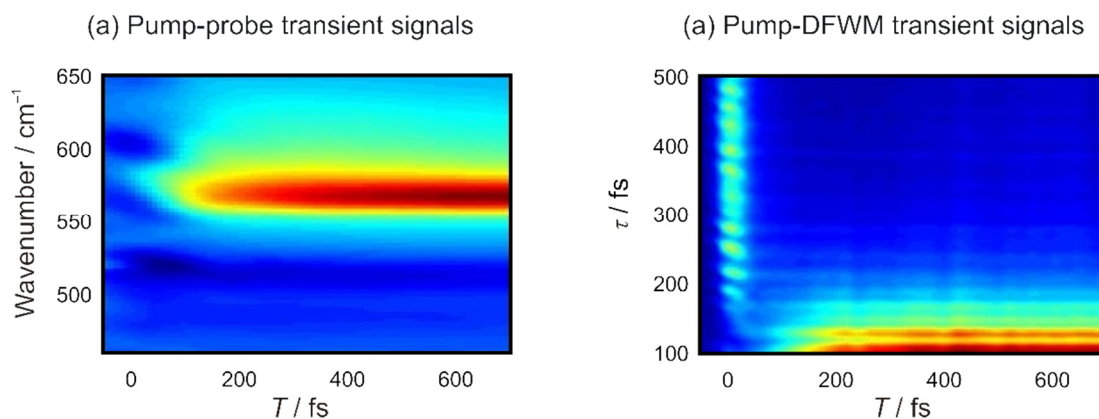


Figure 3.4: (a) pump-probe and (b) pump-DFWM transients collected for lycopene in THF. The detection wavelength of pump-DFWM transients is 630 nm.

Typical pump-probe and pump-DFWM transient signals are shown in Figure 3.4. In the early T delay, emission signals of $S_2(1B_u^+) \rightarrow S_0(1A_g^-)$ appears in pump-probe spectra. The transition between S_2 to S_0 states is observed in pump-DFWM experiment as six-wave mixing signals appearing in the early T delay. The oscillatory contributions along the τ delay are induced by the wavepacket motions on S_2 and S_0 states. At later T delay, there is strong absorption signals of $S_1(2A_g^-) \rightarrow S_N$ transition in pump-probe spectra. The pump-DFWM signals for the transition only appears in the early τ delay due to the lifetime of the relevant states.

3.3 Results and Discussion

3.3.1 Pump-DFWM Transients at Four Detection Wavelengths

The pump-DFWM signals are generated by six-wave mixing mechanisms described in Chapter 2.2 and Appendix B. In the consideration and characterization of observing response functions, the order of the pulses and detection wavelength are important information. In pump-DFWM experiment for carotenoids, the following contributions can be seen as shown in Figure 3.5.

- I) Short-lived S_2 and S_x contributions.
- II) Stimulated emission pumping between S_2 and S_0 states.
- III) Contribution from the S_1-S_N and S_1-S_0 transitions.

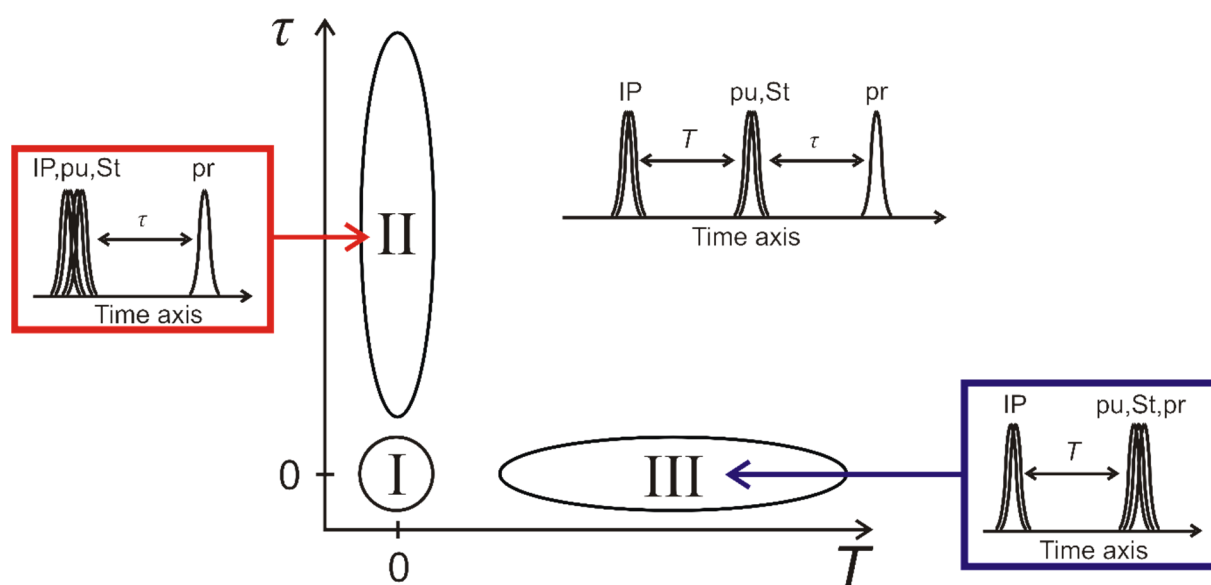


Figure 3.5: Scheme of the main contributions observed in pump-DFWM experiment for carotenoids. I – Short-lived pump-DFWM signal generated close to the Franck-Condon region. II – Stimulated emission pumping between the optically active excited state and ground state. III – Contributions from the S_1-S_N transitions.

The pump-DFWM transients of the carotenoids consist of three contributions as shown in Figure 3.5; (I) the signal appearing at $T = \tau = 0$, (II) the signal appearing at $T = 0$ in later τ delay and (III) the signal appearing at $T = 0$ in later T delay. The two contributions (I and II) appear immediately generated after the excitation of $S_0 (1A_g^-) \rightarrow S_2 (1B_u^+)$ by the initial pump pulse. Since all of the pulses are temporally overlapped at $T = \tau = 0$, there is a strong emission signal at all detection wavelengths. In the region (I), ground-state bleaching and excited-state emission between S_0 and S_2 states give rise to the strong signal. In addition, there can be a short-lived contribution which stems from a contribution of an electronic dark state (S_x) directly after the S_2 state relaxation.⁹⁸ On the other hand, in the region (II), the rising of an emission signal is observed around $\tau > 100$ fs. The emission signal is amplified by nuclear rearrangement from the Franck-Condon region on the S_2 state. In other word, the rising of hot-ground state created by excited-state configuration appears in region (II). The mechanism of the stimulated emission enhanced by pu/St sequence in $R_1^{(5')}$ and $R_5^{(5')}$ is known as stimulated emission pumping (SEP) which has been observed in retinoids as well as other molecular systems with strong fluorescence

emission transitions.^{90,99-101} In general, the SEP mechanism gives rise to the strong signal with dephasing on the excited state or ground state. In the region (III), the population dynamics of S_1 electronic states is observed. The signal is also influenced by vibrational coherence on the excited-states.

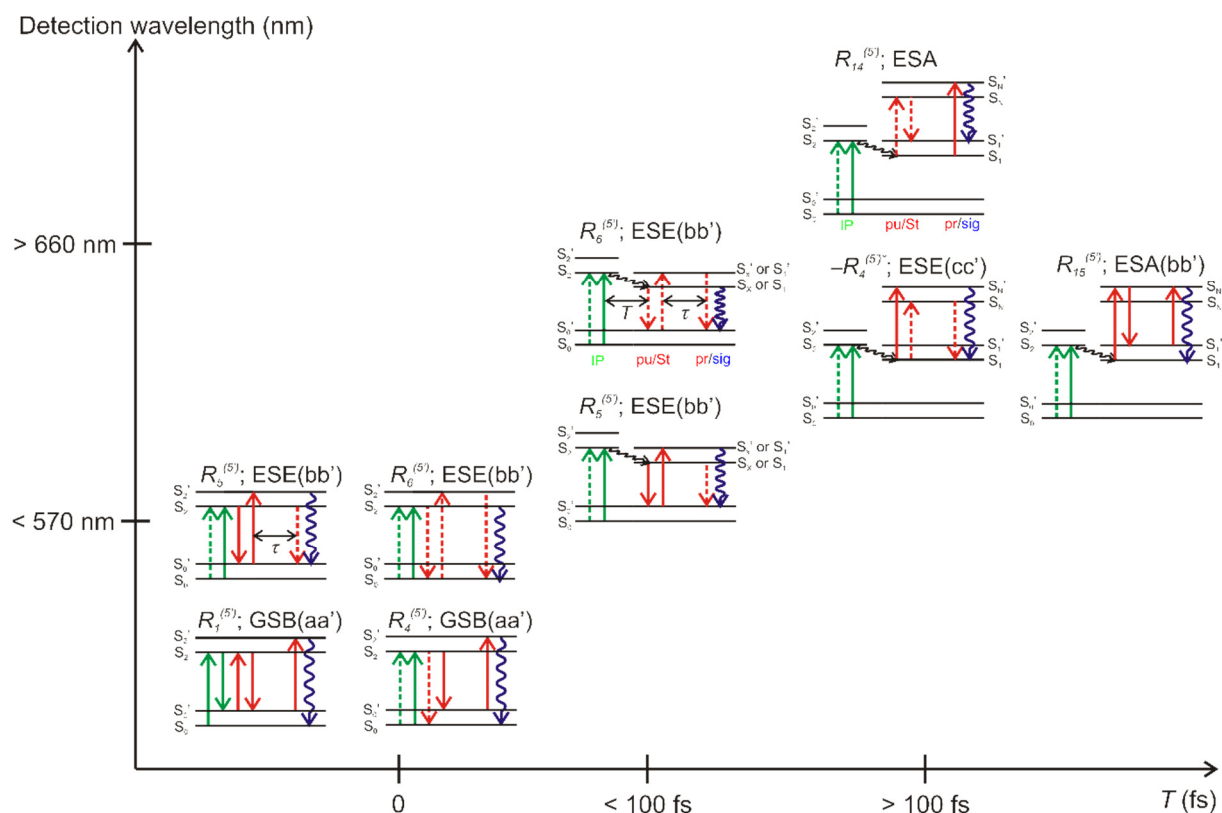


Figure 3.6: The observable sequences selected from the response functions in the pump-DFWM experiment (Figure 2.10 in Chapter 2.2.3). The energies are taken from lycopene. The dipole interactions induced by external electric fields to the density matrix are described by solid and broken lines for bra and ket interactions, respectively. Wavy lines indicate emission signals observed at $k_s = k_{IP} - k_{IP} + k_{pu} - k_{St} + k_{pr}$. The sequences are categorized into three pathways determined by IP and pr pulses. In each diagram, the two interactions induced by pump/Stokes in DFWM sequence prepare coherence on some electric potential energy surface. ESA, ESE or GSB pathways. IP – Initial Pump pulse, pu – pump pulse, St – Stokes pulse, pr – probe pulse, sig – signal, ESA – excited-state absorption, ESE – excited-state emission and GSB – ground-state bleaching.

The appearance of the signals have some differences due to the detection wavelengths. Figure 3.6 shows observable sequences and relevant electronic energy levels (S_2 , S_x , S_N , S_1 and S_0) for lycopene ($N = 11$) as an example. The energy of the emission signal depends on the energy difference between the energy levels. In addition, the energy difference between the blue wing ($570 \text{ nm} = 17540 \text{ cm}^{-1}$) and the red wing ($660 \text{ nm} = 15150 \text{ cm}^{-1}$) of the DFWM probe spectrum for lycopene nearly matches the energy of two vibrational levels of $2300 - 2600 \text{ cm}^{-1}$.⁹² Thus, some of the sequences in Figure 3.6 becomes very weak in the red wing. For example, the ESE pathways between S_x and S_0 states only appear in the red wing due to the energy. In addition, GSB ($R_1^{(5')}$ and $R_4^{(5')}$) and ESE ($R_5^{(5')}$ and $R_6^{(5')}$) pathways between S_2 and S_0 states have strong amplitude in the blue wing. In the red wing, the signals

of the two pathways are generated through hot- S_0 state instead of S_0 state. At later delay times, the signals of ESE or ESA pathways between S_N - S_1 states appear in both detection wavelengths. However, the amplitude in blue wing is much weaker than the amplitude in red wing due to the energy difference of the two states. Therefore, the signal appearing at red detection wavelength is appropriate to investigate decoherence and relaxation of excited states in carotenoids. In the experiments, the spectral width needs to be broad enough to be able to observe higher frequency mode till 1800 cm^{-1} .

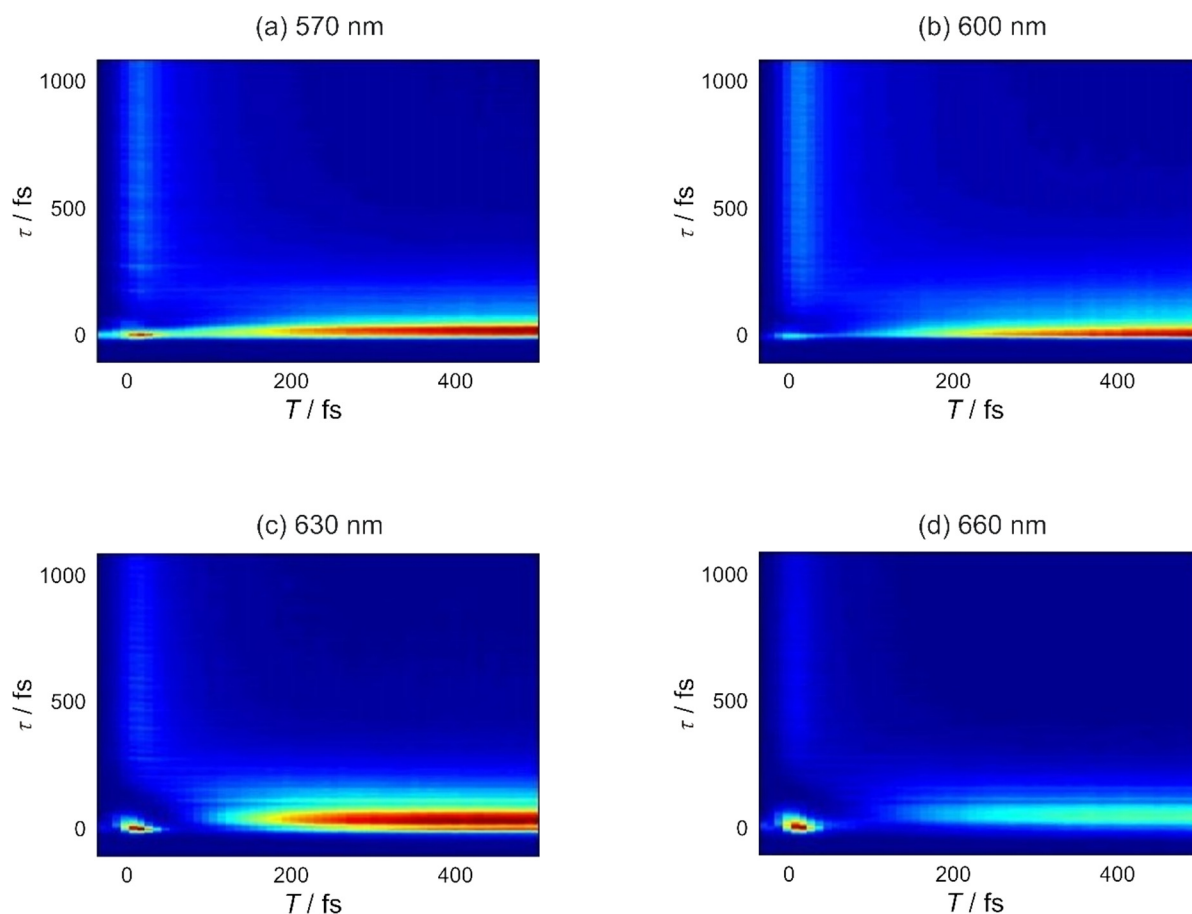


Figure 3.7: Pump-DFWM transients collected for lycopene. (a)-(d) Data was detected at $\lambda_{\text{det}} = 550, 560, 620$ and 630 nm, respectively. The normalized intensity of the signal increases from cold color (blue) to hot color (red).

Figure 3.7 shows pump-DFWM transients for lycopene detected at 570, 600, 630 and 660 nm. The pump-DFWM transients contain oscillatory and non-oscillatory contributions generated by some of the response functions shown in Figure 3.6. As explained in the previous sections, the relative amplitudes of each contributions (I, II and III) are different at each detection wavelengths. In the blue detection wavelength (570 and 600 nm), there is relatively strong contributions of II and some contributions between I and III generated through S_2 (or S_x) - S_0 states as shown in the higher energy side of Figure 3.6. On the other hand, in the red detection wavelengths (630 and 660 nm), the major contributions, generated by $S_1 - S_0$ or $S_1 - S_N$ transitions, appear in the later T delay (in the case of the detection at 660 nm, the strongest contribution appears in $T > 500$ fs).

3.3.2 Ultrafast Molecular Dynamics in the Carotenoids ($N = 9, 10, 11$ and 13)

Very early dynamics of the carotenoids with $N = 9, 10, 11$ and 13 is examined by pump-DFWM experiment. The spectrum of DFWM sequence is carefully selected to spectrally overlap with S_1 - S_N transition and not to overlap with S_0 - S_2 transition. Thus, the interaction of DFWM sequence, which is determined by the probe spectrum, is well-separated from any interaction with the $S_2 - S_0$ transitions. In fact, there was no signal except coherent artifact without the interaction of IP pulse. No signal appears before $T = 0$. In general, pump-DFWM transient contains oscillatory and non-oscillatory contributions in which time evolutions of dephasing and population relaxation are stored. Figure 3.8 shows pump-DFWM signals detected at the red wing of the four carotenoids. There are oscillatory contributions along τ delay in addition to the non-oscillatory signal in all carotenoids. The Fourier transformation of the oscillatory contribution gives rise to the vibrational spectra at each T delay as shown in the bottom panels in the Figure. The four contributions appearing in the vibrational spectra are assigned as $1150 - 1200 \text{ cm}^{-1}$ (C-C stretching mode), $1500 - 1600 \text{ cm}^{-1}$ (C=C stretching mode), 915 cm^{-1} (THF solvent mode)¹⁰² and 1800 cm^{-1} (C=C stretching mode specific to the $2A_g^-$ state)²³.

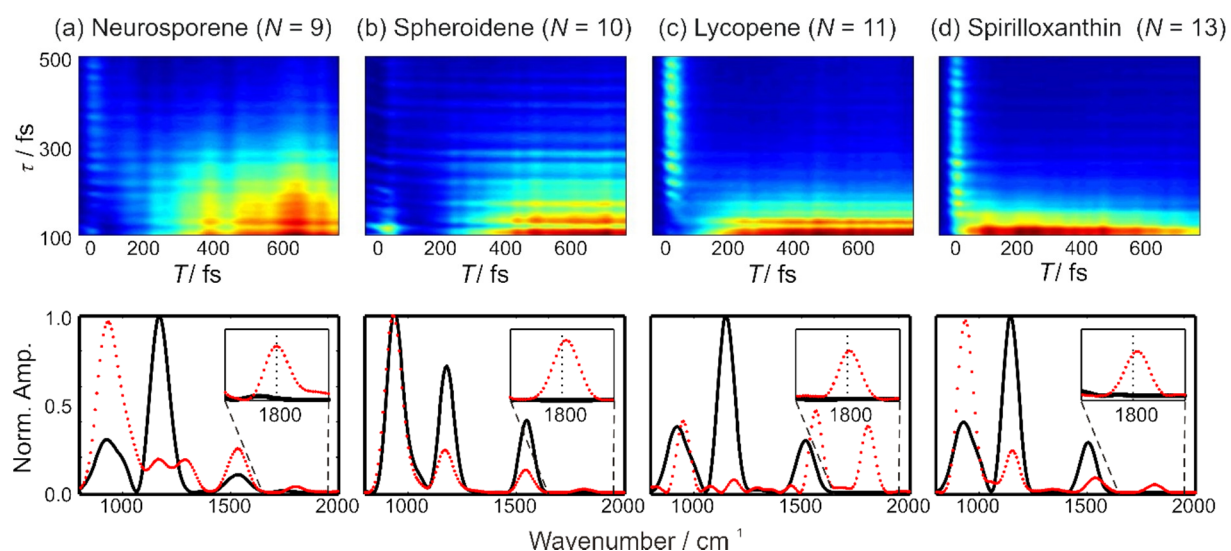


Figure 3.8: (a)-(d) Pump-DFWM signal collected for carotenoids with $N = 9, 10, 11$ and 13 , respectively. Data was detected at red wing $\lambda_{\text{det}} = 570, 600, 630$ and 660 nm for $N = 9, 10, 11$ and 13 , respectively. The intensity of the signal increases from cold color (blue) to hot color (red). (e)-(h) The Fourier spectra calculated from transients measured at $T = 25 \text{ fs}$ (black solid line) and $T = 700 \text{ fs}$ (red broken line) which is multiplied by about a factor 70 for comparison.

At the early T delay, dephasing and relaxation of the S_2 state and the dark S_x state are observed with contributions from vibrational coherence of C-C and C=C stretching modes. Especially from $T = 0$ to 100 fs , dynamical nuclear motion after the excitation can be examined by the two vibronic modes (detail information is available in 3.3.3). Obviously, the nuclear coordinate of the excited state changes from the S_2 state to the S_1 state ($S_2 \rightarrow S_x \rightarrow S_1$ or $S_2 \rightarrow S_1$) in this time region. Spheroidene ($N = 10$), and in some extent also neurosporene ($N = 9$), show non-oscillatory contributions from the optically-dark S_x state at very early T -delay, which is, however, extremely short lived along the τ delay.⁹⁸ The

long-lived signal of later τ delay is due to a contribution from the hot- S_0 state which is observed for all carotenoids slightly after $T = 0$. This fact indicates that the hot- S_0 configuration is effectively formed by the S_2 -state configuration. Since the S_2 state has ionic character leading to the delocalization of π electron of conjugated double bonds, the relative amplitude of C–C stretching mode is very strong around $T = 25$ in comparison with the vibrational spectrum at $T = 700$ fs.

In later T delay ($T > 200$ fs), the rising of the S_1 state is observed as the appearing of strong non-oscillatory contribution. In longer chain carotenoids, the rising of the non-oscillatory S_1 -state signal occurs in the earlier T delay due to the fast and effective relaxation of S_2 state. In vibrational spectra, two kinds of C=C stretching modes around 1500 cm^{-1} and 1800 cm^{-1} are observed. The detail mechanism of the phenomenon is well-known as vibronic coupling.²³ The vibronic coupling between the two states with A_g symmetry leads to the result that the frequency of the C=C stretch mode in the upper state is increased, while that in the lower state is decreased. In the carotenoids, S_1 state ($2A_g^-$) and S_0 state ($1A_g^-$) are coupled. Therefore, the frequency for C=C stretching mode of $2A_g^-$ is higher than the that of $1A_g^-$, although in general the electron density in the double bonds is expected to decrease upon excitation, causing a decrease in bond order, and hence in vibrational frequency.^{22,24}

3.3.3 Time Evolution of Vibrational Frequencies

Ultrafast deactivation processes of S_2 state take place within a few hundred fs. Hence, the dynamics are accompanied by nuclear motion which induces nonadiabatic effects on the excited energy levels. In the following experiment, the electron-nuclear motion on the excited states is examined by C–C and C=C stretching modes appearing around 1100 cm^{-1} , 1500 cm^{-1} and 1800 cm^{-1} .

Figure 3.9 shows the time evolution of C–C and C=C stretching modes observed by pump-DFWM experiment. The change of vibronic frequencies of the initial 100 fs indicates a down-shift for the carotenoids with a smaller number of conjugated double bonds ($N = 9$ and 10) while it shows an up-shift for the carotenoids with $N = 11$ and 13 . For example, neurosporene ($N = 9$) shows a down-shift of the C=C stretching mode from about 1580 to 1510 cm^{-1} . Contrasting to that, spirilloxanthin ($N = 13$) shows an up-shift from about 1510 to 1530 cm^{-1} .

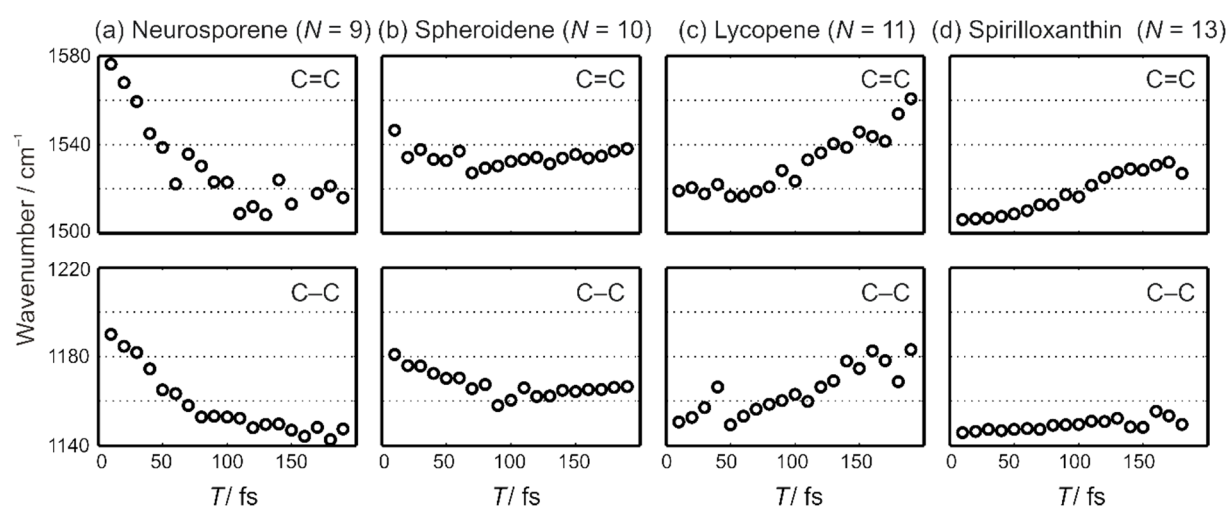


Figure 3.9: Initial dynamics of the frequency of the (a)-(d) C=C and (e)-(h) C–C stretching modes for carotenoids with $N = 9$ (1st column), 10 (2nd column), 11 (3rd column) and 13 (4th column). Spectra was obtained Fourier transformation of transients between $\tau = 100$ and 550 fs.

The C=C stretching mode of the S_1 ($2A_g^-$) state appearing at 1800 cm^{-1} arises after the relaxation of the S_2 state. Figure 3.10 shows the time evolution of frequency and amplitude of the mode. In general, the longer the carotenoid, the faster is its rise dynamics: The amplitude of this mode in spirilloxanthin ($N = 13$) increases with a time constant faster than 200 fs, while the rise time is much slower (> 500 fs) for spheroidene ($N = 10$). The central frequency of this mode also changes in time, but all carotenoids showed a comparable upshift of the frequency during the evolution over the initial 800 fs. The dynamics of this mode in neurosporene ($N = 9$) was not possible to resolve due to its low amplitude, and, therefore, a fitting was not conclusive.

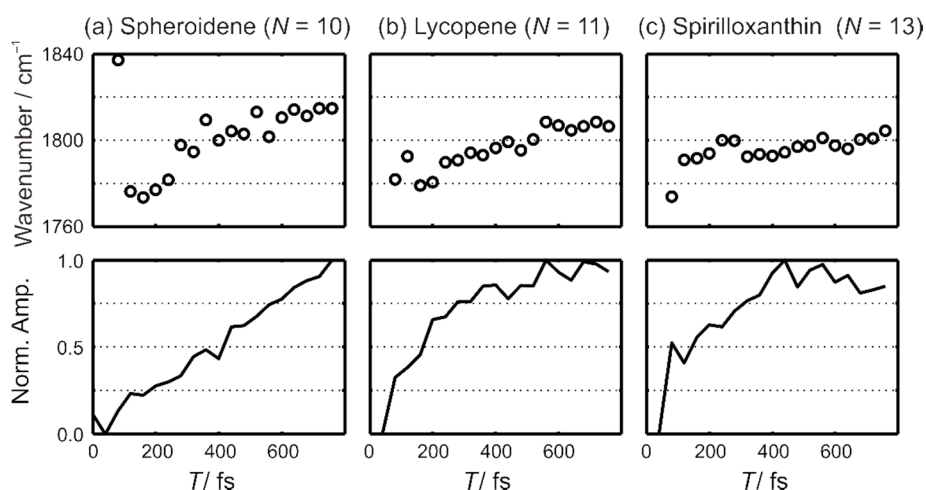


Figure 3.10: Initial dynamics of (a)-(c) frequency and of the (a)-(c) amplitude of the C=C specific to S_1 state for carotenoids with $N = 10$ (1st column), 11 (2nd column) and 13 (3rd column). Spectra were obtained by Fourier transformation of transients between $\tau = 100$ and 550 fs.

Table 3.1 shows vibrational frequencies of C–C and C=C stretching modes observed from the S_1 state ($T = 700$ fs), S_2 state ($T = 25$ fs) and ground-state (from literature by other techniques). In addition, the vibronic frequencies of the S_2 state are separated into two categories: One has strong contribution from the S_2 state ($T = 25$ fs, $\tau = 100$ –450 fs) and the other has a strong contribution from hot- S_0 state ($T = 25$ fs, $\tau = 200$ –550 fs). Interestingly, both stretching modes have higher frequencies on the S_1 state ($T = 700$ fs) or the S_2 state ($T = 25$ fs, $\tau = 100$ –450 fs) compared to the frequencies observed in literature of Table 3.1. Moreover, the gap of the frequencies observed on S_2 state and S_0 state becomes bigger as the polyene becomes shorter. In general, the excited-state should have lower frequencies due to decreasing electron density in the double bonds, but the results contradict the feature due to vibronic effects referred in Chapter 3.3.5.

Table 3.1: Vibrational wavenumbers of C–C and C=C modes for several open- and closed-chain carotenoids with $N = 9, 10, 11$ and 13. All units in cm^{-1} .

Open Chain	This work									Literature		
	$T=700\text{fs}$			$T=25\text{fs} - \tau=100-450$			$T=25\text{fs} - \tau=200-550$			C-C	C=C	C=C S_1
	C-C	C=C	C=C S_1	C-C	C=C	C=C S_1	C-C	C=C	C=C S_1			
Neurosporene ($N=9$)	1163	1537	1803	1181	1551	-	1156	1539	-	1151 (S_0) ^A	1515 (S_0) ^A	1780 ^A
Spheroidene ($N=10$)	1173	1545	1813	1178	1542	-	1166	1534	-	1150 (S_0) ^B	1516 (S_0) ^B	1794 ^B
Lycopene ($N=11$)	1180	1564	1803	1158	1516	-	1150	1519	-	1143 (S_0) ^B 1140 (S_1) ^E	1501 (S_0) ^B 1513 (hot- S_0) ^E 1530 (S_1) ^E	1783 ^B
Spirilloxanthin ($N=13$)	1150	1534	1802	1147	1506	-	1147	1508	-	1148 (S_0) ^C	1505 (S_0) ^C	1770 ^C
Closed Chain												
Lutein ($N = 9, \beta = 1$)	1135	1535	1783	1153	1524	-	1153	1522	-			
β -Carotene ($N = 9, \beta = 2$)	1140 ^F	1528 ^F	1765 ^F	1160 ^F	1535 ^F	-	-	-	-	1160 (S_0) ^D 1145(hot- S_0) ^D 1190 (S_1) ^D	1526 (S_0) ^D 1515 (hot- S_0) ^D 1540 (S_1) ^D	1785 (S_1) ^D

^A Resonant Raman in benzol¹⁰³, ^B Resonant Raman in benzol¹⁰⁴, ^C Resonant Raman in n-hexane¹⁰⁵,
^D Pump-DFWM and -IVS in THF¹⁰⁶, ^E Pump-DFWM in THF⁹⁷, ^F Pump-DFWM in THF²⁷.

3.3.4 Effect of Overlapping Contributions on the Evolution of Frequencies

It is important to discuss the role of temporally overlapping contributions on the experimentally detected frequencies, since population relaxation and dephasing are simultaneously observed in pump-DFWM experiment. The evolution of the frequencies after the S_0 - S_2 excitation with initial pump mainly consists of three contributions shown in Figure 3.5. Around $T = 0$, transitions between the excited electronic states near the Frank-Condon region and hot- S_0 play a major role as expected by response functions in Figure 3.6. Thus, decoherence on S_2 state was simultaneously observed with the contribution of hot- S_0 state. During very early T delay, processes involving the S_2 -hot- S_0 transition are suppressed, and transitions resonant with excited-state absorption of dark states, such as the $3A_g^-$ and $1B_u^-$, contribute to the signal. At much later T delay, the transition involving S_1 state will be the major signal source as the S_1 state is eventually populated (Figure 3.6). The dynamics of these contributions is usually overlapping along the T delay time because they are continuous processes. Therefore, it is very challenging to disentangle such contributions in one-dimensional techniques like pump-probe experiment, because all of the overlapping dephasings are integrated at each T delay. On the other hand, multidimensional time-resolved spectroscopies like pump-DFWM or pump-IVS, provide multiple time axes recording raw information of the potentially overlapping dephasings. In other words, the overlapping molecular dynamics at each T delay can be disentangled in a pump-DFWM experiment. This can be done, for example, by applying a sliding window Fourier transformation at specific time windows (Figure 3.11).

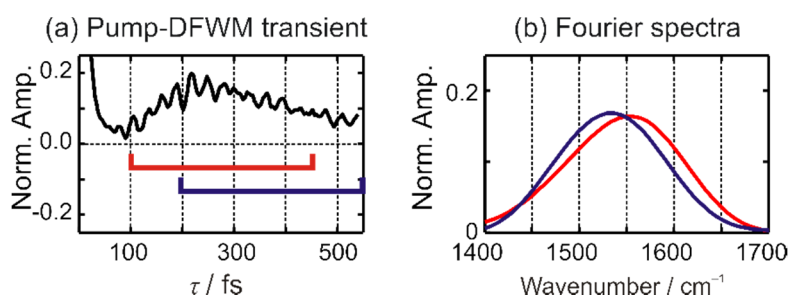


Figure 3.11: Disentangling overlapping contributions in multidimensional time-resolved vibrational spectroscopy by using sliding window Fourier transformation at specific T delay.

In Figure 3.11, overlapping molecular vibrational modes at $T < 30$ fs from hot- S_0 and electronic excited states are separated on the additional probe-axis τ of the DFWM sequence: While the coherent signal of long-lived hot- S_0 state survives at the timescale of ground-state processes (over a few picoseconds), vibrational coherence which originate from short-lived excited-states must dephase as fast as the population relaxation. Thus, around $T = 25$ fs, Fourier transformations of early τ delays lead to vibrational coherences from hot- S_0 state as well as from short-lived electronic states, while Fourier transformations of later τ delays give rise to exclusively hot- S_0 vibrational modes since short-lived excited-state contributions have already dephased. Note that the values obtained at early τ delays will be interpreted as an average of the vibrational frequencies of the S_2 state and of the hot- S_0 .

3.3.5 Vibronic Effects on Degenerate Energy Levels

The experimental observation shown in section 3.3.3 can be summarized as (i) the frequency changes of the C-C and C=C stretching modes depend on the carotenoid conjugation length and (ii) the C=C S_1 (1800 cm^{-1}) stretching mode does not follow that dependence. In general, the vibrational frequency shows an up-shift of the frequency as the system relaxes within an anharmonic potential. However, we also observed a down-shift of the frequencies for shorter-chain carotenoids (neurosporene and spheroidene). The unusual observation can be explained by vibronic coupling having a unique dependence on the symmetries of the nuclear coordinate of the relevant energy levels. Since the effect is theoretically explained by the terms ignored in adiabatic approximation, the definition of the approximation is important to understand the physical meaning of the coupling.

Born-Huang (BH) approximation, Born-Oppenheimer (BO) approximation and Condon approximation are widely accepted approximations to calculate potential energy surfaces. Although there are some differences on the terminology and definition of the approximations in literature, many physical phenomena observed in optical experiments can be explained as shown in Figure 3.12. For example, intensity borrowing can be described by the terms between BO and Condon approximations. In other words, intensity borrowing originates from the nuclear coordinate of the excited-state as indicated by the difference of the approximations. On the other hand, the adiabatic (diagonal) correction term is equivalent to the energy between BH and BO approximations as shown in Appendix F. This is experimentally examined for some simple molecules (so-called “Born-Oppenheimer diagonal correction”).¹⁰⁷ The important term in nonadiabatic processes observed in our experiments is described by derivative coupling. The derivative coupling is the term containing the most part of the effects induced by nuclear motion. It has a significant importance for the ultrafast molecular dynamics on degenerate energy levels such as conical intersection.

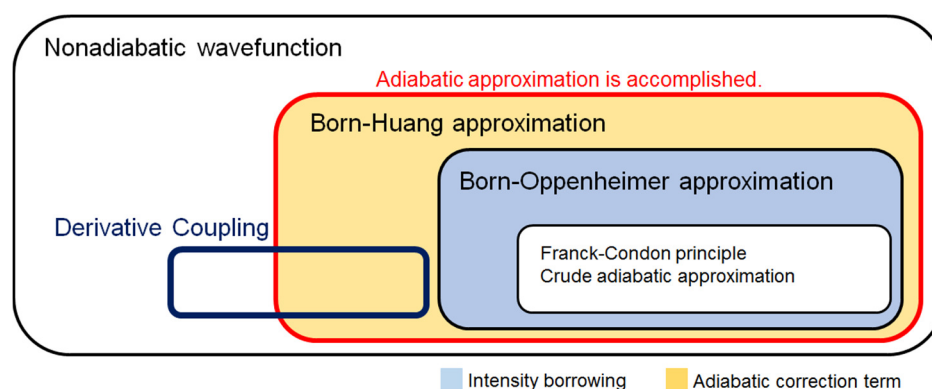


Figure 3.12: The relationship between the approximations and physical phenomena. Each part of Hamiltonian can be extracted by the wavefunctions calculated under each approximation. The definitions and mathematical formulations of the approximations are shown in Appendix F.

Derivative coupling T'_{ij} (detailed information is written in Appendix G) is expressed as a very simple formula consisting of electronic wavefunctions with fixed nuclear coordinates $\psi_i(r; Q)$, where r and Q are the electronic and nuclear coordinates,

$$T'_{ij} = \langle \psi_j | \frac{\partial}{\partial Q} | \psi_i \rangle$$

Since the derivative coupling obeys to the following Hellman-Feynman-type formula¹⁰⁸, it can be transformed as

$$\langle \psi_j(r; Q) | \frac{\partial}{\partial Q} | \psi_i(r; Q) \rangle = \frac{\langle \psi_j(r; Q) | \frac{\partial \hat{H}_{el}(r; Q)}{\partial Q} | \psi_i(r; Q) \rangle}{V_{ii}(Q) - V_{jj}(Q)},$$

with

$$V_{ij} = \langle \psi_j | \hat{H}_{el} | \psi_i \rangle,$$

Obviously, the derivative coupling tends to diverge for small energy gaps between electronic states (so-called “breakdown of Born-Oppenheimer approximation”). Due to this fact, adiabatic approximation cannot explain molecular dynamics around conical intersection. In other words, electronic and vibrational motions are not dynamically separated for the molecular dynamics through degenerate energy levels. Since nuclear motion is dominating dynamics on a femtosecond timescale, it is necessary to take into account of the derivative coupling in ultrafast molecular dynamics observed in this work.

The modification of adiabatic potential energy surfaces induced by derivative coupling appears as increasing and decreasing of the energy and vibrational frequencies in optical experiments. Such vibronic effect is theoretically calculated by use of diabatic basis which vanishes derivative couplings and has a weak dependence on nuclear coordinates. Since vibronic wavefunctions composed by diabatic basis, obviously, have some dependence on nuclear coordinates, it is possible to calculate the energies and vibrational frequencies by preparing a complete set of diabatic basis. In the calculation, vibronic coupling leads to an increase of the vibrational frequencies of an excited state coupled with a lower energy level while the frequencies of the lower state decrease. In the case of the carotenoids, the coupling between the two energy levels with A_g^- symmetry, optically-dark S_1 state and ground S_0 state, give rise to the C=C stretching mode having 1800 cm^{-1} which is higher than the normal C=C stretching mode ($\sim 1500 \text{ cm}^{-1}$). Although the coupling between the S_1 and S_0 state is observed in all carotenoids, the coupling of S_2 state is very selective due to the fact that optically-dark states around S_2 state for shorter-chain carotenoids exhibit a B_u^- symmetry while they were A_g^- symmetry in longer-chain carotenoids (Figure 2.4). Therefore, the dependence of the coupling on the length of the polyenes originate from the selection rule of the coupling.

On the other hand, in general, it is absent between two diabatic states with different symmetries such as $1B_u^+$ and $3A_g^-$ states, because the coupling strength and probability have a unique dependence on the symmetry and energies of the quantum states. For polyenes with a planar configuration, there is no vibronic coupling between two electronic states with different particle-hole symmetry or Pariser’s \pm labels^{109,110}. However, when it is excited to the $1B_u^+$ state, there is good chance for the conjugated chain to take a non-planar configuration due to a decrease in the C=C bond order. Then, the perfect C_{2h} and particle-hole symmetries break down. As a result, the vibronic coupling between the excited states must have appreciable non-zero value. Especially between the quasi-degenerated states, the derivative coupling between the excited states becomes too large for adiabatic description to be adequate. In addition to the Pariser’s selection rule, the symmetrical coupling between two vibronic states exist due to the coupling induced by a Q -dependent interaction^{24,110}. Therefore, the vibronic coupling between $1B_u^+$ and $1B_u^-$ states has importance in the early dynamics.

In the pump-DFWM experiment, we observed two pairs of coupled states in shorter-chain carotenoids; $2A_g^- + 1A_g^-$ and $1B_u^+ + 1B_u^-$. The vibronic effect between $2A_g^- + 1A_g^-$ leads to the C=C stretching mode around 1800 cm^{-1} as shown in Figure 3.10. Since this vibronic frequency is only observable for the S_1 state ($2A_g^-$), the time evolution of the central frequency of the vibronic mode indicates anharmonicity of the electronic energy potential. Thus, the frequency always increase in time for all pigments. On the other hand, the existence of the coupling between $1B_u^+ + 1B_u^-$ gives rise to high frequencies of C-C and C=C stretching modes in the very early time delay for neurosporene and spheroidene as shown in Figure 3.9 and Figure 3.13(a). Due to the coupling, the vibronic frequencies of the two carotenoids decrease in time. On the other hand, they increase for longer-chain carotenoids by the anharmonicity of the potential energy surface (Figure 3.9 and Figure 3.13(b)). In both cases, the vibronic frequencies of C-C, C=C stretching modes increase in later time delay by the anharmonic potential energy surface. In summary, the coupling between the B_u states is a critical factor possibly having significant importance on their dependence on environmental factors or lifetimes of quantum states in the early molecular dynamics.

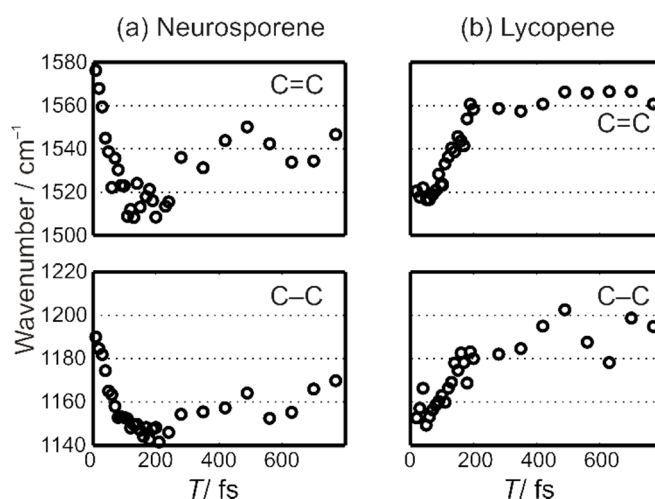


Figure 3.13: Evolution of the vibrational frequency of the C=C and C–C stretching modes for (a) neurosporene ($N = 9$) (1st column) and (b) lycopene ($N = 11$) (2nd column) between $T = 0$ and 800 fs. Spectra was obtained by Fourier transformation of transients between $\tau = 100$ and 550 fs.

3.3.6 Vibronic Coupling Enhanced via Solvation

The relationship between the coupling strength and degeneracy of the energy levels is established for a series of carotenoids having $N = 9 - 13$ in 3.3.5. The degeneracy of the B_u states has significant importance as expected by the derivative coupling. As a result, the vibronic coupling is controlled by the conjugation length which changes the overlap of the energy levels. An additional way of changing the relative energy of the B_u states is by using their different interaction with the solvent polarizability. The one-electron symmetry properties of polyenes, first used by Pariser⁷⁹ and further investigated by Pople and others,⁷⁴ distinguish electronic states as so-called plus and minus ones. While plus states are ionic states, minus states show a very strong covalent character. The existence of $1B_u^+$ state and $1B_u^-$ state leads to the modification of degeneracy between the energy levels by solvent polarizability.

Solvents with large polarizability tend to stabilize the ionic S_2 ($1B_u^+$) state and decrease its energy while the covalent states, such as the $1A_g^-$, $2A_g^-$, $3A_g^-$ and $1B_u^-$ states are barely affected in their energetic position.¹¹¹ The energy shift of ionic states in respect to covalent states can be clearly seen in the steady state absorption spectrum ($1A_g^- \rightarrow 1B_u^+$ transition) as well as in the excited state absorption of the S_1 state ($2A_g^- \rightarrow nB_u^+$ transition).³⁴ In the polyene with $N = 9 - 10$, where the S_2 and S_x states with B_u symmetry are nearly degenerate, the energy shift induced by solvent polarizability give rise to the modification of vibronic coupling.

The evolution of vibronic coupling around a conical intersection between the $1B_u^+$ and $1B_u^-$ states was detected in pump-DFWM experiment for lutein ($N \sim 10$) with three different solvents (hexane, THF and benzene). The measurements showed the modification of the vibronic coupling induced by solvent effects in the polyene (Figure 3.14). Lutein in hexane shows a frequency down-shift for both stretching modes similar to the one observed for similar open-chain carotenoids (spheroidene and neurosporene). On the other hand, lutein in benzene, a solvent with a much higher polarizability, showed a frequency up-shift similar to the observation in section 3.3.3 for longer carotenoids like lycopene and spirilloxanthin.

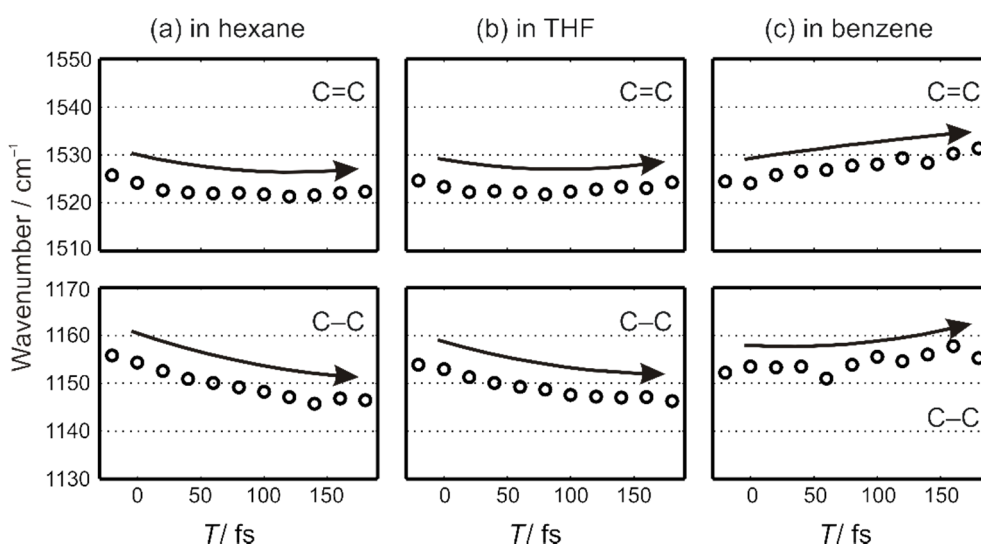


Figure 3.14: Evolution of the vibrational frequency for the C=C and C-C stretching mode for lutein in three different solvents measured with pump-DFWM. From left to the right: (a) hexane, (b) THF and (c) benzene. The arrows are a guide for the eye.

The vibrational frequency shifts of C–C and C=C stretching modes reveal two important aspects of the vibronic coupling in lutein. Firstly, the vibrational frequency shifts in THF indicate the coupling effect is much weaker in lutein than in the open-chain carotenoids with $N = 9 - 10$. The fact illustrates two influences induced by a β -ring of lutein (Figure 2.1); the C_{2h} symmetry is broken and the effective conjugated double bond length is longer than of open-chain carotenoids. The end group has significant importance in the optical character of the carotenoids. The second aspect is the requirement for the vibronic coupling between $1B_u^+$ and $1B_u^-$ states. It is indicated in the theory that a degeneracy of the vibronic levels is required for strong derivative coupling. In the case of lutein, the ionic $1B_u^+$ state is strongly stabilized in benzene which has a higher polarizability. This energy shift can be approximated by the shift of the steady state absorption spectrum, which shows for lutein that the energy of the $1B_u^+$ state decreases almost 400 cm^{-1} in comparison to the $1A_g^-$ when the solvent is shifted from hexane to benzene. Due to the stabilization effect induced by the solvent with high polarizability, the degeneracy of two vibronic levels of $1B_u^+$ and $1B_u^-$ states is broken in the carotenoids with $N = 9$ and 10 .^{49,92} As a result, the disappearance of the frequency down-shift is observed when benzene is used as a solvent.

In addition to the pump-DFWM analysis, it is interesting to have a close look on simple pump-probe measurements. The pump-probe spectra for lutein in three different solvents also surprisingly indicate the strong influence of vibronic coupling. Especially, the presence of a stronger coupling for non-polarizable solvents has an effect on the initial population dynamics as shown in Figure 3.15. A global target fitting with a three-state sequential model of data obtained with transient absorption shows an acceleration of the dynamics with the solvent polarizability. While lutein in hexane shows initial time constants of $\tau_1 = 43 \pm 5\text{ fs}$ and $\tau_2 = 35 \pm 2\text{ fs}$, benzene, a much more polarizable solvent, shows a much faster dynamics with $\tau_1 = 35 \pm 5\text{ fs}$ and $\tau_2 = 23 \pm 5\text{ fs}$ (in THF, $\tau_1 = 38 \pm 3\text{ fs}$ and $\tau_2 = 32 \pm 3\text{ fs}$). By comparing these results with the frequency shift show in Figure 3.14, it can be clearly seen that the presence of vibronic coupling between $1B_u^-$ and $1B_u^+$ states as found for e.g. lutein in hexane leads to slower population dynamics. This is not surprising since a vibronic coupling between states means a loss of pure $B_u^{+/-}$ symmetry property and may lead to complicated electronic potential surfaces and slower internal relaxations. These results raise though very interesting questions for future experiments about the role of vibronic coupling between electronic states of carotenoids embedded on natural light harvesting complexes.

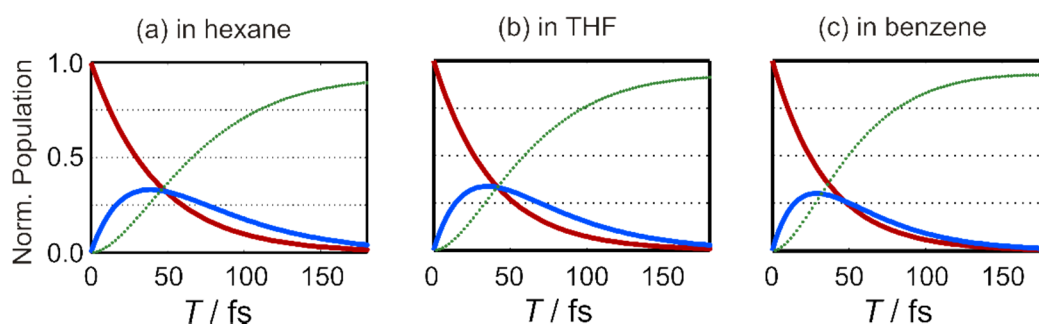


Figure 3.15: Population evolution determined by global target fitting of transient absorption of lutein using a three state sequential model in the same solvents of Figure 3.14: (a) Hexane, (b) THF and (c) Benzene.

3.4 Conclusions

The existence and non-existence of vibronic coupling are distinguished as a frequency down-shift or up-shift of C–C and C=C stretching modes as shown in Figure 3.16 in pump-DFWM experiment for a series of carotenoids with $N = 9, 10, 11$ and 13 . The multidimensional time-resolved vibrational spectroscopy directly records wavepacket motion on the excited states with vibronic effects induced by derivative coupling. These vibronic couplings become stronger in degenerate energy levels around conical intersection. Three aspects of vibronic coupling in photosynthetic polyenes are revealed in the experiments.

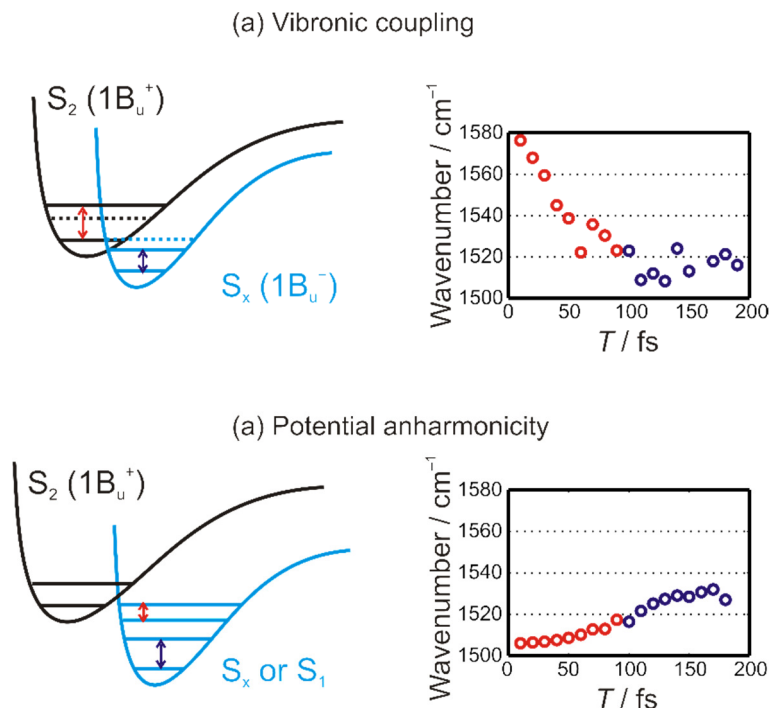


Figure 3.16: (a) Vibronic coupling and (b) potential anharmonicity were observed in pump-DFWM experiment as a frequency shift.

Firstly, vibronic coupling in the series of carotenoids (Figure 3.16a) is strongly influenced by the selection rule determined by the symmetry of excited states. The degeneracy between the $1B_u^+$ and $1B_u^-$ states in shorter-chain carotenoids leads to strong vibronic coupling, while only population relaxation in anharmonic potential-energy surfaces (Figure 3.16b) was observed in longer-chain carotenoids. The observation of the effect of the coupling between B_u states on the vibrational dynamics here agrees with previous state-of-the-art experimental work in the group of Cerullo on the interplay of population dynamics and solvation effects.¹¹² In addition, the vibrational frequencies of the excited state ($1B_u^+$) and ground state ($1A_g^-$) are reasonable compared with literature under careful analysis (Table 3.1). The existence of vibronic coupling between $1B_u^+$ and $1B_u^-$ states in shorter-chain carotenoids might be one of the reasons why the energy gap law has not been established between $1B_u^+$, $1B_u^-$, $3A_g^-$ and $2A_g^-$ states.

Secondly, the frequency up-shift around 1800 cm^{-1} , which is the C=C stretching mode of the $2A_g^-$ state strongly coupled to the ground state ($1A_g^-$), is observed in all carotenoids after the relaxation of $S_2 (1B_u^+)$ and $S_x (1B_u^-$ and $3A_g^-)$ states. The anharmonicity of the potential energy-surface of the $2A_g^-$

state is clearly described by the frequency up-shift in pump-DFWM experiment. Obviously, the vibronic coupling between $2A_g^-$ and $1A_g^-$ states is a robust feature of the photosynthetic polyenes.

Thirdly, the influences of an end-group (a β -ring in lutein) and solvent polarizability give rise to further information about vibronic coupling in photosynthetic polyenes. In the experiment, the vibronic coupling between the $1B_u^+$ and $1B_u^-$ states has a clear dependence on the solvent polarizability. The vibrational frequency shift in THF proved that a β -ring in lutein reduces the coupling strength compared with the end group of open-chain carotenoids. This is not surprising since the increasing of the number of β -ring in the polyene with $N=9$ usually gives rise to a red-shift in the stationary absorption spectrum as well as the spectra of longer-chain carotenoids having less vibronic effects between the two states. Concerning the solvent effect for the coupling, vibronic coupling between the B_u states disappears in benzene having higher polarizability. Since previous studies indicate the breakdown of the degeneracy between two vibronic levels of the B_u states in the solvent with higher polarizability, the observation is clearly understood as a vibronic effect induced by derivative coupling.

In addition, the existence of vibronic coupling on pump-probe experiment clearly indicated some conventional issues in the analysis and characterization of pump-probe spectra. The vibronic coupling extends the lifetime of the coupled states by creating complicated potential-energy surfaces. While this nature is very important for the functions of carotenoids, it often results in the spectral and temporal overlaps in pump-probe experiment.

In conclusion, the vibronic coupling takes place at very early times of the photoexcitation in the photosynthetic samples. The features of the couplings were proved for the pairs of electronic states of $B_u^+-B_u^-$ and $A_g^- - A_g^-$ not only by use of a series of carotenoids having different conjugation length but also in the different solvents.

Chapter 4

Combination of Pump-probe and Pump-DFWM Experiments by Functional Analysis

4.1 Introduction

Functional analysis (chapter 2.3) and time-resolved spectroscopies used in the investigation of molecular dynamics is usually challenging, especially on the fs timescale, since nuclear motion induces many additional phenomena which are ignored in conventional research. In fact, some analytical errors and ambiguities due to the effects induced by nuclear motion were reported^{112,113}. While the optical techniques to reveal molecular dynamics have been improved during a last few decades, the analytical techniques applied on time-resolved spectra were often based on the Singular Value Decomposition (SVD) analysis.^{36,38,56,113} As a result, some typical residuals and ambiguities induced by the analysis have caused a long-time discussion about the existence of some electronic states, such as the optically-dark excited-states of carotenoids (chapter 3).^{38,93,97} Although various aspects of molecular dynamics have been revealed by multiple-pulse optical technique, there are still some analytical issues on the investigations with the techniques on the fs timescale.

The functional analysis is important especially to analyze time-resolved spectra. In general, molecular dynamics is recorded as a multidimensional function on the optical experiments. Since it is often hard to explain the experimental data without any mathematics, functional analysis has been used to decompose the multidimensional functions. For example, Fourier transformation is one of the most frequently used mathematics. Vibrational frequencies instead of the oscillatory contributions recorded in spectroscopies can be directly seen by use of the analysis.^{27,114,115} Furthermore, the SVD analysis is an excellent technique to decompose multidimensional functions in time-resolved spectroscopies.⁵⁶ The electron-nuclear motion observed in ultrafast time-resolved spectroscopies is often explained by a sum of the components revealed by global target fitting (chapter 2.3). In the fitting, the orthogonal elements obtained by the SVD analysis are transformed with the simultaneous fitting of rate equations.^{3,116} The evaluation of the residuals and errors in the analysis usually determines the best kinetic model to explain the observation. Thus, the development of the analytical mathematics is important to obtain the correct interpretation of the data.

However, the functional analysis based on SVD, especially in ultrafast dynamics, contains three inevitable issues: (i) vibrational relaxation is often neglected, (ii) temporal and energetic overlap makes it difficult to distinguish the correct model and (iii) the interactions between electronic states (derivative coupling in Appendix F) lead to strong ambiguities and, therefore, to wrong results. The issue (i) depends on the singular values of the vibrational relaxation against the other phenomena. Since the singular values for vibrational dynamics are usually smaller compared to the electronic dynamics, the spectral broadening or some modification of vibronic structures are often neglected in the analysis. The terms of (ii) and (iii) are called rotation ambiguity or local minimum, which will appear in Chapter 4.3.3.

To clarify and to solve the issues induced by the analytic ambiguities, we propose a new approach, multimodal TRS, which is a combination of different time-resolved spectroscopic techniques. Here we demonstrate an example of multimodal TRS by use of the pump-probe and pump-DFWM

experiments. We combined the data sets obtained by the two experiments for rhodamine 6G in ethanol. The pump-probe spectroscopy is a well-known technique having high temporal and spectral resolutions. In pump-probe spectroscopy combined with functional analysis, the molecular dynamics is often described by a set of electronic states. On the other hand, pump-DFWM can selectively observe wavepacket motions on a potential energy surface by controlling resonance conditions and phase matching geometry. In the multimodal approach, the complementary use of the two multi-pulse techniques in one experimental setup allows one to decompose the signals with less ambiguity.

4.2 Experimental Methods

4.2.1 Pump-probe and Pump-DFWM Experiments

The time-resolved pump-probe and pump-DFWM experiments were carried out by using the experimental setup^{27,97,98} shown in Figure 3.2 in chapter 3.2.2. The IP pulse (18 fs) was sent to a delay line (T -delay) and a chopper to initiate the time-resolved experiment, while two DFWM pulses (13 fs) were further delayed via the piezo stages. Pump and Stokes pulses were degenerate to obtain the maximum intensity of nonlinear signals at phase matching position. DFWM beams were arranged in a folded BOXCARS geometry^{42,117} producing a spatially separate background-free signal. In the pump-DFWM experiment, the signal appearing at $k_S = k_{Pu} - k_{St} + k_{Pr}$ was observed by a pair of photomultipliers at selected wavelengths (narrow-band pass filter). The pump-probe spectroscopy is carried out with the chopped IP pulse and probe pulse detected by silicon photo-diode array.

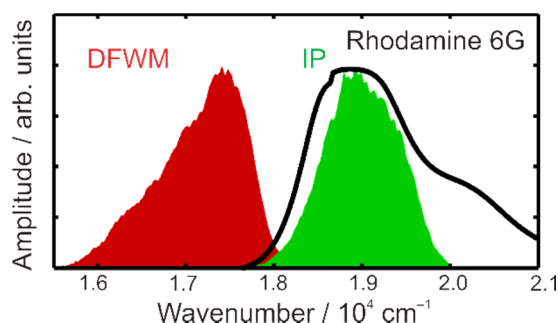


Figure 4.1: Interaction scheme of pump-probe and pump-DFWM experiments. The IP (green) and DFWM (red) excitation spectra of the time-resolved spectroscopies for (a) carotenoids and (b) Rhodamine 6G are shown. The IP pulse is resonant with the excitation from the ground state to the lowest optically-active state. The DFWM pulses are resonant with the stimulated emission from the excited states. The resonant interaction of DFWM pulses with the excited state absorption (S_1 – S_N) of the carotenoids leads to a signal order that is magnitudes larger than the non-resonant signal.

Figure 4.1 shows the excitation spectra and absorption spectra of rhodamine 6G. This pigment is famous for the excellent fluorescence quantum yield (0.95).¹¹⁸ The electronic states of rhodamine 6G in the visible regions are the well-known S_0 and S_1 singlet states as described in the literature.^{50,51,118} Thus, the experimental condition allows one to observe the relaxation dynamics from the lowest optically-active excited states (S_1) in pump-probe and pump-DFWM experiments.

4.2.2 Data Analysis

The data analysis for the data sets recorded in pump-probe and pump-DFWM experiments were performed by global target fitting and multimodal TRS explained in chapter 2.3. In both analyses, the most appropriate theoretical model was found by evaluating the error functions obtained during the analyses. The analysis of the spectral data sets were performed by applying self-coded programs based on the equations shown in chapter 2.3. All of the analyses were implemented into a MATLAB code (*Mathworks*).

4.3 Results and Discussion

4.3.1 TA spectra and Pump-DFWM signals of Rhodamine 6G

Pump probe spectra and pump-DFWM data were acquired for rhodamine 6G in ethanol. Figure 4.2 shows the time-resolved (a) transient absorption (TA) spectra and (b) vibrational spectra observed by pump-probe and pump-DFWM experiments, respectively. In the TA spectra, strong stimulated emission signals ($S_1 \rightarrow S_0$) and the ground-state bleaching were observed. The signal generation mechanisms and relevant response functions of the excited-state emission and the ground-state bleaching are described in Figure 2.9 (Chapter 2.2.3). At later T -delay, the stimulated-emission peaks became broader. On the other hand, in pump-DFWM experiment, the DFWM spectrum was carefully selected to spectrally overlap with the stimulated emission of the S_1 - S_0 transition (see Figure 4.1 and Figure 4.2a), *i.e.* it was electronically non-resonant with the S_0 - S_1 transition. Therefore, ground-state contribution under the experimental condition was orders of magnitude smaller than the electronically resonant DFWM signal generated from the electronically excited states. In Figure 4.2(b) vibrational spectra, there are three vibrational modes assigned to the C-C-C ring in-plane bend mode ($\sim 614 \text{ cm}^{-1}$)¹¹⁹, C-H out-of-plane bend mode (780 cm^{-1})¹¹⁹ and solvent mode ($\sim 881 \text{ cm}^{-1}$ which is assigned to C-C-O symmetric stretch mode of ethanol¹²⁰). The detection of a solvent mode, which only appears under the existence of the excited chromophores in Raman-based experiments, has been explained by molecular-near-field effect, which is based on the solute-solvent dipole-dipole and dipole-quadrupole interactions³⁹.

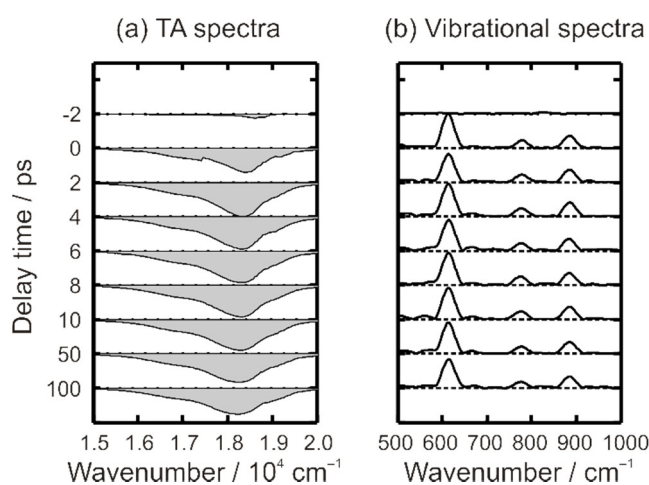


Figure 4.2: Two sets of time-resolved spectra measured for Rhodamine 6G. (a) Time-resolved transient absorption (TA) spectra observed by pump-probe spectroscopy. (b) Vibrational spectra calculated from the non-oscillatory signal of pump-DFWM transients measured at $\lambda_{\text{det}} = 560$ (17860 cm^{-1}).

The Pump-DFWM signal contains a non-oscillatory and an oscillatory contribution¹¹⁴. The oscillatory signal are converted in frequency domain by Fourier transform as shown in Figure 4.2b. Compared with pump-probe experiment, this technique follows the molecular dynamics from a different aspect. The pump-DFWM signals contains vibrational frequencies of wavepacket motion on the potential surfaces at each delay time. Furthermore, the vibrational dephasing at each delay time is recorded in the additional time axis. Thus the technique can effectively capture the coherence which is usually ignored in conventional analysis for pump-probe experiments. The detailed features of pump-DFWM signals have been described in the literature^{27,47,97} and chapter 3.3.1.

It is important to note that the IP interactions are the same in both experimental methods while the ratio of observed coherence and population terms are not the same due to the difference of probing. While pump-DFWM experiment can resolve the dynamics in much detail by multipulse probing as explained by use of the response functions in chapter 2.2.3, pump-probe experiment captures population dynamics with high temporal resolution by less amount of electronic field interaction. In other words, the two optical technique evaluate the molecular dynamics from different aspects, and this feature is necessary in multimodal approach to achieve unique minimum of error functions.

4.3.2 Singular Value Decomposition (SVD)

The Singular Value Decomposition (SVD) of TA spectra is a mathematical procedure which is typically used as a preliminary analysis giving important information for the conventional analysis and the multimodal TRS. The analysis for the pump-probe spectra determines the maximum number (k' in Eq. (8) in chapter 2.3.2) of the components in the analysis to keep the analytic ambiguity as small as possible (see Chapter 4.3.3). In more detail, the number k' is determined by the evaluation of singular values and relevant orthogonal elements. The rest of the components are excluded as a noise part to reduce the ambiguity of rotation operation in Eq. (7). The analysis is expressed as,

$$\mathbf{A} = \sum_i^k \mathbf{u}_i s_i \mathbf{v}_i^T = \sum_i^{k'} \mathbf{u}_i s_i \mathbf{v}_i^T + \mathbf{E} = \sum_j^{k'} \mathbf{u}'_j (\mathbf{v}'_j)^T + \mathbf{E} \quad , \quad (20)$$

where the matrix \mathbf{A} ($m \times n$) contains spectral data with a time axis $T(m)$ and a wavelength axis $\lambda(n)$, $\{\mathbf{v}_k\}$ and $\{\mathbf{u}_k\}$ are both normalized and orthogonal sets of eigenvectors, and the matrix \mathbf{E} ($m \times n$) contains the residual signal. In later part of the analysis, the pump-DFWM signals are also evaluated by all possible kinetic models consisted of k' elements.

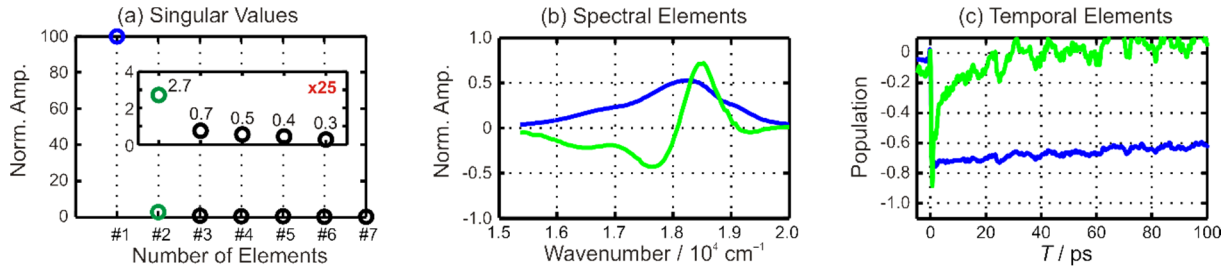


Figure 4.3: Singular value decomposition for the TA spectra within the delay time from -5 ps to 150 ps (1552 spectra) and in the spectral range 500 nm – 650 nm (120 channels). The decomposition gives (a) singular values, (b) spectral elements and (c) time evolutions of the orthogonal elements. The 1st and 2nd components are colored with blue and green, respectively.

The Figure 4.3 shows SVD for the transient absorption data set of rhodamine 6G shown in Figure 4.2 (a). The singular values and relevant orthogonal vectors indicate the existence of two components representing most of the dynamical changes in the spectra. Figure 4.3b and c show the main spectral and temporal elements of the spectra, respectively. Although the original spectra can be reconstituted with all components of the orthogonal bases, we used only two main contributions to avoid rotation ambiguity (Chapter 2.3.5). Since the singular values of two components account up to 93.6 % of all of the singular values, most of the dynamical evolution and spectroscopic features are conserved

in the analysis. The rest of the signals are discarded as a noise before rotation operation. Therefore, the analysis is performed for two kinetic models, (a) two-state parallel model and (b) the two-state sequential model as shown in Figure 4.4. The kinetic elements $\{p_i\}$ of the parallel model with two elements, S_1 and S_2 , are given by the convolution between the rate equation and Instrumental Response Function (IRF) expressed as,

$$p_1(T) = r[S_1]_0 e^{-\frac{T}{\tau_1}} * \text{IRF} \quad , \quad (21)$$

$$p_2(T) = (1 - r)[S_1]_0 e^{-\frac{T}{\tau_2}} * \text{IRF} \quad , \quad (22)$$

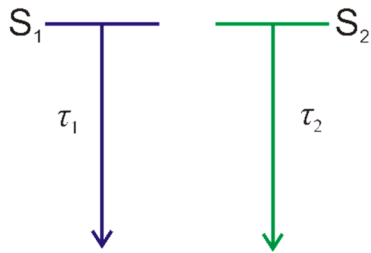
where τ_n is the lifetime, IRF is the instrumental response function and r determines the ratio of the components. The kinetic elements for sequential model are given by

$$p_1(T) = [S_1]_0 e^{-k_1 T} * \text{IRF} \quad , \quad (23)$$

$$p_2(T) = \left\{ \frac{k_1}{k_2 - k_1} [S_1]_0 (e^{-k_1 T} - e^{-k_2 T}) \right\} * \text{IRF} \quad . \quad (24)$$

where $k_n = 1/\tau_n$ (exponential decay time constant). A detailed explanation about the kinetic models is available in Chapter 2.3 and Appendix E.

(a) Two-state parallel model



(d) Two-state sequential model

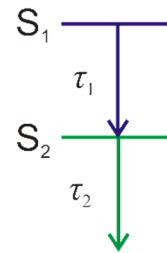


Figure 4.4: (a) Two-state parallel and (b) two-state sequential model for global target fitting.

4.3.3 Functional Analysis and Ambiguities

In global target fitting, all possible kinetic models are evaluated by use of the two error functions E_k and E_s . The kinetic model error (E_k) describes the residuals between the time profiles of the Species-Associated Difference Spectra (SADS) and a theoretical kinetic model (Chapter 2.3.4, Eq. 11). The 3rd-order signal error (E_s) contains the residuals between the raw spectra and reconstituted spectra (Chapter 2.3.4, Eq. 10). There are two important relationships between the two error functions and the accuracy and precision of global target fitting. For example, if a kinetic model used in global target fitting gives a temporal behavior which diverse from the correct dynamics as shown in Figure 4.5a, in other words when the value of the E_k is huge, the time constant determined by the fitting would be away from the correct value. Moreover, if the huge residuals for the reconstituted spectra are allowed, in other words when the error value of the E_s is huge, there are many kinetic models which can fit the original data with the same amounts of the residuals as shown in Figure 4.5b. As a result, the precision of global target fitting often becomes worse under the existence of the huge residuals evaluated by the error function E_s . In addition, such tendencies of the error functions evoke some weakness in the analysis. In this section, the two issues of global target fitting, which are rotation ambiguity and local minimum, are described by comparing three fitting results obtained for the two-state parallel model, the two-state sequential model and the three-state model.

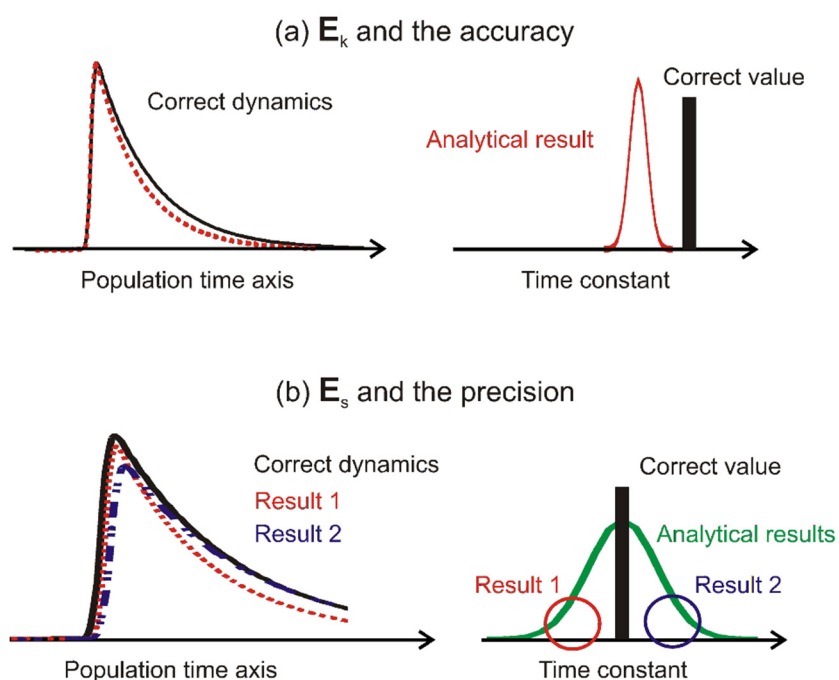


Figure 4.5: The relationship between the error functions and analytical resultants. (a) E_k is directly connected to the accuracy of the analysis. (b) There are various patterns of the analytical results belonging to the same value of E_s .

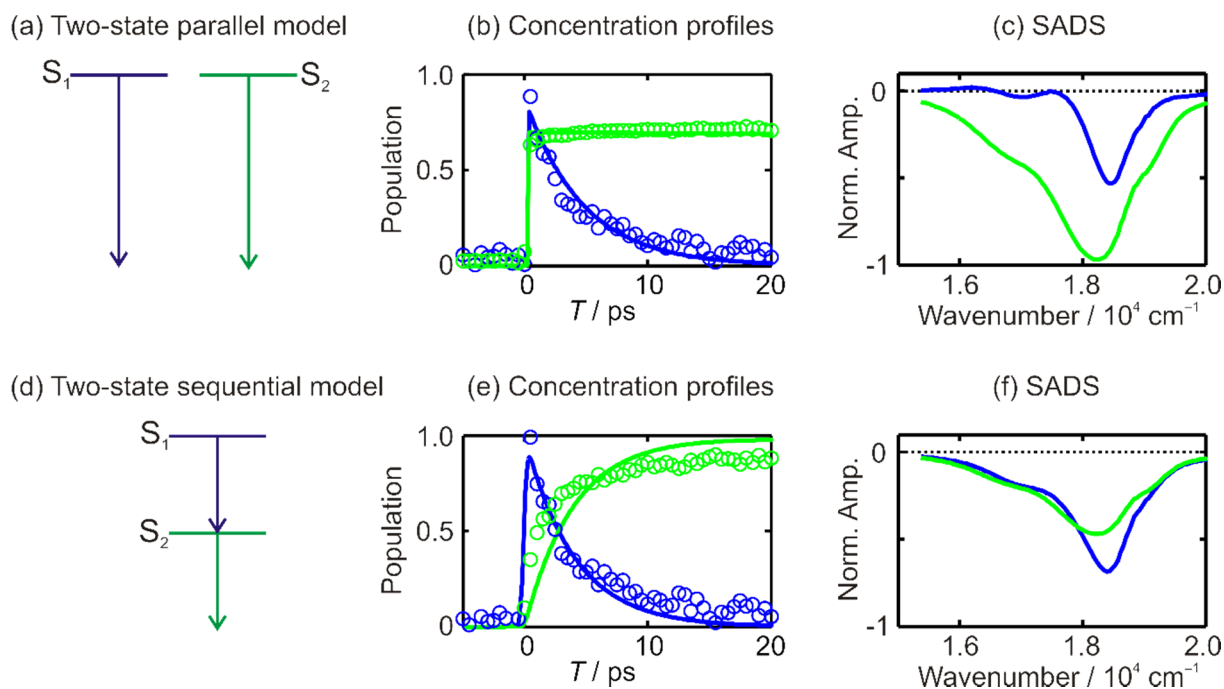


Figure 4.6: Global target fitting with (a)-(c) two-state parallel model or (d)-(f) two-state sequential model. (a), (d) Both kinetic models have two states, S_1 (blue) and S_2 (green). (b), (e) The concentration profiles of the two states. The experimental data are shown in circles. (c), (f) Species-Associated Difference Spectra (SADS) of each component.

Figure 4.6 shows the global target fitting results with the SADS and their time evolutions for each model. The error values of each analysis were $E_k = 2.31 \times 10^{-2}$ and $E_s = 3.64 \times 10^{-2}$ for the parallel model and $E_k = 6.67 \times 10^{-2}$ and $E_s = 2.87 \times 10^{-2}$ for the sequential model as shown in Table 4.1. In both cases, the reconstituted spectra contain more than 96 % of the spectral intensities of the original spectra. Although the 3rd-order error, E_s , is smaller in the sequential model than in the parallel model, the parallel model has a smaller kinetic model error, E_k , than the sequential model. Thus, the analysis cannot exclusively conclude which model is the correct one.

Table 4.1: The error values of the two error functions (E_k and E_s) calculated in global target fitting for two-state parallel, two-state sequential and three-state models used in Figure 4.6 and 4.7.

	$E_k (\times 10^{-2})$	$E_s (\times 10^{-2})$	$E_k + E_s (\times 10^{-2})$
Two-state parallel model	2.31	3.64	5.95
Two-state sequential model	6.67	2.87	9.54
Three-state model	2.53	2.53	5.06

Although in this kind of analysis it is possible to reduce the error values by adding a new component in the model, this approach always induces a strong rotation ambiguity (detailed explanation is written in the next paragraph for Figure 4.8) which detracts the analytic precisions significantly. For example, the combination of the two-state parallel and the two-state sequential model leads to the three-state model shown in Figure 4.7. The combination of the two-state models, resulting in a three-state

model, significantly reduced the error values to $E_k = 2.53 \times 10^{-2}$ and $E_s = 2.53 \times 10^{-2}$. As shown in Table 4.1, both error values are smaller than the values in the other two-state models shown in Figure 4.6. In addition, it might be possible to determine the correct model from the total error given by $E_k + E_s$. However, it is dangerous to determine the correct model only with the error values because the precision and accuracy of the analysis are also important as well as the error values. In other words, there can be some analytical results having the same or very similar error values in the analysis. In fact, there are several resultants having similar error values in the analysis with the three-state model due to rotation ambiguity and local minimum.

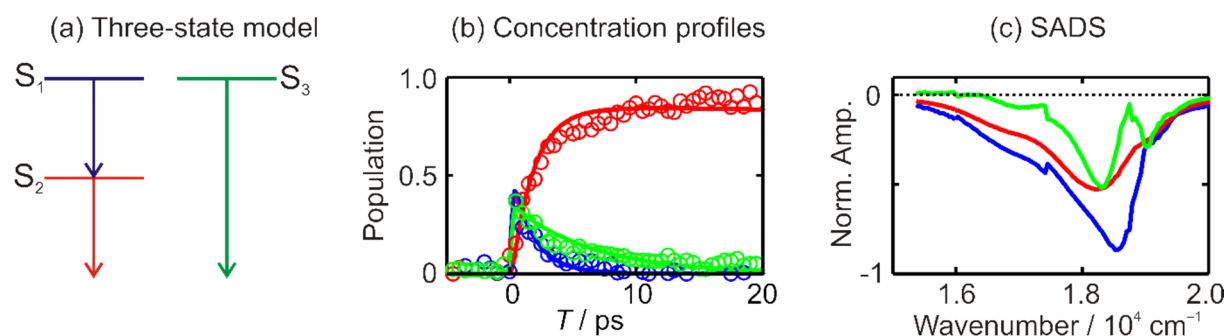


Figure 4.7: Global target analysis with three state model. (a) The kinetic model has sequentially aligned two states, S_1 (blue) and S_2 (red) with an individual state, S_3 (red). (b) The concentration profiles of three states. The experimental data are shown in circles. (c) The spectral elements for the states.

The rotation ambiguity and local minimum are main sources which detract the precision of each parameter in this kind of multi-component analyses. Both of them are inevitable and intrinsic features of the analysis. Firstly, the rotation ambiguity is induced by the spectral and temporal overlap between the components in the analysis. Since the S_1 (blue) and S_3 (green) components are almost perfectly overlapped both on the time and energy axes in the three-state model (Figure 4.7), the analysis with the three-state model is a good example to visualize the rotation ambiguity. Under the existence of a strong overlap between the components, there are possibilities of a certain result which can be created by a different C-matrix. The C-matrix performs the rotation operation for the orthogonal elements (Figure 4.3b,c) extracted by the SVD analysis of the original signals to reconstitute the spectra (detailed explanation is written in chapter 2.3.2 and Figure 2.12). Figure 4.8(a) shows the kinetic model error values (E_k) for the C-matrix elements (c_{11} and c_{32}). The quality of a fit model can be judged by looking at all the parameters of each error function. In the ideal case one would like to have a unique minimum on every axis. However, the error values don't change on the c_{32} axis although the values have a minimum on the c_{11} axis. It is important to note that four parameters, c_{12} , c_{13} , c_{32} and c_{33} , mainly create the S_1 and S_3 components. Since the small change induced by c_{32} on the S_1 or S_3 components can be compensated by the other parameters (c_{12} , c_{13} and c_{33}), the error values on the c_{32} axis don't change so much. The components generated by such optimization often don't have any physical meaning, and they are, most likely, just some artificial components. Since the dimension of the C-matrix with n components analysis is n^2 , increasing the number of the components can easily occur the rotation ambiguity. Thus, as mentioned in the Chapter 2.3, the analysis should be performed with a minimum number of components. Of course, the precision of the analysis is significantly detracted by the rotation ambiguity. On the other hand, the global target fitting for degenerate energy levels tends to have a bad precision and a strong rotation ambiguity due to the strong overlap of the components. Therefore, the analytic result with the three-state model is not reliable even though it has the smallest error values.

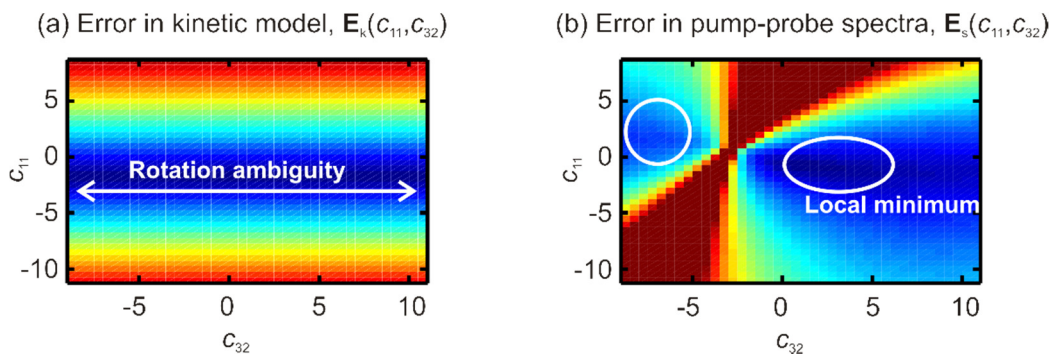


Figure 4.8: The rotation ambiguity and local minimum observed in the functional analysis with three-state model (Figure 4.7). The error values increase from cold color (blue) to hot color (red). The center, $c_{11} = c_{32} = 0$, is the convergence point. The matrix elements of c_{11} and c_{32} present two of the parameters to create S_1 and S_3 states. (a) Rotation ambiguity appears in the axis of c_{32} . The error value are the same in any value of c_{32} in this region. (b) There are two spots having small error values around the convergence point.

Secondly, the other ambiguity, local minimum, has a strong influence on the accuracy of the analysis. In Figure 4.8 (b), the local minimum is shown on the error function E_s for the c_{11} and c_{32} coordinates. There are two spots which can converge the error function. In general, there can be many local minimums in the analysis. Especially, using a kinetic model with many components tends to generate many local minimums because the calculations having high degree-of-freedom can fit the data by many different combinations of the parameters. In other words, many patterns of the fitting results could have the same error values due to the rotation ambiguity and local minimum as described in Figure 4.8.

The ambiguities appearing on the C-matrix elements have a strong influence on the determination of the kinetic time constants (τ_n). While in the ideal case the kinetic time constants τ_n should be uniquely determined for a kinetic model, the time constants are often not uniquely determined due to the ambiguities as shown in Figure 4.8. In Figure 4.9, the error values of E_s , E_k and $E_s + E_k$ were calculated on the c_{11} and τ_1 axes for the three types of kinetic models which are (a) two-state parallel, (b) two-state sequential and (c) three-state models. The two parameters c_{11} and τ_1 have a major impact on the determination of the time constant and SADS of the first component (the component S_1 in Figure 4.6 and 4.7).

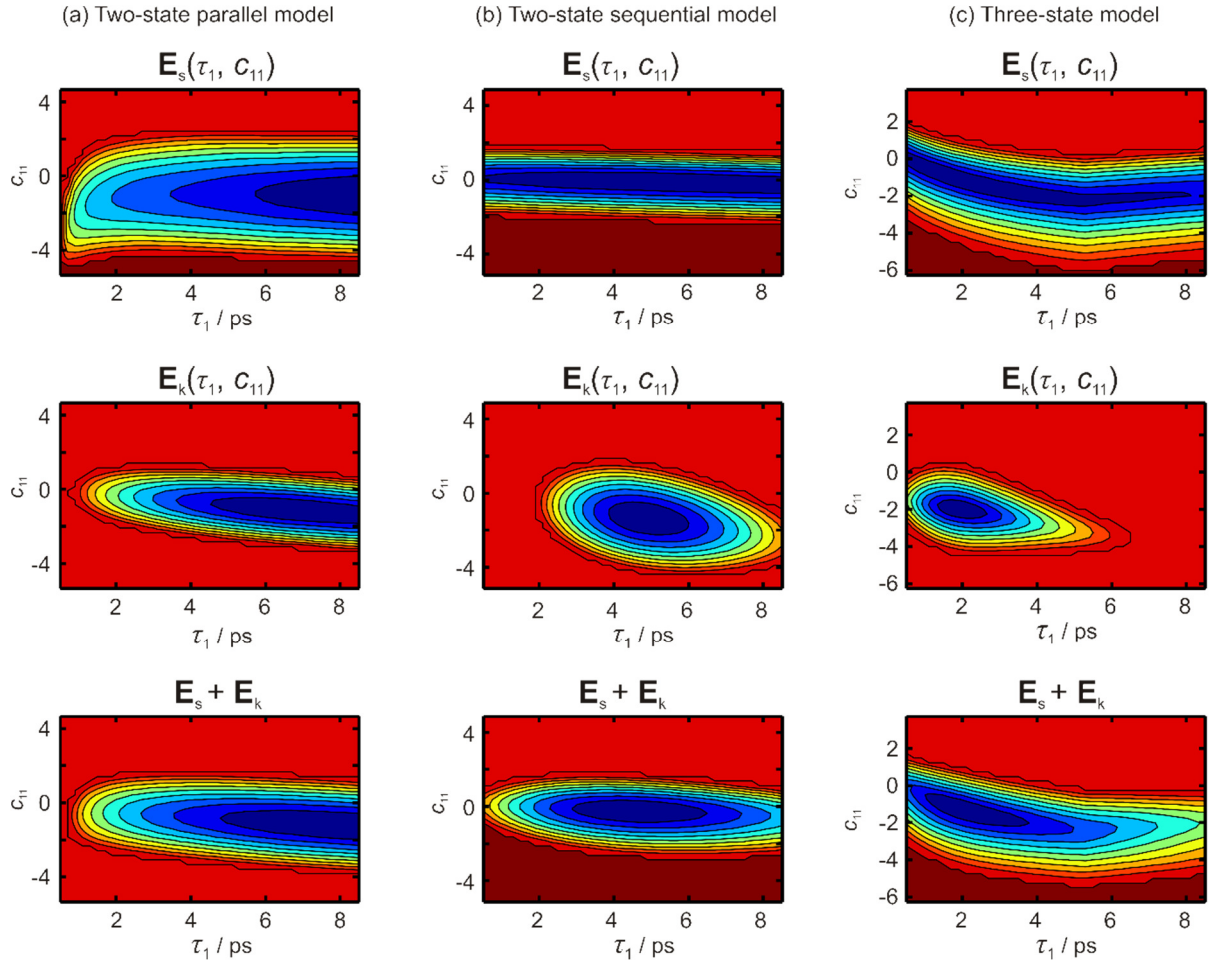


Figure 4.9: The error distributions in global target fitting. The two error functions E_s and E_k in (a) two-state parallel model, (b) two-state sequential model or (c) three-state model are shown on the c_{11} and k_1 axis. The error values increase from cold color (blue) to hot color (red).

As shown in Figure 4.9, the error functions E_s , E_k and $E_s + E_k$ have a region where the error value is much smaller than in other regions. It is important to note that the position of the minimum error value on the c_{11} axis is strongly influenced by the other C-matrix elements due to the local minimum as shown in Figure 4.8(b). In other words, the value of c_{11} having small error values can be shifted by the other c_{ij} values. On the other hand, the kinetic time constant τ_1 can be determined by the E_k with some precision of 4 ~ 10 ps which are roughly estimated by the width of the region giving the minimum error value on the τ_1 axis in Figure 4.9. However, in the total error function $E_s + E_k$ (Figure 4.9 bottom panels), the region giving small error values on the τ_1 axis becomes broader. Although it is possible to determine the kinetic time constants only with the E_k , this approach often increases the value of the E_s . Since many kinds of kinetic models can be fitted with the raw spectra with a large spectral residuals (E_s), too much weighting on the E_k leads to the bad precision in the analysis as explained in Figure 4.5(b). In addition, since the ambiguities appearing on the c_{ij} are a part of the inherent features of the analysis, it is impossible to improve the error function E_s in SVD analysis. Therefore, it is required to evaluate the kinetic models in the other spectral data sets recorded under the comparable experimental condition.

4.3.4 Error Functions in Multimodal TRS

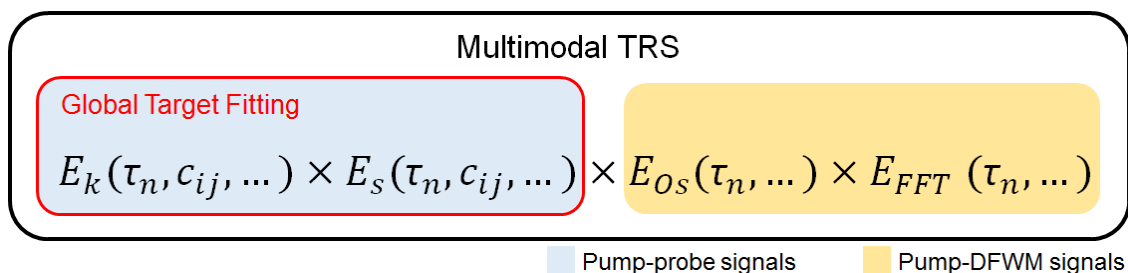


Figure 4.10: The four error functions, E_k , E_s , E_{OS} and E_{FFT} , are evaluated in the pump-probe spectra and in the pump-DFWM transients. The kinetic time constants in global target fitting are evaluated only in the pump-probe spectra while they are also optimized for the pump-DFWM transients in multimodal TRS. The C-matrix elements (c_{ij}) only appear in the global target fitting.

Multimodal TRS, consisting of pump-probe and pump-DFWM experiments, can overcome the ambiguities by use of the two additional error functions (E_{OS} and E_{FFT}) calculated by the fitting of pump-DFWM signals. Figure 4.10 shows the error functions in global target fitting and in multimodal TRS. While global target fitting is carried out with the two error functions (E_k and E_s) which were briefly explained in Chapter 4.3.3 and defined in Chapter 2.3.4 Eq. (10)-(11), there are two additional error functions (E_{OS} and E_{FFT}) in multimodal TRS.

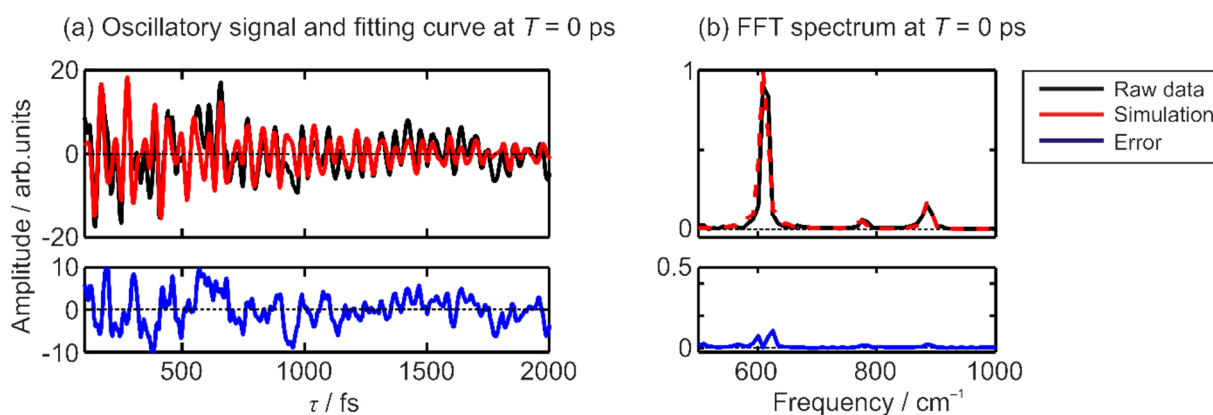


Figure 4.11: The pump-DFWM transient (black, at $T = 0$) on the τ axis is fitted by the simulated signal (red) in multimodal TRS. The residuals (blue) are mainly originated from the vibrational frequencies $< 500 \text{ cm}^{-1}$ or $> 1000 \text{ cm}^{-1}$.

The two error functions (E_{OS} and E_{FFT}) for pump-DFWM signals evaluate kinetic models by the simulation of vibrational spectra recorded by pump-DFWM experiment. Figure 4.11 shows the fitting of the pump-DFWM signal observed at $T = 0$. The error function E_{OS} contains the residuals (Figure 4.11a, blue) which are calculated by taking differences between the raw signal (black) and the simulated signals (red). On the other hand, the error function E_{FFT} contains the residuals of (Figure 4.11b, blue) of the Fourier transformed spectrum of the oscillatory signal. As shown in Figure 4.11b, the residuals of the oscillatory signal (Figure 4.11a, blue) barely contains the vibrational modes used in the simulation. Since vibrational spectra are strongly influenced by molecular dynamics, the E_{FFT} is

sensitive to the time constants for each components appearing in the dynamics. On the other hand, the E_{Os} has an importance to remove wrong kinetic models by evaluating the simulated signals on the τ axis.

Regarding the later T delay, the three vibrational modes are effectively extracted by the fitting curves as shown in Figure 4.12. The residuals on the oscillatory signals don't contains the vibrational frequencies of rhodamine 6G as shown in Figure 4.12b,d,f.

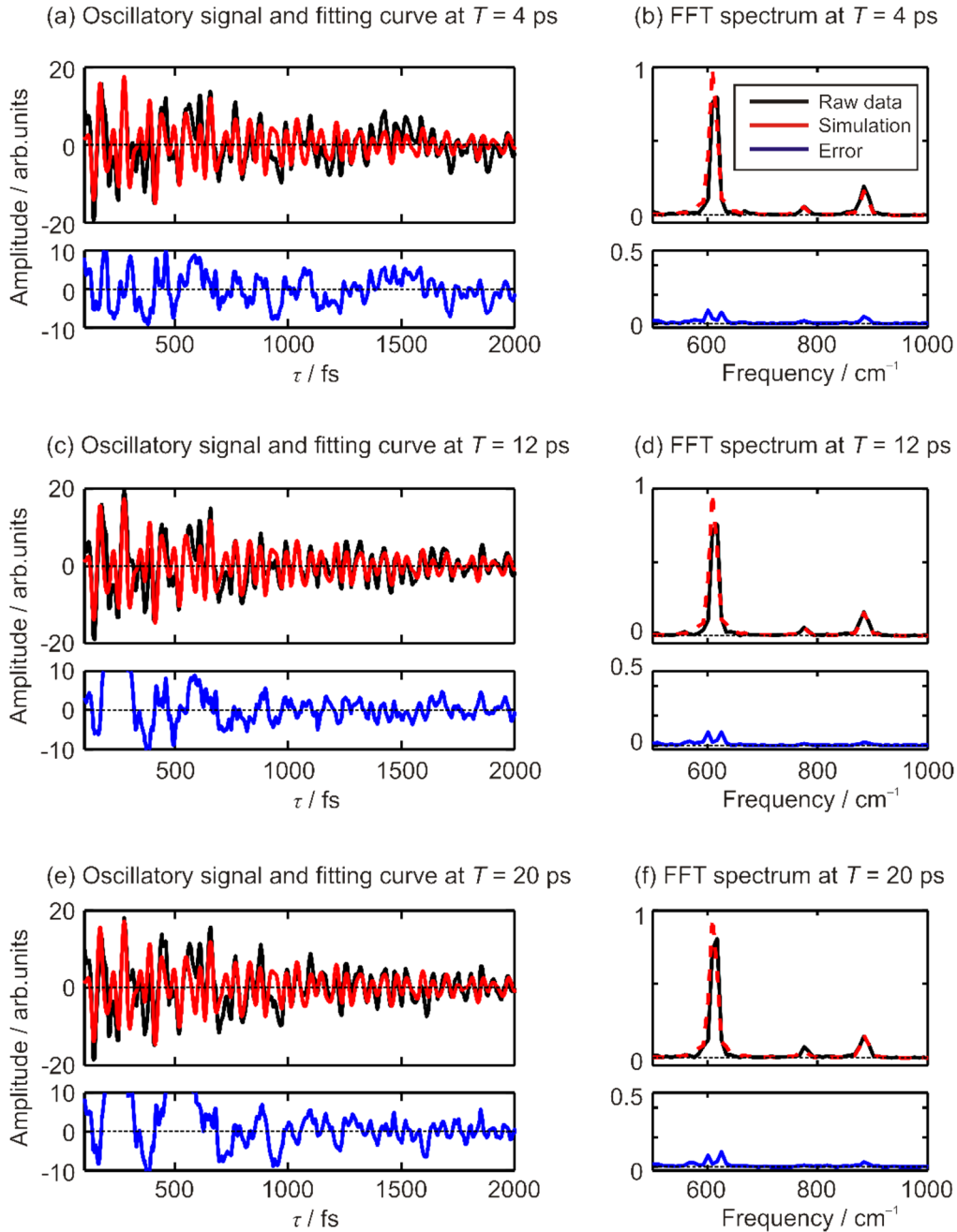


Figure 4.12: The pump-DFWM transient (black, at $T = 0$) on the τ axis is fitted to obtain E_{Os} and E_{FFT} . The residuals (blue) are mainly originated from the vibrational frequencies $< 500 \text{ cm}^{-1}$ or $> 1000 \text{ cm}^{-1}$.

By the combination of the four error functions (E_k , E_s , E_{OS} and E_{FFT}), it is possible to evaluate kinetic models not only by pump-probe signals but also by pump-DFWM signals. Figure 4.13 shows the error values of the E_{OS} , E_{FFT} and $E_{OS} + E_{FFT}$ on the c_{11} and τ_1 axes for (a) two-state parallel and (b) two-state sequential models. The $E_s + E_k$ shown in Figure 4.13 are calculated by exactly the same functions used in global target fitting while there is a slight difference due to the parameters used in the analysis. Since E_{OS} and E_{FFT} don't have any C-matrix elements, they have always the same value on the c_{ij} axis. In the comparison between $E_s + E_k$ and $E_{OS} + E_{FFT}$, the $E_s + E_k$ in global target fitting have a broad bandwidth for the small error values on the τ_1 axis. However, the two error functions $E_{OS} + E_{FFT}$ are very sensitive to kinetic time constant τ_1 . In addition, it is important to note that the $E_s + E_k$ and $E_{OS} + E_{FFT}$ are connected through the evaluation of kinetic time constants as shown in Figure 2.16 in chapter 2.3.6.

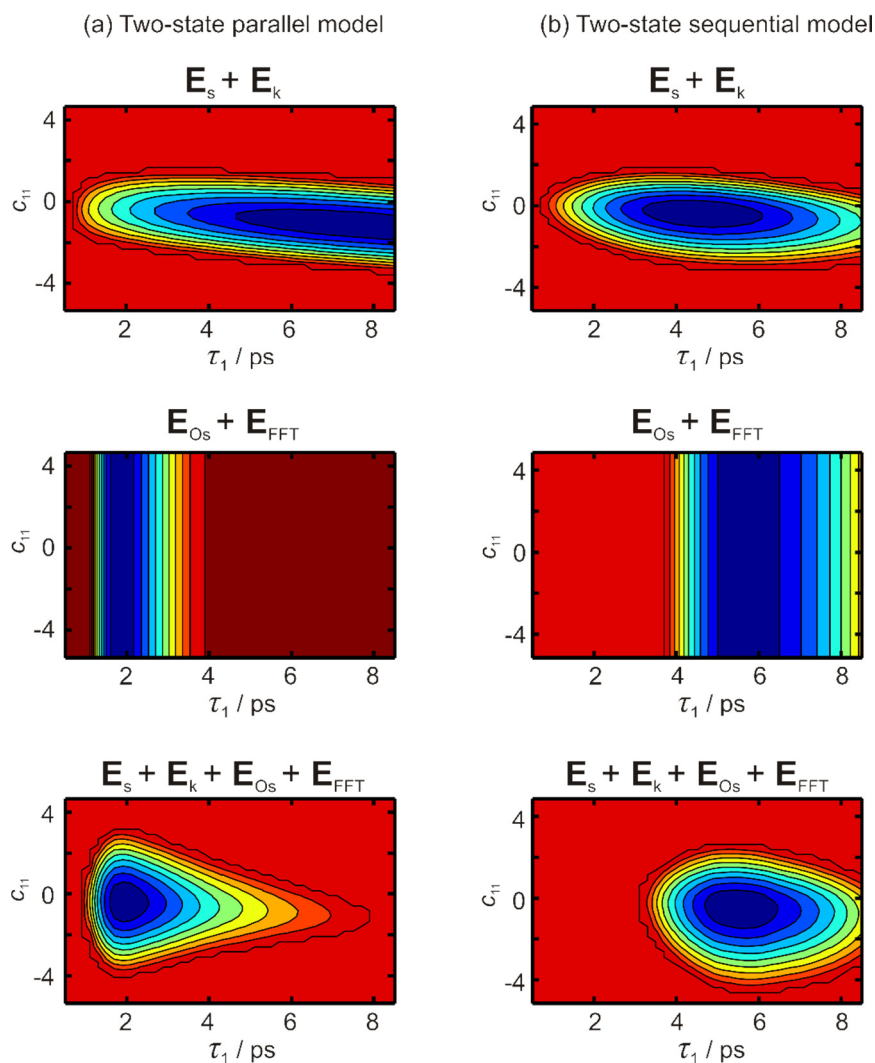


Figure 4.13: The error distributions in multimodal TRS. The two error functions E_s , E_k , E_{OS} and E_{FFT} in (a) two-state parallel model or (b) two-state sequential model are shown on the c_{11} and k_1 axis. The error values increase from cold color (blue) to hot color (red). The weights of the error functions, $E_s + E_k$ and $E_{OS} + E_{FFT}$, are set as 10:1 which is based on the changing of the error values in each axis.

In both kinetic models, the time constant τ_1 observed in pump-DFWM experiment is clearly indicated by the unique minimums of the $E_{OS} + E_{FFT}$ on the τ_1 axis. As a result, multimodal TRS can combine the two experimental results by the evaluation of kinetic models. In other words, each kinetic

model gives rise to some error values calculated by the error functions which fit pump-probe and pump-DFWM signals. Since the appearance of the $E_s + E_k$ can vary due to the local minimum and the rotational ambiguity, the error values of the $E_{OS} + E_{FFT}$ have an important index to determine the appropriate kinetic model. The importance of the evaluation of kinetic models in the two different experimental results is discussed in the next section.

4.3.5 Multimodal TRS for Rhodamine 6G

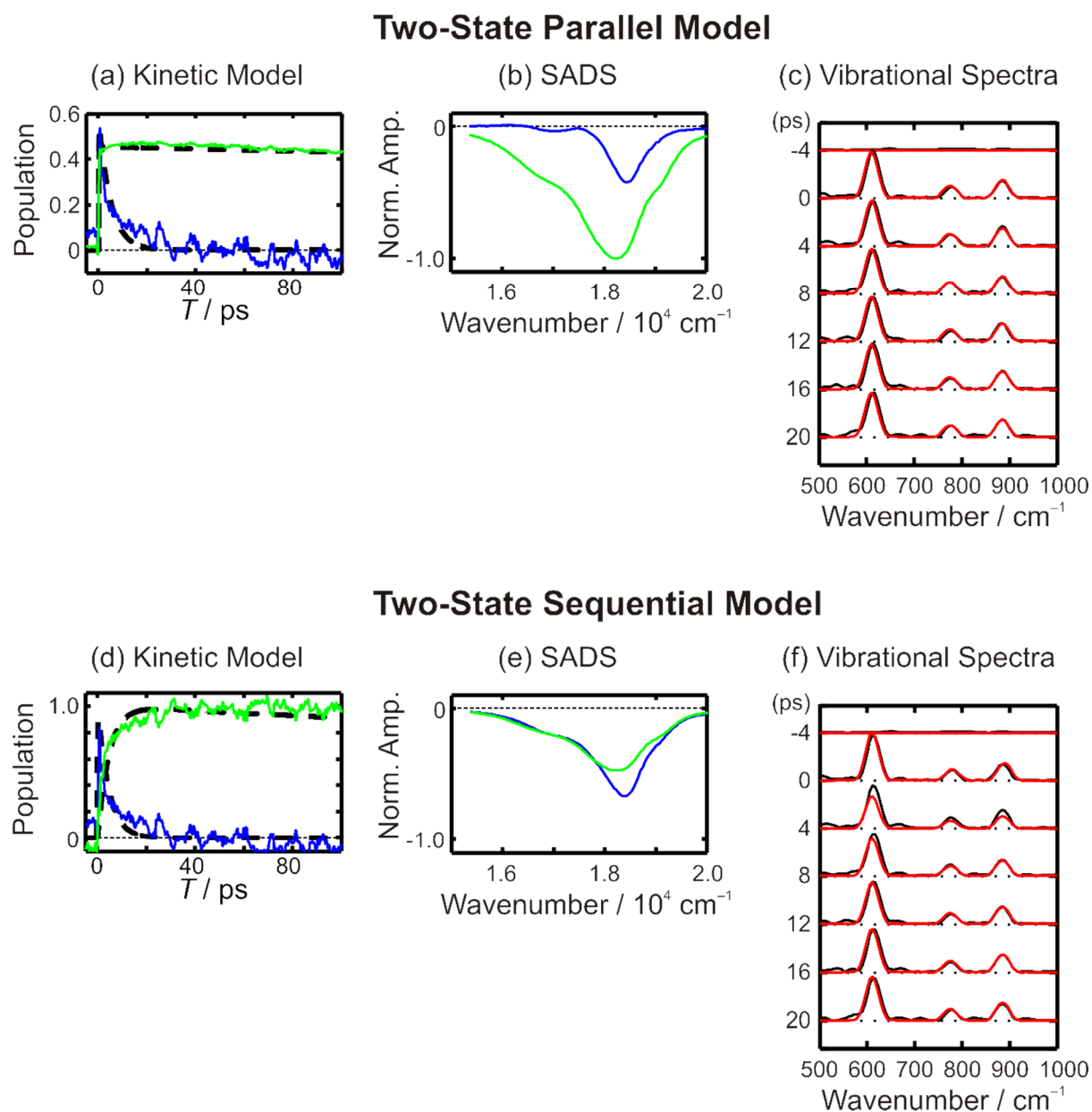


Figure 4.14: Multimodal TRS for rhodamine 6G with (a)-(c) two-state parallel model and (d)-(f) two-state sequential model. Stimulated emission spectra in pump-probe spectroscopy were decomposed into (a), (d) temporal elements and (b), (e) spectral elements. (c), (f) The short-lived 1st component (blue, ~ 5 ps) and long-lived 2nd component (green, > 2 ns) are separated by the simultaneous fitting with kinetic models (black broken line in (a) and (d)). The vibrational spectra (black solid line) were simulated for each model as shown in red lines.

As described in the previous sections, the multimodal TRS can determine the molecular dynamics by use of the four error functions (E_s , E_k , E_{OS} and E_{FFT}) which combines pump-probe and pump-DFWM signals. The evaluation of kinetic models in the two different optical signals, at least, leads to the common parts of molecular dynamics observed in the two experiments. Thus, it is possible to exclude wrong kinetic models much easier compared with the conventional global target fitting.

Figure 4.14 shows analytical results of multimodal TRS for the pump-probe and pump-DFWM signals of rhodamine 6G (Figure 4.2) by use of (a)-(c) two-state parallel model and (d)-(f) two-state sequential model. The error values of pump-probe part ($E_s + E_k$) and pump-DFWM part ($E_{OS} + E_{FFT}$) are summarized on Table 4.2. In the results, there are clear differences on the SADS and their time profiles. While the oscillatory contribution only appears on the short-lived component in the parallel model (Figure 4.14a, blue), the oscillatory signal appears on both components in the sequential model (Figure 4.14d). In addition, the SADS of the short-lived component in the parallel model (Figure 4.14b, blue) is totally different compared with the other SADS.

Table 4.2: The error values of $E_s + E_k$ and $E_{OS} + E_{FFT}$ in multimodal TRS in comparison with the error values of classic global target fitting. Two-state parallel and two-state sequential models are evaluated in the analysis. GTF – global target fitting, MTRS – multimodal TRS.

	Two-state models	Pump-probe			Pump-DFWM
		E_k	E_s	$E_k + E_s$	$E_{OS} + E_{FFT}$
GTF	Parallel	2.31	3.64	5.95	---
	Sequential	6.67	2.87	9.54	---
MTRS	Parallel	2.56	3.91	6.47	105.4
	Sequential	7.51	2.81	10.31	120.39

In the fitting of the vibrational spectra (Figure 4.14c,f), there are less residuals in the parallel model compared with the sequential model especially around $T = 4$ ps. The difference clearly appeared on the amplitudes of the three modes (614, 780 and 881 cm^{-1}) in the population time axis as shown in Figure 4.15 and the number of the error values of $E_{OS} + E_{FFT}$ as shown in Table 4.2. Thus, the sequential model is not suitable to explain the pump-DFWM signals. In fact, the error values of $E_{OS} + E_{FFT}$ for pump-DFWM signals with parallel model is by 10 – 15 % better than with the sequential model as shown in Table 4.2. Since the pump-DFWM signals contain strong low-frequency contributions which are not simulated, the error values of $E_{OS} + E_{FFT}$ is much bigger than the values of $E_s + E_k$. However, it is possible to evaluate each kinetic models by the four error functions.

It is important to note that there are some difficulties to achieve a unique solution in the conventional global target fitting (GTF). The error values for GTF shown in Table 4.2 indicated that the parallel model gives rise to better values of E_k and the total error value $E_s + E_k$. However, the E_s indicates the sequential model fits the pump-probe spectra better than the parallel model. As explained in Figure 4.5b, the E_s is sensitive to the precision of the fitting. Thus, it is difficult to conclude which model fits better in global target fitting. On the other hand, in multimodal TRS, the additional error functions $E_{OS} + E_{FFT}$, which evaluate the pump-DFWM signals, clearly indicates that the parallel model is suitable for the signals. Therefore, evaluating by the two experimental data sets, which were measured by pump-probe and pump-DFWM experiments, the analytical result with the parallel model (Figure 4.14a-c) is the adequate solution in the analysis.

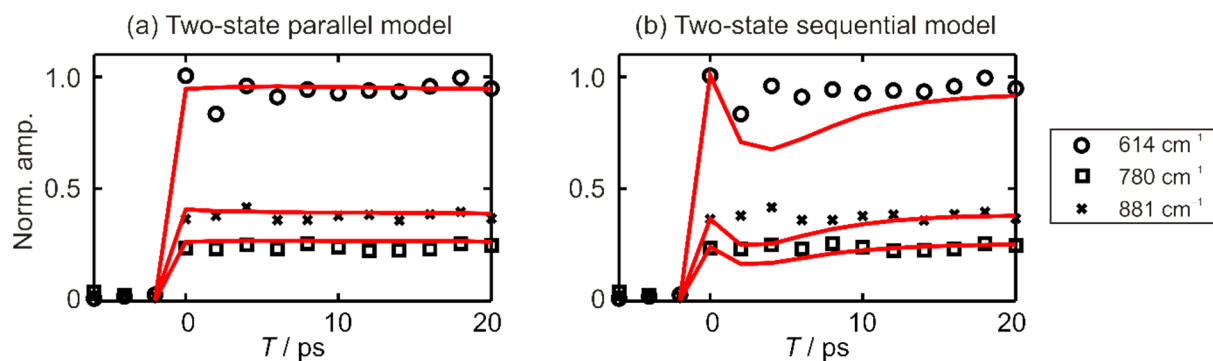
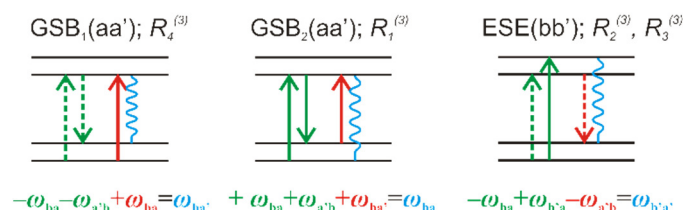


Figure 4.15: The amplitudes of C-C-C ring in-plane bending $\sim 614 \text{ cm}^{-1}$, C-H out-of-plane bend mode $\sim 780 \text{ cm}^{-1}$ and C-C-O symmetric stretching mode of ethanol $\sim 881 \text{ cm}^{-1}$. The simulated curves (red) for (a) parallel model and (b) sequential model fit the amplitudes of pump-DFWM signals for each peak.

The kinetic elements and the SADS (Figure 4.14a and b) obtained by multimodal TRS show some interesting features. The oscillatory contribution only appears in the short-lived component while the long-lived component only contains nonoscillatory contribution. The lifetimes of each component is 5 ps for the short-lived component and $> 2 \text{ ns}$ for the long-lived component.

Oscillatory signals (SADS1)



Long-lived component (SADS2)

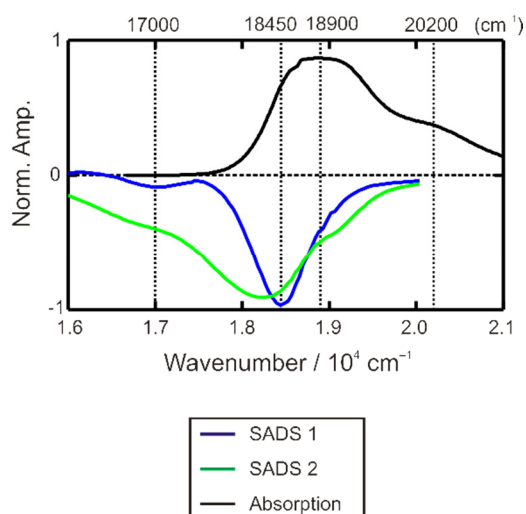
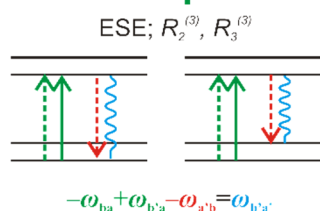


Figure 4.16: The two components obtained by multimodal TRS with the relevant response functions. The short-lived component (SADS 1, blue) appears at 17000 and 18450 cm^{-1} , while the long-lived component is the emission spectrum from S_1 state. The stationary absorption spectrum is also shown as a reference. GSB – ground-state bleaching, ESE – excited-state emission.

Furthermore, the two components obtained by multimodal TRS can be explained by the common terms of the response functions of the 3rd-order and 5th-order nonlinear spectroscopies (the response functions are described in Figure 2.9 and 2.10). Figure 4.16 shows the SADS calculated by the analysis. For example, the corresponding SADS for the short-lived component (Figure 4.16, SADS 1) contains the emissions with a narrow spectral band appearing at 17000 cm^{-1} ($1 \leftarrow 0$) and 18450 cm^{-1} ($0 \leftarrow 0$) where the coherence can be observed through the four-wave mixing sequences. On the other hand,

the stimulated emission and ground-state bleaching are stored in the long-lived component. The SADS 2 clearly contains the vibronic structure with the Stokes shift $\sim 700 \text{ cm}^{-1}$. The stationary absorption spectrum have a vibronic structure of 18900 cm^{-1} ($0 \rightarrow 0$) and 20200 cm^{-1} ($0 \rightarrow 1$). Thus, the energy separation of the vibrational levels on the stationary absorption spectrum is $\sim 1300 \text{ cm}^{-1}$ while it is $\sim 1450 \text{ cm}^{-1}$ in the emission signal.

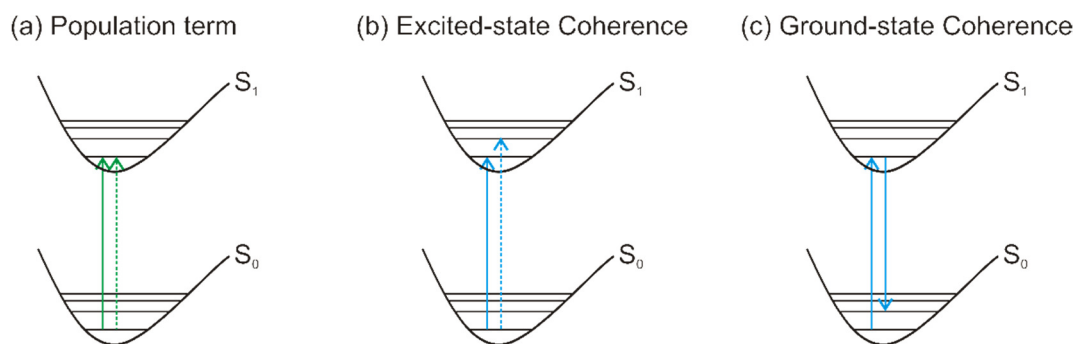


Figure 4.17: Interpretation of the result obtained by multimodal TRS for Rhodamine 6G. The interaction of the initial pump pulse from bra side (solid line) and ket side (broken line) are shown. (a) Long-lived component having a typical stimulated emission spectrum is the population term of the S_1 state. The oscillatory shape in the time evolution of stimulated emission having a spectrum with narrow shape indicates the preparation of coherence on (b) excited-state or (c) ground-state.

By combining pump-probe and pump-DFWM experiments, which have different probing mechanisms while the initial pump interactions are the same, multimodal TRS determined the kinetic model commonly observed in the two optical experiments as summarized in Figure 4.17. The observation and the interpretation of the results are reasonable in comparison of the literature^{50,51}.

4.4 Conclusions

The multimodal approach by use of pump-probe and pump-DFWM experiments indicated that the coherence can be separated by the functional analysis based on the response functions and the resonance conditions. In this work, we demonstrated the separation of the population term and the coherent term of the TA spectra. The evolutionary calculations for the two data sets clearly identified the correct model which was not possible applying only a single set of spectra. In conclusion, the new method has effectively overcome the issues originated from the rotation ambiguity and local minimum.

Furthermore, in multimodal TRS the error functions have minimum error values to determine the adequate model. Since two optical techniques share some response functions restricted by resonance conditions, multimodal TRS can overcome many local minimums and rotation ambiguities appearing in the conventional analysis. In addition, the principle of the analysis in multimodal TRS gives rise to the signal of the pure population term. In general, the oscillatory and non-oscillatory signals are mixed in the species obtained by the conventional analysis for TA data. In the multimodal TRS, the two terms are separated based on the response functions which are commonly observed in the two optical experiments.

Chapter 5

Summary and Outlook

5.1 Summary

5.1.1 Time-resolved Spectroscopies on the Femtosecond Timescale

The pump-probe and pump-DFWM experiments on biological polyenes and rhodamine 6G elucidated the ultrafast molecular dynamics on a fs timescale. The nonstationary states prepared by the initial pump interactions gave rise to the strong coherences containing the information of the nuclear rearrangement. The coherence observed in the optical experiments showed the vibronic interactions between the electronic states in the carotenoids. For example, the coupling between B_u states were observed for shorter chain polyenes ($N = 9$ and 10) in addition to the well-known $1A_g^- - 2A_g^-$ coupling (detail information appears in 5.1.2). Moreover, the coupling caused modifications of the early dynamics in the pump-probe experiment. Since such modifications are ignored in the conventional SVD analyses, we suggested a new approach to solve the two issues (rotation ambiguity and local minimum) in the conventional pump-probe experiment on the fs timescale.

The combination of the pump-probe and pump-DFWM experiments by functional analysis gave rise to a new principle to decompose the time-resolved spectra. Since the response functions of the two optical experiments share a part of signal generation pathways, it is possible to separate the signals based on the interactions of the initial-pump pulse. For example, the wavepacket dynamics and population dynamics were separated in the time-resolved spectra of rhodamine 6G (detail information appears in 5.1.3). In addition, the influences of the rotation ambiguity and local minimum in the conventional SVD analysis are now much weaker in the new approach due to the evaluations of the kinetic models in the two data sets measured by pump-probe and pump-DFWM experiments. In multimodal approach, the resultant components are explained by the response functions appearing in pump-probe and pump-DFWM experiments. This approach indicates the possibility of the separation of the optical signals based on the response functions by the combination of the optical experiments.

5.1.2 Vibronic Effects in the Polyenes with $N = 9, 10, 11$ and 13

The couplings in the photosynthetic polyenes were observed as an increase and a decrease of the vibrational frequencies of the C–C and C=C stretching modes. Two pairs of the electronic states, with the symmetries of $1B_u^+$ and $1B_u^-$ or $1A_g^-$ and $2A_g^-$ respectively, were strongly coupled as expected in the theory.^{18,24} The couplings have different dependences on the conjugation length and solvent polarization. Firstly, the coupling between the $1A_g^-$ and $2A_g^-$ states was observed for the carotenoids with $N = 9 - 13$. This coupling increased the vibrational frequency of the $2A_g^-$ C=C stretching mode which appeared at 1800 cm^{-1} . Secondly, the vibrational relaxation on a distinct anharmonic potential surface was observed as an increase of the vibrational frequencies during the relaxation. On the other hand, the vibronic coupling between the $1B_u^+$ and $1B_u^-$ states, which appeared during the early dynamics for the short polyenes with $N = 9$ and 10 , have strong dependences on the conjugation length and the solvent polarizability. Interestingly, controlling the energetic degeneration between the ionic and cationic states by solvent polarizability changed the coupling strength between $1B_u^+$ and $1B_u^-$ states for

lutein ($N = 9$, $\beta = 1$) as expected by the derivative coupling. Obviously, the couplings modified the appearance of the early dynamics on the pump-probe experiment. Thus, the solute-solvent interaction had a significant contribution on the lifetime and the population dynamics observed in the pump-probe experiment.

In addition, care was taken to follow a clear definition of Born-Huang, Born-Oppenheimer and crude adiabatic approximation, which will help to understand the physical meaning of vibronic interactions induced by derivative coupling. Since the meaning of the words are often obscure in literature³⁵, the definitions of the work would help the transparency of the research. Especially regarding the derivative coupling, the theoretical expectation explains our experimental observation very well.

5.1.3 Multimodal Approach for Ultrafast Molecular Dynamics

The analytical problems in an ultrafast pump-probe experiment were effectively solved by the multimodal TRS. We demonstrated an example of the multimodal approach by combining two multipulse optical techniques, pump-probe and pump-DFWM experiments, implemented under the same conditions. The functional analysis for the two data sets overcome the rotation ambiguity as well as the local minimum. The multimodal approach decomposed the signals into the components based on the patterns of the initial pump interactions commonly observed in the two optical experiments. This new principle of the decomposition led to a unique interpretation of the results.

The determination of the correct theoretical model only based on the pump-probe spectra of rhodamine 6G was not successful by global target fitting due to the rotation ambiguity and local minimum in the SVD analysis. Three different theoretical models, which are the two-state parallel, the two-state sequential or the three-state sequential+parallel model, generated error values which did not allow to identify the best solution. In addition, the three-state sequential+parallel model has a significant influence from the rotational ambiguity and local minimum. In multimodal TRS, the problem has been solved by the evaluation of the kinetic models combining the analysis of data from the two sets of measurements in one analytical routine. As a result, the coherence and population terms were separated for the time-resolved spectra of rhodamine 6G. This idea of the analysis could be widely applied for other optical experiments.

5.2 Outlook

5.2.1 Functions of Vibronic Coupling in Photosynthetic Polyenes

The vibronic couplings in the carotenoids indicated that the interactions between the chromophores and the solvent molecules changed the coupling strengths. Obviously, the influences of the surrounded environment of the pigment molecules have significant influences for the application of the molecules. In the case of photosynthetic polyenes, the carotenoids are covered by proteins and lipids in a pigment-protein complex. However, the effects of the unique environment on the early dynamics of the polyenes are still not revealed. As a result, the light-energy conversion efficiencies of solar cells using the same sets of the pigments are not as efficient as the natural ones. The unique features of the vibronic couplings could be a key process to reveal the mechanism of the high light-energy conversion efficiency of the photosynthetic apparatus.

For example, the mixture of the carotenoids and chlorophylls used in dye-sensitized solar cell showed unique features of intermolecular interactions. Especially, the enhancement of the efficiency by the alignment of the molecules has significant importance because the localized excitations of the molecules are necessary to prevent singlet-triplet annihilation reaction and to keep the number of the excited-state dye molecules as much as possible.¹²¹ The further detail mechanism is still unrevealed due to the difficulties to describe such intermolecular interactions in theory. However, some research indicates possible interpretation of such interactions.³⁹ Thus, the interaction between the carotenoids and other molecules can be the next step of the application of the pump-DFWM experiment.

On the other hand, regarding the characterization of vibronic coupling appearing on C–C and C=C stretching modes, their vibrational frequencies should be strictly determined by calculations and measurements. This requires a complete series of the polyenes having different lengths of conjugated double bonds (N) or different end-groups such as the β ring. In addition, the conformers of the polyenes could have a totally different coupling dynamics due to their structural symmetries. Since most of them don't belong to the C_{2h} point group, the conformers should have different features on the excited-state dynamics. In this work, we determined a part of them. A complete set of the data will be a great reference for future investigations.

5.2.2 Multimodal Approach

In this work the idea and an example of multimodal TRS were demonstrated. Since it is still a kind of SVD analysis, the technique requires further improvements especially for the three points as below.

Firstly, the maximum precision determined by the inner products of the components in kinetic models should be carefully evaluated to remove some kinetic models having a low maximum precision. In Chapter 4, the temporal and spectral overlaps between the components lead to the rotation ambiguity and local minimum. As a result, there are many results which give rise to the same value of the error functions. In other word, the strong overlap between the components in kinetic models, or a huge inner products, detracts the precision of the analysis for pump-probe data. Therefore, it would be necessary to remove some theoretical kinetic models which have low maximum precision. In this work, we removed three-state sequential+parallel model due to this reason, although the model gave rise to much smaller error values compared with the two-state models. However, it is better to create a certain criteria which can remove some kinetic models based on the evaluation of kinetic models.

Secondly, an accurate pulse characterization, especially about the chirp of the pulses, is desirable. In pump-DFWM experiment, the significant influences induced by the chirp and pulse durations are reported.⁹⁸ In addition, the accurate experimental determination of the analytical parameters related to the instrumental response function (IRF) can reduce the number of the calculations in multimodal TRS.

In addition, the concept of multimodal approach can be extended for other spectroscopies having some similarity in the response functions observed in the optical experiments. An example could be the determination of the correlation function $M(t)$. The correlation function describes the fluctuation of the transition-energy gap by the solute-solvent interaction. There is a good approximation to determine the correlation function $M(t)$ as a sum of the faster part $M_1(t)$ and the slower part $M_2(t)$.¹²² Since the $M_1(t)$ and $M_2(t)$ can be observed by the echo-peak shift, time-gated echo, absorption and emission spectra, it is possible to determine the correlation function by the numerical simulation of the experimental data.¹²³

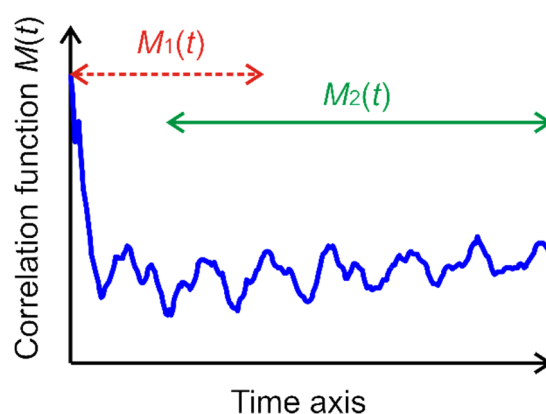


Figure 5.1: The correlation function $M(t)$ can be determined as a sum of the faster part $M_1(t)$ and the slower part $M_2(t)$ which can be observed in different optical experiments.

In conclusion, the multimodal approach is suitable to combine the optical experiments having the same part of the response functions and observables.

Appendix A

Symmetrical Operators and Symmetry of Molecular Orbitals

Operation around x, y, z axis are described by the transformation matrix between the original coordinate (x,y,z) and the new coordinate (x',y',z').

E: identity

$$\begin{bmatrix} 1 & 0 & 0 \\ 0 & 1 & 0 \\ 0 & 0 & 1 \end{bmatrix} \begin{bmatrix} x \\ y \\ z \end{bmatrix} = \begin{bmatrix} x' \\ y' \\ z' \end{bmatrix}$$

σ : reflection (σ_v : vertical, σ_h : horizontal, σ_d : dihedral, σ_{xy} : xy plane)

$$\begin{bmatrix} 1 & 0 & 0 \\ 0 & 1 & 0 \\ 0 & 0 & -1 \end{bmatrix} \begin{bmatrix} x \\ y \\ z \end{bmatrix} = \begin{bmatrix} x' \\ y' \\ z' \end{bmatrix}$$

C_n : rotation around an axis (for example, around z axis)

$$\begin{bmatrix} \cos(2\pi/n) & \sin(2\pi/n) & 0 \\ -\sin(2\pi/n) & \cos(2\pi/n) & 0 \\ 0 & 0 & 1 \end{bmatrix} \begin{bmatrix} x \\ y \\ z \end{bmatrix} = \begin{bmatrix} x' \\ y' \\ z' \end{bmatrix}$$

i: inversion

$$\begin{bmatrix} -1 & 0 & 0 \\ 0 & -1 & 0 \\ 0 & 0 & -1 \end{bmatrix} \begin{bmatrix} x \\ y \\ z \end{bmatrix} = \begin{bmatrix} x' \\ y' \\ z' \end{bmatrix}$$

The molecular orbitals of the molecules with C_{2h} point group are labeled according to the symmetry properties as belonging to one of the four irreducible representation (A_g , A_u , B_g , B_u) with different combination of operators.

Table A1: Character table for the C_{2h} point group. A value of 1 represents no change between original coordinate (x,y,z) and new coordinate (x',y',z') and -1 refers to the opposite change.

C_{2h}	E	C_2	i	σ_h
A_g	1	1	1	1
B_g	1	-1	1	-1
A_u	1	1	-1	-1
B_u	1	-1	-1	1

Appendix B

Theoretical Description of Pump-probe and Pump-DFWM Experiments

Optical spectroscopies read a set of physical quantities through light-matter interaction. Since physical quantities of molecules are stored in the Hamiltonian as the eigenvalues of the relevant eigenvectors, spectroscopic signals are originated from the Hamiltonian. In general, light-matter interaction is approximately described by optical polarizations⁴¹. In the description, the expectation value of the polarization is calculated by the density matrix (Appendix C) which is an alternative representation of the molecular wavefunctions. In addition, the polarization can be simplified by experimental condition, such as pulse degeneration, phase matching condition or energetic resonance. This Appendix shows theoretical descriptions for pump-probe (3rd-order nonlinearity) and pump-DFWM experiments (5th-order nonlinearity).

B.1 Light-matter Interaction

With nonlinear spectroscopies, one can obtain plenty of information from the molecular Hamiltonian through the light-matter interaction. The total Hamiltonian H_T of the system, including a time-dependent light-matter interaction, is given by

$$H_T = H + V(t) \quad . \quad (B1)$$

It is divided into a time-independent part H and a time-dependent interaction Hamiltonian $V(t)$, which represents the light-matter interaction.

In general, the theoretical description of the light-matter interaction contains many parameters representing the experimental conditions. In other words, the experimental conditions determine the appearance of the Hamiltonian. The feature of the light-matter interaction is described by the optical polarization $P(\mathbf{x}, t)$ which is a physical quantity. Furthermore, dielectric media have a very small magnetic permeability compared with their electronic susceptibility. Thus, the effects of an optical magnetic field are negligible so that a nonlinear medium interacting with electric fields can be considered by the dipole interaction. It is given by

$$V(\mathbf{x}, t) = - \int d\mathbf{x} E(\mathbf{x}, t) P(\mathbf{x}, t) \quad , \quad (B2)$$

where $E(\mathbf{x}, t)$ is the classical transverse electric field. The calculation of the integral in Eq. (B2) is difficult due to the complex spatial excitation profile created in the matter by the electric fields. Thus, it is simplified to the optical responses of a single particle whose size is much smaller than the wavelength where it is valid to use the dipole approximation. Hence, Eq. (B2) can be approximated to

$$V(t) = -\hat{\mu}E(\mathbf{x}, t) \quad , \quad (B3)$$

where $\hat{\mu}$ is the dipole operator of an absorber. The incoming electric fields induce a time-dependent polarization $P(\mathbf{x}, t)$, which is given by the expectation value (see Eq. (C4) in Appendix C)

$$P(\mathbf{x}, t) = \text{Tr}[\hat{\mu}\hat{\rho}(E(\mathbf{x}, \tau), t)] \quad . \quad (B4)$$

$\hat{\rho}(E(\mathbf{x}, \tau), t)$ is a time-dependent density operator of the system that depends on the external electric field $E(\mathbf{x}, \tau)$.

B.2 Perturbation Theory

The perturbation theory is an important idea to describe a weak interaction with a function. The idea is based on the fact that a weak interaction only gives rise to a small change of the function. In nonlinear spectroscopy, the polarization arising from the interactions with multiple electric fields can be calculated by perturbation theory. If we assume the fields only act to drive transitions between quantum states of the system and the interaction with the fields to be sufficiently weak, the problem can be treated with the perturbation theory. In Eq. (B4) the time-dependent density operator is a function of the electric field $E(\mathbf{x}, \tau)$ and can be expanded in powers of the electric field, *i.e.*,

$$\hat{\rho}(E) = \hat{\rho}^{(0)}(1) + \hat{\rho}^{(1)}(E) + \hat{\rho}^{(2)}(EE) + \hat{\rho}^{(3)}(EEE) + \dots \quad , \quad (\text{B5})$$

where $\hat{\rho}^{(n)}$ is the n^{th} -order expansion of the density matrix. For the polarization, the expansion yields

$$P(\mathbf{x}, t) = P^{(1)} + P^{(2)} + P^{(3)} + \dots = \varepsilon_0 [\chi^{(1)}E + \chi^{(2)}EE + \chi^{(3)}EEE + \dots] \quad . \quad (\text{B6})$$

$P^{(n)}$ refers to the polarization arising from n incident light fields. $P^{(2)}$ and higher terms referred to as the nonlinear terms. From Eq. (B5) and (B6) we calculate the polarization from the density matrix as the sum of the expectation values

$$P(\mathbf{x}, t) = \text{Tr}[\hat{\mu}(t), \hat{\rho}(E, \tau)] = \text{Tr}(\hat{\mu}, \hat{\rho}^{(0)}) + \text{Tr}(\hat{\mu}, \hat{\rho}^{(1)}) + \text{Tr}(\hat{\mu}, \hat{\rho}^{(2)}) + \dots \quad . \quad (\text{B7})$$

The dipole operator is given by (Heisenberg picture in Appendix C.2 Eq. (C21))

$$\hat{\mu}(t) = e^{iH_0 t} \mu e^{-iH_0 t} = U_0^\dagger(t) \mu U_0(t) \quad . \quad (\text{B8})$$

From Eq. (B7), n^{th} -order perturbation theory will be used to describe the nonlinear signal derived from interacting with n electric fields. The time evolution of the density matrix is given by the Liouville-Von Neumann equation (Eq. (C24) in Appendix C.3) as

$$\frac{\partial}{\partial t} \rho(t) = -\frac{i}{\hbar} [H, \rho(t)] \quad . \quad (\text{B9})$$

Time integration of the interaction Hamiltonian in Eq. (B9) gives

$$\rho(t) = \rho(0) - \frac{i}{\hbar} \int dt [V, \rho(t)] \quad . \quad (\text{B10})$$

Here, the time evolution of the dipole matrix contains the function itself. The expansion of Eq. (B10) in powers of the electric field gives

$$\rho(t) = \rho(0) + \sum_{n=1}^{\infty} \left(-\frac{i}{\hbar}\right)^n \int_{-\infty}^t dt_n \int_{-\infty}^{t_n} dt_{n-1} \dots \int_{-\infty}^{t_2} dt_1 [V_n(t_n), [V_{n-1}(t_{n-1}), [\dots, [V_1(t_1), \rho_{\text{eq}}]]]] \quad . \quad (\text{B11})$$

ρ_{eq} describes the equilibrium density matrix before the interaction with the light field. The n^{th} -order expansion of the density matrix is given by

$$\rho^{(0)} = \rho_{\text{eq}} \quad , \quad (\text{B12})$$

$$\rho^{(1)} = -\frac{i}{\hbar} \int_{-\infty}^t d\tau_1 [V_1(\tau_1), \rho_{\text{eq}}] \quad , \quad (\text{B13})$$

$$\rho^{(2)} = \left(-\frac{i}{\hbar}\right)^2 \int_{-\infty}^t d\tau_2 \int_{-\infty}^{\tau_2} d\tau_1 [V_2(\tau_2), [V_1(\tau_1), \rho_{\text{eq}}]] \quad , \quad (\text{B14})$$

$$\rho^{(n)} = \left(-\frac{i}{\hbar}\right)^n \int_{-\infty}^t d\tau_n \int_{-\infty}^{\tau_n} d\tau_{n-1} \dots \int_{-\infty}^{\tau_2} d\tau_1 [V_n(\tau_n), [V_{n-1}(\tau_{n-1}), [\dots, [V_1(\tau_1), \rho_{\text{eq}}]]]] \quad . \quad (\text{B15})$$

B.3 Polarization

The perturbation theory for the polarization and the density operator lead to the expansion of the polarization in powers of electric fields. As a result, the nonlinear responses are described by repeated linear interactions of electric fields as shown in Eq. (B12)-(B15). Each term of the polarization can be further simplified by changing the variables as shown below. From Eq. (B7) and (B15), the n^{th} -order polarization is given by

$$P^{(n)}(t) = \left(\frac{i}{\hbar}\right)^n \int_0^\infty dt_n \cdots \int_0^\infty dt_1 E(t-t_n) \cdots E(t-t_n - \cdots - t_1) \text{Tr} \left\{ \left[\left[\left[\hat{\rho}(t_n + \cdots + t_1), \hat{\mu}(t_{n-1} + \cdots + t_1) \right], \cdots \right], \cdots \hat{\mu}(0) \right], \rho_{\text{eq}} \right\} \quad (\text{B16})$$

In the equation, absolute times are substituted by time intervals to yield a more intuitive description shown in Figure B.1.

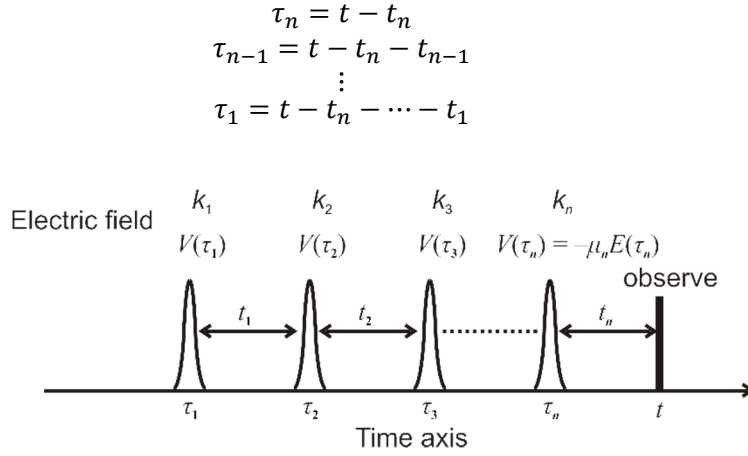


Figure B.1: Multi-pulse sequence for n^{th} -order polarization. The pulse sequence is described by the delay times τ_n and the time intervals t_n . The pulses are labeled by the vector k_n corresponding to the interaction $V(\tau_n)$ in the equations.

Within this time picture, the n^{th} -order polarization can be expressed using the identity $[A, [B, C]] = [[A, B], C]$ as

$$P^{(n)}(\mathbf{x}, t) = \int_0^\infty dt_n \int_0^\infty dt_{n-1} \cdots \int_0^\infty dt_1 R^{(n)}(t_n, t_{n-1}, \cdots, t_1) E^{(n)}(\mathbf{x}, t, t_n, t_{n-1}, \cdots, t_1) \quad (\text{B17-1})$$

where

$$\begin{aligned} R^{(n)}(t_n, t_{n-1}, \cdots, t_1) &= \left(\frac{i}{\hbar}\right)^n \theta(t_1) \theta(t_2) \cdots \theta(t_n) \text{Tr} \left\{ \left[\left[\left[\hat{\rho}(t_1 + t_2 + \cdots + t_n), \hat{\mu}(t_1 + t_2 + \cdots + t_{n-1}) \right], \hat{\mu}(t_1 + t_2) \right], \hat{\mu}(t_1) \right], \hat{\rho}(0) \right] \hat{\rho}(-\infty) \right\} \quad (\text{B17-2}) \end{aligned}$$

$$E^{(n)}(\mathbf{x}, t, t_n, t_{n-1}, \cdots, t_1) = E_1(\mathbf{x}, t - t_n - t_{n-1} - \cdots - t_1) \cdots E_{n-1}(\mathbf{x}, t - t_n - t_{n-1}) E_n(\mathbf{x}, t - t_n) \quad (\text{B17-3})$$

$\theta(t)$ is the Heaviside step function. Here, the light-matter interactions are expressed in term of a sequence of consecutive time intervals, $t_1 \cdots t_n$, prior to observing the system. For delta-function interactions the polarization and the response functions are directly proportional.

B.4 3rd-order Response Functions in Pump-probe Experiment

The response function used in n^{th} -order polarization has significant convenience to estimate observable signals under some experimental condition. Thus, response function often becomes an evidence of the connection between experimental condition and interpretation of the signals. Appendix B.4 introduces observable signals in pump-probe experiment.

The Eq. (B17) for 3rd-order polarization can be transformed as (all intermediate equations are shown in Appendix D)

$$P^{(3)}(\mathbf{x}, t) = \int_0^\infty dt_3 \int_0^\infty dt_2 \int_0^\infty dt_1 R^{(3)}(t_3, t_2, t_1) E^{(3)}(\mathbf{x}, t, t_3, t_2, t_1) \quad , \quad (\text{B18-1})$$

where

$$R^{(3)}(t_3, t_2, t_1) = \left(\frac{i}{\hbar}\right)^3 \theta(t_1)\theta(t_2)\theta(t_3) \sum_{n=1}^4 [R_n^{(3)} - R_n^{(3)*}] \quad , \quad (\text{B18-2})$$

$$E^3(\mathbf{x}, t, t_3, t_2, t_1) = E(\mathbf{x}, t - t_3)E(\mathbf{x}, t - t_3 - t_2)E(\mathbf{x}, t - t_3 - t_2 - t_1) \quad , \quad (\text{B18-3})$$

$$\begin{aligned} R_1^{(3)}(t_1, t_2, t_3) &= \text{Tr}[\mu U_0(t_3)\mu U_0(t_2)\mu U_0(t_1)\mu \hat{\rho} U_0^\dagger(t_1)U_0^\dagger(t_2)U_0^\dagger(t_3)] \\ R_2^{(3)}(t_1, t_2, t_3) &= \text{Tr}[\mu U_0(t_3)U_0(t_2)U_0(t_1)\mu \hat{\rho} U_0^\dagger(t_1)\mu U_0^\dagger(t_2)\mu U_0^\dagger(t_3)] \\ R_3^{(3)}(t_1, t_2, t_3) &= \text{Tr}[\mu U_0(t_3)U_0(t_2)\mu U_0(t_1)\hat{\rho}\mu U_0^\dagger(t_1)U_0^\dagger(t_2)\mu U_0^\dagger(t_3)] \\ R_4^{(3)}(t_1, t_2, t_3) &= \text{Tr}[\mu U_0(t_3)\mu U_0(t_2)U_0(t_1)\hat{\rho}\mu U_0^\dagger(t_1)\mu U_0^\dagger(t_2)U_0^\dagger(t_3)] \end{aligned} \quad . \quad (\text{B18-4})$$

In the Eq. (B18-1) and (B18-2), the 3rd-order polarization is expressed as a linear combination of four response functions $R_1^{(3)} \sim R_4^{(3)}$ and their complex conjugates. In Eq. (B18-4), each response function contains a different sequence of the dipole interactions. For example, the density matrix, $\hat{\rho}$, in $R_1^{(3)}$ has the sequence: ket interaction (k_1) \rightarrow time evolution t_1 \rightarrow ket interaction (k_2) \rightarrow time evolution t_2 \rightarrow ket interaction (k_3) \rightarrow time evolution t_3 \rightarrow the signal. Such dipole interaction and time evolution are usually summarized by the double-sided Feynman diagram as shown in Figure B.2.

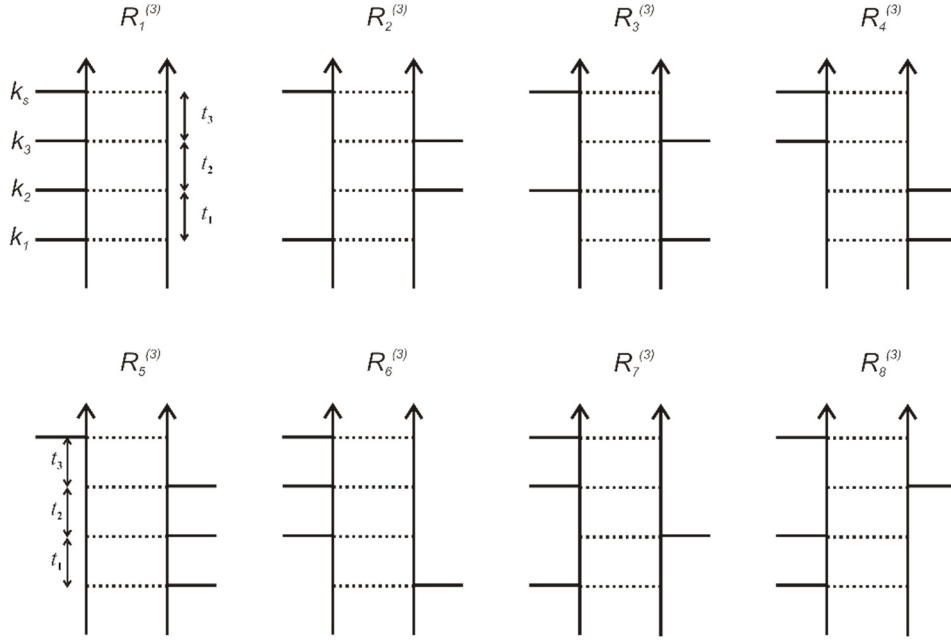


Figure B.2: Double-sided Feynman diagram for 3rd-order nonlinear response functions shown in Eq. (B18-4). The center columns are density matrix with the time evolution from the bottom to the top. The electric fields are shown as the vectors interacting with the density matrix from left-hand side (the ket side) and right-hand side (the bra side) at each delay time.

The observable signals in pump-probe experiment can be estimate by use of the double-sided Feynman diagram in Figure B.2 and experimental condition. In pump-probe experiment, k_1 and k_2 are identical ($k_{IP} = k_1 = k_2$) and the signal is observed at $k_s = k_1 - k_2 + k_3$ ($k_s = -k_1 + k_2 + k_3$). The information determines the direction of dipole interactions and observable signals as shown in Figure B.3.

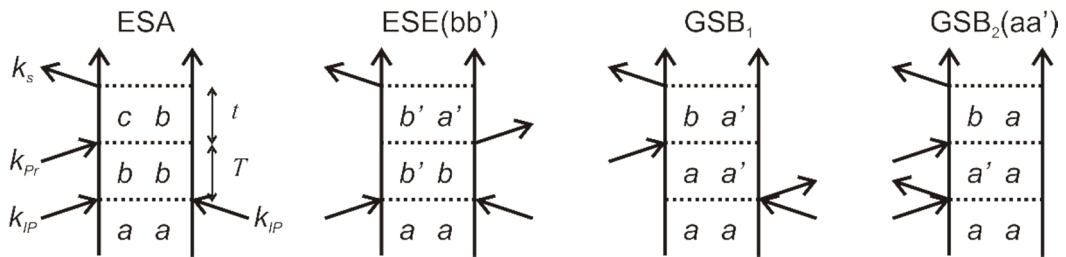


Figure B.3: Double-sided Feynman diagram for the observable signals in pump-probe experiment. ESA = excited-state absorption, ESE = excited-state emission and GSB = ground-state bleaching. The incoming arrows to the density matrix are equivalent with the creation operators while the outgoing arrows stand for the annihilation operators.

The observable phenomena in pump-probe experiment have four sequences; the excited-state absorption (ESA) from $R_6^{(3)}$ and $R_7^{(3)}$, excited-state emission (ESE) from $R_2^{(3)}$ and $R_3^{(3)}$ and ground-

state bleaching (GSB₁ from $R_4^{(3)}$ and GSB₂ from $R_1^{(3)}$), respectively. In addition, there are the signals arising from the wavepacket motion with the frequencies of $\omega_{aa'}$ in GSB and $\omega_{bb'}$ in ESE.

B.5 5th-order Response Functions in Pump-DFWM Experiment

As seen in previous section, the double-sided Feynman diagrams for response functions contain crucial information to estimate observable signals. In addition, the number of the response functions can be reduced by taking account of the experimental condition. This section introduces the observable signals in pump-DFWM experiment from the 5th-order nonlinear response functions.

The 5th-order nonlinear response functions have 16 terms with their complex conjugates. In pump-DFWM experiment, k_1 and k_2 are identical ($k_{IP} = k_1 = k_2$), $k_3 (= k_{pu})$ and $k_4 (= k_{st})$ interact at the same delay time and the signal is observed at $k_s = k_1 - k_2 + k_3 - k_4 + k_5$. Then, the number of the terms are reduced till the nine functions with their complex conjugates as shown in Eq. (B19) (detail information and intermediate equations are shown in Appendix D).

$$\begin{aligned}
R_1^{(5')} &= \text{Tr}[\mu U_0(t_5) \mu U_0(t_4) \mu U_0(t_2) \mu \hat{\rho} U_0^\dagger(t_2) U_0^\dagger(t_4) U_0^\dagger(t_5)] \\
R_2^{(5')} &= \text{Tr}[\mu U_0(t_5) U_0(t_4) \mu U_0(t_2) \mu \hat{\rho} U_0^\dagger(t_2) \mu U_0^\dagger(t_4) \mu U_0^\dagger(t_5)] \\
R_3^{(5')} &= \text{Tr}[\mu U_0(t_5) \mu U_0(t_4) U_0(t_2) \mu \hat{\rho} U_0^\dagger(t_2) \mu U_0^\dagger(t_4) U_0^\dagger(t_5)] \\
R_4^{(5')} &= \text{Tr}[\mu U_0(t_5) \mu U_0(t_4) \mu U_0(t_2) \mu \hat{\rho} U_0^\dagger(t_2) \mu U_0^\dagger(t_4) U_0^\dagger(t_5)] \\
R_5^{(5')} &= \text{Tr}[\mu U_0(t_5) U_0(t_4) \mu U_0(t_2) \mu \hat{\rho} U_0^\dagger(t_2) U_0^\dagger(t_4) \mu U_0^\dagger(t_5)] \\
R_6^{(5')} &= \text{Tr}[\mu U_0(t_5) U_0(t_4) U_0(t_2) \mu \hat{\rho} U_0^\dagger(t_2) \mu U_0^\dagger(t_4) \mu U_0^\dagger(t_5)] \\
R_7^{(5')} &= \text{Tr}[\mu U_0(t_5) \mu U_0(t_4) \mu U_0(t_2) \hat{\rho} \mu U_0^\dagger(t_2) U_0^\dagger(t_4) U_0^\dagger(t_5)] \\
R_8^{(5')} &= \text{Tr}[\mu U_0(t_5) U_0(t_4) \mu U_0(t_2) \hat{\rho} \mu U_0^\dagger(t_2) \mu U_0^\dagger(t_4) \mu U_0^\dagger(t_5)] \\
R_9^{(5')} &= \text{Tr}[\mu U_0(t_5) \mu U_0(t_4) U_0(t_2) \hat{\rho} \mu U_0^\dagger(t_2) \mu U_0^\dagger(t_4) U_0^\dagger(t_5)]
\end{aligned} \tag{B19}$$

The colors indicate a pair of dipole interactions from the ket side (red), both sides (green) or the bra side (blue) at each delay time. The response functions corresponding to the Eq. (B19) are represented by the double-sided Feynman diagrams as shown in Figure B.4.

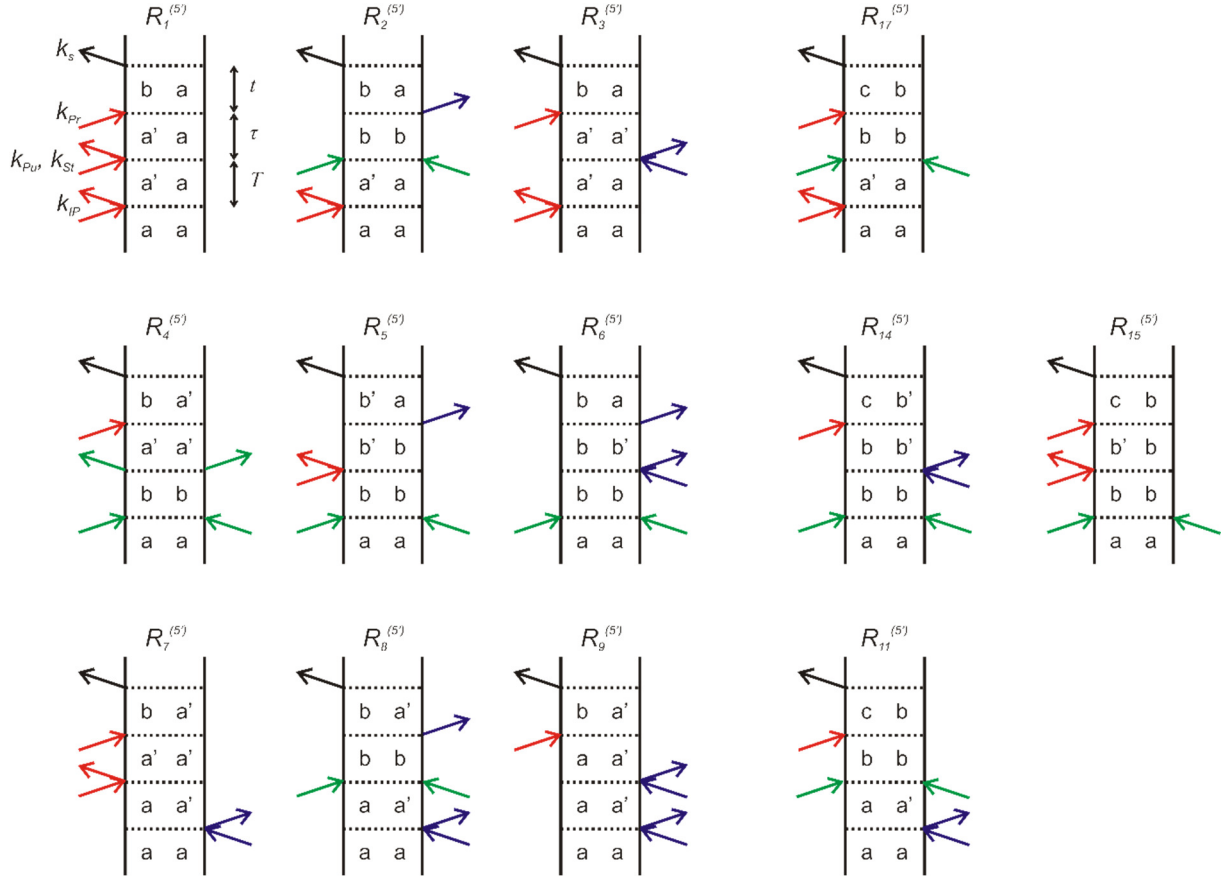


Figure B.4: Double-sided Feynman diagrams for 5th-order nonlinear response functions in pump-DFWM experiment given by Eq. (B19). The color codes of Eq. (B19) indicates the dipole interactions of a pair of electric fields (k_1-k_2 and k_3-k_4) from the ket side (red), both sides (green) or the bra side (blue) at each delay time. The interaction from both sides (green) can flip the directions for both vectors due to degeneracy of the pulses.

In addition, the spectral resonance in the experimental condition for carotenoids gives additional restriction in the appearance of the response functions. The three pulses (k_3 , k_4 and k_5 for pump, Stocks and probe pulses) are not resonant with the ($a \rightarrow b$) transition. Thus, $R_2^{(5)}$, $R_3^{(5)}$, $R_7^{(5)}$, $R_8^{(5)}$, $R_9^{(5)}$, $R_{11}^{(5)}$ and $R_{17}^{(5)}$ are obviously not observable in the research. However, a pair of interactions of the initial pump in $R_1^{(5)}$ can create resonant condition for the following four-wave mixing sequence. The rest of the response functions are resonant in the experimental condition.

As seen in the appendix, the appearance of the response functions are regulated by experimental condition. The fact indicates the importance of the design of multi-pulse optical experiments.

Appendix C

Density Matrix and Time Evolution Operator

C.1 Density Matrix

The density matrix (density operator) approach is often used to represent the eigenstates of a quantum system. Although describing a quantum system with the density matrix is equivalent to using the wavefunction, one can gain significant practical advantages for certain time-dependent problems, especially in nonlinear spectroscopy. The density matrix is defined as the outer product of the wavefunctions with its conjugate

$$\hat{\rho}(t) = \sum_i p_i |\Psi_i(t)\rangle \langle \Psi_i(t)| \quad . \quad (C1)$$

This implies that if you specify a state $|\Psi_n\rangle$, $\langle \Psi_n | \hat{\rho} | \Psi_n \rangle$ gives the probability of finding a particle in the state $|\Psi_n\rangle$. The density matrix is named after the observation that it plays the quantum role of a probability density. Due to this feature, the density matrix is useful to describe expectation values or observables of the operators. The wavefunction for the system is expanded as

$$|\Psi_i(t)\rangle = \sum_i c_i(t) |i\rangle \quad , \quad (C2)$$

and the elements of the density matrix are given by

$$\hat{\rho}(t) = \sum_{i,j} c_i(t) c_j^*(t) |i\rangle \langle j| = \sum_{i,j} \rho_{ij}(t) |i\rangle \langle j| \quad . \quad (C3)$$

Then the expectation value of an operator \hat{A} is expressed as

$$\langle \hat{A}(t) \rangle = \sum_{i,j} \langle \Psi_j(t) | \hat{A} | \Psi_i(t) \rangle = \sum_{i,j} c_i(t) c_j^*(t) \langle j | \hat{A} | i \rangle = \sum_{i,j} p_{ij} A_{ji} = \text{Tr}[\hat{A} \hat{\rho}(t)] \quad . \quad (C4)$$

Here we use the identity of trace elements

$$\text{tr} \mathbf{AB}^T = \sum_{i=1}^n \sum_{j=1}^n a_{ij} b_{ij} \quad . \quad (C5)$$

The density matrix elements can be categorized into diagonal and off-diagonal elements based on their features. The diagonal elements ($i = j$) give the probability of occupying a quantum state:

$$\rho_{ii} = c_i c_i^* = p_i \geq 0 \quad . \quad (C6)$$

For this reason, the diagonal elements are referred to as populations. On the other hand, the off-diagonal elements ($i \neq j$) are complex and have a time-dependent phase factor which is given by

$$\rho_{ij} = c_i(t) c_j^*(t) = c_i c_j^* e^{-i\omega_{ij}t} \quad . \quad (C7)$$

C.2 Time-evolution Operator

The time evolution of the state of a quantum system is described by the time-dependent Schrödinger equation

$$i\hbar \frac{\partial}{\partial t} \Psi(\mathbf{x}, t) = \hat{H}(\mathbf{x}, t) \Psi(\mathbf{x}, t) \quad , \quad (\text{C8})$$

$$\frac{\partial}{\partial t} \Psi(\mathbf{x}, t) + \frac{i\hat{H}}{\hbar} \Psi(\mathbf{x}, t) = 0 \quad , \quad (\text{C9})$$

$$\exp\left(\frac{i\hat{H}t}{\hbar}\right) \frac{\partial}{\partial t} \Psi(\mathbf{x}, t) + \exp\left(\frac{i\hat{H}t}{\hbar}\right) \frac{i\hat{H}}{\hbar} \Psi(\mathbf{x}, t) = 0 \quad , \quad (\text{C10})$$

$$\exp\left(\frac{i\hat{H}t}{\hbar}\right) \frac{\partial}{\partial t} \Psi(\mathbf{x}, t) + \frac{i\hat{H}}{\hbar} \exp\left(\frac{i\hat{H}}{\hbar} t\right) \Psi(\mathbf{x}, t) = 0 \quad , \quad (\text{C11})$$

$$\exp\left(\frac{i\hat{H}t}{\hbar}\right) \frac{\partial}{\partial t} \Psi(\mathbf{x}, t) + \frac{\partial}{\partial t} \exp\left(\frac{i\hat{H}}{\hbar} t\right) \Psi(\mathbf{x}, t) = 0 \quad , \quad (\text{C12})$$

$$\frac{\partial}{\partial t} \left[\exp\left(\frac{i\hat{H}t}{\hbar}\right) \Psi(\mathbf{x}, t) \right] = 0 \quad . \quad (\text{C13})$$

Integrating $t_0 \rightarrow t$, we get

$$\exp\left(\frac{i\hat{H}t}{\hbar}\right) \Psi(\mathbf{x}, t) - \exp\left(\frac{i\hat{H}t_0}{\hbar}\right) \Psi(\mathbf{x}, t_0) = 0 \quad , \quad (\text{C14})$$

$$\Psi(\mathbf{x}, t) = \hat{U}(t, t_0) \Psi(\mathbf{x}, t_0) \quad . \quad (\text{C15})$$

where the time evolution operator $\hat{U}(t, t_0)$ is given by

$$\hat{U}(t, t_0) = \exp\left(\frac{-i\hat{H}(t - t_0)}{\hbar}\right) \quad . \quad (\text{C16})$$

In the Schrödinger picture, the time evolution of an expectation value is given by the interaction of the time evolution operator with the density matrix. Therefore, the density matrix is expressed as

$$\hat{\rho}(t) = \hat{U}(t, t_0) |\Psi(t_0)\rangle \langle \Psi(t_0)| \hat{U}^\dagger(t, t_0) = \hat{U} \hat{\rho}(t_0) \hat{U}^\dagger \quad . \quad (\text{C17})$$

The time evolution of the expectation value, in the **Schrödinger picture**, is given by

$$\langle \hat{A}(t) \rangle = \text{Tr}[\hat{A} \hat{\rho}(t)] = \text{Tr}[\hat{A} \hat{U}(t) \hat{\rho}(0) \hat{U}^\dagger(t)] \quad . \quad (\text{C18})$$

On the other hand, it is possible to describe the same phenomenon in a different way. In the Heisenberg picture, the time evolution operator interacts with an operator \hat{A} ,

$$\begin{aligned} \langle \hat{A} \rangle \Psi(t) &= \langle \Psi(t) | \hat{A} | \Psi(t) \rangle = \langle \Psi(t_0) | \hat{U}^\dagger(t, t_0) \hat{A} \hat{U}(t, t_0) | \Psi(t_0) \rangle \\ &= \langle \Psi(t_0) | \hat{A}(t) | \Psi(t_0) \rangle \end{aligned} \quad . \quad (\text{C19})$$

where

$$\hat{A}(t) = \hat{U}^\dagger(t, t_0) \hat{A} \hat{U}(t, t_0) \quad , \quad (\text{C20})$$

Then, in the **Heisenberg picture**, the expectation value is given by

$$\langle \hat{A}(t) \rangle = \text{Tr}[\hat{A}(t)\hat{\rho}] = \text{Tr}[\hat{U}^\dagger(t)\hat{A}\hat{U}(t)\hat{\rho}] \quad . \quad (\text{C21})$$

By comparing the Schrödinger [Eq. (C18)] and Heisenberg picture [Eq. (C21)], the following relationship is obtained:

$$\langle \hat{A}(t) \rangle = \text{Tr}[\hat{A}\hat{U}(t)\hat{\rho}(0)\hat{U}^\dagger(t)] = \text{Tr}[\hat{U}^\dagger(t)\hat{A}\hat{U}(t)\hat{\rho}] \quad . \quad (\text{C22})$$

C.3 Time Evolution of Density Matrix

The equation of motion for the density matrix follows naturally from the definition of ρ and the time-dependent Schrödinger equation.

$$\begin{aligned} \frac{\partial \rho}{\partial t} &= \frac{\partial}{\partial t} [|\Psi\rangle\langle\Psi|] = \left[\frac{\partial}{\partial t} |\Psi\rangle \right] \langle\Psi| + \frac{\partial}{\partial t} |\Psi\rangle \frac{\partial}{\partial t} \langle\Psi| \\ &= -\frac{i}{\hbar} H_T |\Psi\rangle\langle\Psi| + \frac{i}{\hbar} |\Psi\rangle\langle\Psi| H_T = -\frac{i}{\hbar} [H_T, \rho] \quad . \quad (\text{C23}) \end{aligned}$$

$$i\hbar \frac{\partial \rho}{\partial t} = [H, \rho] \quad . \quad (\text{C24})$$

Eq. (C24) is called Liouville-Von Neumann equation for the density matrix.

Appendix D

Intermediate Equations for the Response Functions

The n^{th} -order polarization is given by (Eq. (B17) in Appendix B)

$$P^{(n)}(\mathbf{x}, t) = \int_0^\infty dt_n \int_0^\infty dt_{n-1} \cdots \int_0^\infty dt_1 R^{(n)}(t_n, t_{n-1}, \dots, t_1) E^{(n)}(\mathbf{x}, t, t_n, t_{n-1}, \dots, t_1) \quad , \quad (\text{B17-1})$$

where

$$R^{(n)}(t_n, t_{n-1}, \dots, t_1) = \left(\frac{i}{\hbar}\right)^n \theta(t_1)\theta(t_2) \cdots \theta(t_n) \text{Tr} \left\{ \left[\left[\left[\hat{\mu}(t_1 + t_2 + \cdots + t_n), \hat{\mu}(t_1 + t_2 + \cdots + t_{n-1}) \right], \hat{\mu}(t_1 + t_2) \right], \hat{\mu}(t_1) \right], \hat{\rho}(-\infty) \right] \right\} \quad , \quad (\text{B17-2})$$

$$E^{(n)}(\mathbf{x}, t, t_n, t_{n-1}, \dots, t_1) = E_1(\mathbf{x}, t - t_n - t_{n-1} \cdots - t_1) \cdots E_{n-1}(\mathbf{x}, t - t_n - t_{n-1}) E_n(\mathbf{x}, t - t_n) \quad . \quad (\text{B17-3})$$

For simplification, we define the operators as

$$\begin{aligned} \mu_1 &= \hat{\mu}_I(0) = \mu \\ \mu_2 &= \hat{\mu}_I(t_1) = U_0^\dagger(t_1) \mu U_0(t_1) \\ \mu_3 &= \hat{\mu}_I(t_1 + t_2) = U_0^\dagger(t_1) U_0^\dagger(t_2) \mu U_0(t_2) U_0(t_1) \\ \mu_4 &= \hat{\mu}_I(t_1 + t_2 + t_3) = U_0^\dagger(t_1) U_0^\dagger(t_2) U_0^\dagger(t_3) \mu U_0(t_3) U_0(t_2) U_0(t_1) \end{aligned} \quad . \quad (\text{D1})$$

Then, the third order response function is given by

$$R^{(3)}(t_3, t_2, t_1) = \left(\frac{i}{\hbar}\right)^3 \theta(t_1)\theta(t_2)\theta(t_3) \text{Tr} \left\{ \left[\left[\left[\mu_4, \mu_3 \right], \mu_2 \right], \mu_1 \right] \hat{\rho}(-\infty) \right\} \quad . \quad (\text{D2})$$

The trace elements are expressed as

$$\begin{aligned} \text{Tr} \left\{ \left[\left[\left[\mu_4, \mu_3 \right], \mu_2 \right], \mu_1 \right] \hat{\rho}(-\infty) \right\} &= \text{Tr} \left\{ \left[\left[(\mu_4 \mu_3 - \mu_3 \mu_4), \mu_2 \right], \mu_1 \right] \hat{\rho}(-\infty) \right\} \\ &= \text{Tr} \left\{ \left[(\mu_4 \mu_3 \mu_2 - \mu_3 \mu_4 \mu_2 - \mu_2 \mu_4 \mu_3 + \mu_2 \mu_3 \mu_4), \mu_1 \right] \hat{\rho}(-\infty) \right\} \\ &= \text{Tr} \left\{ \left[(\mu_4 \mu_3 \mu_2 \mu_1 - \mu_3 \mu_4 \mu_2 \mu_1 - \mu_2 \mu_4 \mu_3 \mu_1 + \mu_2 \mu_3 \mu_4 \mu_1) \right. \right. \\ &\quad \left. \left. - (\mu_1 \mu_4 \mu_3 \mu_2 - \mu_1 \mu_3 \mu_4 \mu_2 - \mu_1 \mu_2 \mu_4 \mu_3 + \mu_1 \mu_2 \mu_3 \mu_4) \right] \hat{\rho}(-\infty) \right\} \quad . \quad (\text{D3}) \\ &= \sum_{n=1}^4 \left[R_n^{(3)} - R_n^{(3)*} \right] \end{aligned}$$

where

$$\begin{aligned} R_1(t_1, t_2, t_3) &= \text{Tr}(\mu_4 \mu_3 \mu_2 \mu_1 \hat{\rho}) = \text{Tr}[\mu U_0(t_3) \mu U_0(t_2) \mu U_0(t_1) \mu \hat{\rho} U_0^\dagger(t_1) U_0^\dagger(t_2) U_0^\dagger(t_3)] \\ R_2(t_1, t_2, t_3) &= \text{Tr}(\mu_2 \mu_3 \mu_4 \mu_1 \hat{\rho}) = \text{Tr}[\mu U_0(t_3) U_0(t_2) U_0(t_1) \mu \hat{\rho} U_0^\dagger(t_1) \mu U_0^\dagger(t_2) \mu U_0^\dagger(t_3)] \\ R_3(t_1, t_2, t_3) &= \text{Tr}(\mu_1 \mu_3 \mu_4 \mu_2 \hat{\rho}) = \text{Tr}[\mu U_0(t_3) U_0(t_2) \mu U_0(t_1) \hat{\rho} \mu U_0^\dagger(t_1) U_0^\dagger(t_2) \mu U_0^\dagger(t_3)] \\ R_4(t_1, t_2, t_3) &= \text{Tr}(\mu_1 \mu_2 \mu_4 \mu_3 \hat{\rho}) = \text{Tr}[\mu U_0(t_3) \mu U_0(t_2) U_0(t_1) \hat{\rho} \mu U_0^\dagger(t_1) \mu U_0^\dagger(t_2) U_0^\dagger(t_3)] \end{aligned} \quad . \quad (\text{D4})$$

For 5th-order nonlinear responses, the response functions are obtained in the same way. The 5th-order polarization is given by

$$P^{(5)}(\mathbf{x}, t) = \int_0^\infty dt_5 \int_0^\infty dt_4 \int_0^\infty dt_3 \int_0^\infty dt_2 \int_0^\infty dt_1 R^{(5)}(t_5, t_4, t_3, t_2, t_1) E^{(5)}(\mathbf{x}, t, t_5, t_4, t_3, t_2, t_1) \quad , \quad (\text{D5-1})$$

$$R^{(5)}(t_5, t_4, t_3, t_2, t_1) = \left(\frac{i}{\hbar}\right)^5 \theta(t_1)\theta(t_2)\theta(t_3)\theta(t_4)\theta(t_5) \sum_{n=1}^{16} [R_n^{(5)} - R_n^{(5)*}] \quad , \quad (\text{D5-2})$$

$$E^3(\mathbf{x}, t, t_3, t_2, t_1) = E(\mathbf{x}, t - t_3)E(\mathbf{x}, t - t_3 - t_2)E(\mathbf{x}, t - t_3 - t_2 - t_1) \quad , \quad (\text{D5-3})$$

$$\begin{aligned} R_1^{(5)} &= \text{Tr}[\mu U_0(t_5)\mu U_0(t_4)\mu U_0(t_3)\mu U_0(t_2)\mu U_0(t_1)\mu\hat{\rho}U_0^\dagger(t_1)U_0^\dagger(t_2)U_0^\dagger(t_3)U_0^\dagger(t_4)U_0^\dagger(t_5)] \\ R_2^{(5)} &= \text{Tr}[\mu U_0(t_5)U_0(t_4)\mu U_0(t_3)U_0(t_2)\mu U_0(t_1)\mu\hat{\rho}U_0^\dagger(t_1)U_0^\dagger(t_2)\mu U_0^\dagger(t_3)U_0^\dagger(t_4)\mu U_0^\dagger(t_5)] \\ R_3^{(5)} &= \text{Tr}[\mu U_0(t_5)\mu U_0(t_4)U_0(t_3)U_0(t_2)\mu U_0(t_1)\mu\hat{\rho}U_0^\dagger(t_1)U_0^\dagger(t_2)\mu U_0^\dagger(t_3)\mu U_0^\dagger(t_4)U_0^\dagger(t_5)] \\ R_4^{(5)} &= \text{Tr}[\mu U_0(t_5)U_0(t_4)U_0(t_3)\mu U_0(t_2)\mu U_0(t_1)\mu\hat{\rho}U_0^\dagger(t_1)U_0^\dagger(t_2)U_0^\dagger(t_3)\mu U_0^\dagger(t_4)\mu U_0^\dagger(t_5)] \\ R_5^{(5)} &= \text{Tr}[\mu U_0(t_5)\mu U_0(t_4)\mu U_0(t_3)U_0(t_2)\mu U_0(t_1)\hat{\rho}\mu U_0^\dagger(t_1)U_0^\dagger(t_2)\mu U_0^\dagger(t_3)U_0^\dagger(t_4)U_0^\dagger(t_5)] \\ R_6^{(5)} &= \text{Tr}[\mu U_0(t_5)U_0(t_4)\mu U_0(t_3)\mu U_0(t_2)\mu U_0(t_1)\hat{\rho}\mu U_0^\dagger(t_1)U_0^\dagger(t_2)U_0^\dagger(t_3)U_0^\dagger(t_4)\mu U_0^\dagger(t_5)] \\ R_7^{(5)} &= \text{Tr}[\mu U_0(t_5)\mu U_0(t_4)U_0(t_3)\mu U_0(t_2)\mu U_0(t_1)\hat{\rho}\mu U_0^\dagger(t_1)U_0^\dagger(t_2)U_0^\dagger(t_3)\mu U_0^\dagger(t_4)U_0^\dagger(t_5)] \\ R_8^{(5)} &= \text{Tr}[\mu U_0(t_5)U_0(t_4)U_0(t_3)U_0(t_2)\mu U_0(t_1)\hat{\rho}\mu U_0^\dagger(t_1)U_0^\dagger(t_2)\mu U_0^\dagger(t_3)\mu U_0^\dagger(t_4)\mu U_0^\dagger(t_5)] \\ R_9^{(5)} &= \text{Tr}[\mu U_0(t_5)\mu U_0(t_4)\mu U_0(t_3)\mu U_0(t_2)U_0(t_1)\hat{\rho}\mu U_0^\dagger(t_1)\mu U_0^\dagger(t_2)U_0^\dagger(t_3)U_0^\dagger(t_4)U_0^\dagger(t_5)] \\ R_{10}^{(5)} &= \text{Tr}[\mu U_0(t_5)U_0(t_4)\mu U_0(t_3)U_0(t_2)U_0(t_1)\hat{\rho}\mu U_0^\dagger(t_1)\mu U_0^\dagger(t_2)\mu U_0^\dagger(t_3)U_0^\dagger(t_4)\mu U_0^\dagger(t_5)] \\ R_{11}^{(5)} &= \text{Tr}[\mu U_0(t_5)\mu U_0(t_4)U_0(t_3)U_0(t_2)U_0(t_1)\hat{\rho}\mu U_0^\dagger(t_1)\mu U_0^\dagger(t_2)\mu U_0^\dagger(t_3)\mu U_0^\dagger(t_4)U_0^\dagger(t_5)] \\ R_{12}^{(5)} &= \text{Tr}[\mu U_0(t_5)U_0(t_4)U_0(t_3)\mu U_0(t_2)U_0(t_1)\hat{\rho}\mu U_0^\dagger(t_1)\mu U_0^\dagger(t_2)U_0^\dagger(t_3)\mu U_0^\dagger(t_4)\mu U_0^\dagger(t_5)] \\ R_{13}^{(5)} &= \text{Tr}[\mu U_0(t_5)\mu U_0(t_4)\mu U_0(t_3)U_0(t_2)U_0(t_1)\mu\hat{\rho}U_0^\dagger(t_1)\mu U_0^\dagger(t_2)\mu U_0^\dagger(t_3)U_0^\dagger(t_4)U_0^\dagger(t_5)] \\ R_{14}^{(5)} &= \text{Tr}[\mu U_0(t_5)U_0(t_4)\mu U_0(t_3)\mu U_0(t_2)U_0(t_1)\mu\hat{\rho}U_0^\dagger(t_1)\mu U_0^\dagger(t_2)U_0^\dagger(t_3)U_0^\dagger(t_4)\mu U_0^\dagger(t_5)] \\ R_{15}^{(5)} &= \text{Tr}[\mu U_0(t_5)\mu U_0(t_4)U_0(t_3)\mu U_0(t_2)U_0(t_1)\mu\hat{\rho}U_0^\dagger(t_1)\mu U_0^\dagger(t_2)U_0^\dagger(t_3)\mu U_0^\dagger(t_4)U_0^\dagger(t_5)] \\ R_{16}^{(5)} &= \text{Tr}[\mu U_0(t_5)U_0(t_4)U_0(t_3)U_0(t_2)U_0(t_1)\mu\hat{\rho}U_0^\dagger(t_1)\mu U_0^\dagger(t_2)\mu U_0^\dagger(t_3)\mu U_0^\dagger(t_4)\mu U_0^\dagger(t_5)] \end{aligned} \quad . \quad (\text{D5-4})$$

The 16 response functions can also be described in double-sided Feynman diagrams. However, the experimental conditions (k_1, k_2 pulses and k_3, k_4 pulses are temporally and energetically degenerate in pump-DFWM experiments) reduces the number of the functions. For pump-DFWM experiments, the set of response functions is

$$\begin{aligned} R_1^{(5)} &= \text{Tr}[\mu U_0(t_5)\mu U_0(t_4)\mu U_0(t_2)\mu\hat{\rho}\mu U_0^\dagger(t_2)U_0^\dagger(t_4)U_0^\dagger(t_5)] \\ R_2^{(5)} &= \text{Tr}[\mu U_0(t_5)U_0(t_4)\mu U_0(t_2)\mu\hat{\rho}\mu U_0^\dagger(t_2)\mu U_0^\dagger(t_4)\mu U_0^\dagger(t_5)] \\ R_3^{(5)} &= \text{Tr}[\mu U_0(t_5)\mu U_0(t_4)U_0(t_2)\mu\hat{\rho}\mu U_0^\dagger(t_2)\mu U_0^\dagger(t_4)U_0^\dagger(t_5)] \\ R_4^{(5)} &= \text{Tr}[\mu U_0(t_5)U_0(t_4)\mu U_0(t_2)\mu\hat{\rho}\mu U_0^\dagger(t_2)\mu U_0^\dagger(t_4)\mu U_0^\dagger(t_5)] \\ R_5^{(5)} &= \text{Tr}[\mu U_0(t_5)\mu U_0(t_4)\mu U_0(t_2)\mu\hat{\rho}\mu U_0^\dagger(t_2)\mu U_0^\dagger(t_4)U_0^\dagger(t_5)] \\ R_6^{(5)} &= \text{Tr}[\mu U_0(t_5)U_0(t_4)\mu U_0(t_2)\mu\hat{\rho}\mu U_0^\dagger(t_2)U_0^\dagger(t_4)\mu U_0^\dagger(t_5)] \\ R_7^{(5)} &= \text{Tr}[\mu U_0(t_5)\mu U_0(t_4)\mu U_0(t_2)\mu\hat{\rho}\mu U_0^\dagger(t_2)\mu U_0^\dagger(t_4)U_0^\dagger(t_5)] \\ R_8^{(5)} &= \text{Tr}[\mu U_0(t_5)U_0(t_4)U_0(t_2)\mu\hat{\rho}\mu U_0^\dagger(t_2)\mu U_0^\dagger(t_4)\mu U_0^\dagger(t_5)] \\ R_9^{(5)} &= \text{Tr}[\mu U_0(t_5)\mu U_0(t_4)\mu U_0(t_2)\hat{\rho}\mu U_0^\dagger(t_2)U_0^\dagger(t_4)U_0^\dagger(t_5)] \\ R_{10}^{(5)} &= \text{Tr}[\mu U_0(t_5)U_0(t_4)\mu U_0(t_2)\hat{\rho}\mu U_0^\dagger(t_2)\mu U_0^\dagger(t_4)\mu U_0^\dagger(t_5)] \\ R_{11}^{(5)} &= \text{Tr}[\mu U_0(t_5)\mu U_0(t_4)U_0(t_2)\hat{\rho}\mu U_0^\dagger(t_2)\mu U_0^\dagger(t_4)U_0^\dagger(t_5)] \\ R_{12}^{(5)} &= \text{Tr}[\mu U_0(t_5)U_0(t_4)\mu U_0(t_2)\hat{\rho}\mu U_0^\dagger(t_2)\mu U_0^\dagger(t_4)\mu U_0^\dagger(t_5)] \\ R_{13}^{(5)} &= \text{Tr}[\mu U_0(t_5)\mu U_0(t_4)\mu U_0(t_2)\mu\hat{\rho}\mu U_0^\dagger(t_2)\mu U_0^\dagger(t_4)U_0^\dagger(t_5)] \\ R_{14}^{(5)} &= \text{Tr}[\mu U_0(t_5)U_0(t_4)\mu U_0(t_2)\mu\hat{\rho}\mu U_0^\dagger(t_2)U_0^\dagger(t_4)\mu U_0^\dagger(t_5)] \\ R_{15}^{(5)} &= \text{Tr}[\mu U_0(t_5)\mu U_0(t_4)\mu U_0(t_2)\mu\hat{\rho}\mu U_0^\dagger(t_2)\mu U_0^\dagger(t_4)U_0^\dagger(t_5)] \\ R_{16}^{(5)} &= \text{Tr}[\mu U_0(t_5)U_0(t_4)U_0(t_2)\mu\hat{\rho}\mu U_0^\dagger(t_2)\mu U_0^\dagger(t_4)\mu U_0^\dagger(t_5)] \end{aligned} \quad , \quad (\text{D5-5})$$

where the colors indicate the dipole interactions from the ket side (red), both sides (green) or the bra side (blue) at each delay time. Since some of the functions are the same, they are renamed as,

$$\begin{aligned}
R_1^{(5')} &= \text{Tr}[\mu U_0(t_5) \mu U_0(t_4) \mu \mu U_0(t_2) \mu \mu \hat{\rho} U_0^\dagger(t_2) U_0^\dagger(t_4) U_0^\dagger(t_5)] \\
R_2^{(5')} &= \text{Tr}[\mu U_0(t_5) U_0(t_4) \mu U_0(t_2) \mu \mu \hat{\rho} U_0^\dagger(t_2) \mu U_0^\dagger(t_4) \mu U_0^\dagger(t_5)] \\
R_3^{(5')} &= \text{Tr}[\mu U_0(t_5) \mu U_0(t_4) U_0(t_2) \mu \mu \hat{\rho} U_0^\dagger(t_2) \mu \mu U_0^\dagger(t_4) U_0^\dagger(t_5)] \\
R_4^{(5')} &= \text{Tr}[\mu U_0(t_5) \mu U_0(t_4) \mu U_0(t_2) \mu \hat{\rho} \mu U_0^\dagger(t_2) \mu U_0^\dagger(t_4) U_0^\dagger(t_5)] \\
R_5^{(5')} &= \text{Tr}[\mu U_0(t_5) U_0(t_4) \mu \mu U_0(t_2) \mu \hat{\rho} \mu U_0^\dagger(t_2) U_0^\dagger(t_4) \mu U_0^\dagger(t_5)] \\
R_6^{(5')} &= \text{Tr}[\mu U_0(t_5) U_0(t_4) U_0(t_2) \mu \hat{\rho} \mu U_0^\dagger(t_2) \mu \mu U_0^\dagger(t_4) \mu U_0^\dagger(t_5)] \\
R_7^{(5')} &= \text{Tr}[\mu U_0(t_5) \mu U_0(t_4) \mu \mu U_0(t_2) \hat{\rho} \mu \mu U_0^\dagger(t_2) U_0^\dagger(t_4) U_0^\dagger(t_5)] \\
R_8^{(5')} &= \text{Tr}[\mu U_0(t_5) U_0(t_4) \mu U_0(t_2) \hat{\rho} \mu \mu U_0^\dagger(t_2) \mu U_0^\dagger(t_4) \mu U_0^\dagger(t_5)] \\
R_9^{(5')} &= \text{Tr}[\mu U_0(t_5) \mu U_0(t_4) U_0(t_2) \hat{\rho} \mu \mu U_0^\dagger(t_2) \mu \mu U_0^\dagger(t_4) U_0^\dagger(t_5)]
\end{aligned} \tag{D6}$$

where

$$\begin{aligned}
R_1^{(5')} &= R_1^{(5)} \\
R_2^{(5')} &= R_2^{(5)} = R_4^{(5)} \\
R_3^{(5')} &= R_3^{(5)} \\
R_4^{(5')} &= R_5^{(5)} = R_7^{(5)} = R_{13}^{(5)} = R_{15}^{(5)} \\
R_5^{(5')} &= R_6^{(5)} = R_{14}^{(5)} \\
R_6^{(5')} &= R_8^{(5)} = R_{16}^{(5)} \\
R_7^{(5')} &= R_9^{(5)} \\
R_8^{(5')} &= R_{10}^{(5)} = R_{12}^{(5)} \\
R_9^{(5')} &= R_{11}^{(5)}
\end{aligned}$$

Appendix E

Rate Equations

In our research we employ three types of basic kinetic models which are (1) sequential model, (2) branching model and (3) parallel model. Those models can be easily combined by using the following rate equations.

(1) Sequential Model

The four-state sequential model gives

$$\begin{array}{l}
 \begin{array}{c} k_1 \quad k_2 \quad k_3 \quad k_4 \\
 A \rightarrow B \rightarrow C \rightarrow D \rightarrow \end{array} , \\
 \frac{d}{dt}[A] = -k_1[A] , \\
 \frac{d}{dt}[B] = -k_2[B] + k_1[A] , \\
 \frac{d}{dt}[C] = -k_3[C] + k_2[B] , \\
 \frac{d}{dt}[D] = -k_4[D] + k_3[C] .
 \end{array}$$

By solving each differential equation, we obtain,

$$\begin{array}{l}
 [A] = [A]_0 e^{-k_1 t} , \\
 [B] = \frac{k_1}{k_2 - k_1} [A]_0 e^{-k_1 t} - \frac{k_1}{k_2 - k_1} [A]_0 e^{-k_2 t} = \frac{k_1}{k_2 - k_1} [A]_0 (e^{-k_1 t} - e^{-k_2 t}) , \\
 [C] = \frac{k_1 k_2}{(k_3 - k_2)(k_2 - k_1)(k_1 - k_3)} [A]_0 \{ (k_2 - k_3) e^{-k_1 t} + (k_3 - k_1) e^{-k_2 t} \\
 + (k_1 - k_2) e^{-k_3 t} \} , \\
 [D] = \frac{k_1 k_2 k_3}{(k_3 - k_2)(k_2 - k_1)(k_1 - k_3)} [A]_0 \left\{ \frac{k_2 - k_3}{k_4 - k_1} [e^{-k_1 t} - e^{-k_4 t}] \right. \\
 \left. + \frac{k_3 - k_1}{k_4 - k_2} [e^{-k_2 t} - e^{-k_4 t}] + \frac{k_1 - k_2}{k_4 - k_3} [e^{-k_3 t} - e^{-k_4 t}] \right\} .
 \end{array}$$

(2) Branching Model

The five-state branching model gives,

$$\begin{array}{l}
 \begin{array}{c}
 k_1 \quad k_2 \quad k_3 \\
 \rightarrow B \rightarrow C \rightarrow \\
 A
 \end{array} \\
 \begin{array}{c}
 k'_1 \quad k'_2 \quad k'_3 \\
 \rightarrow B' \rightarrow C' \rightarrow
 \end{array}
 \end{array}
 ,$$

$$\begin{array}{l}
 \frac{d}{dt}[A] = -(k_1 + k'_1)[A] \\
 \frac{d}{dt}[B] = -k_2[B] + k_1[A] \\
 \frac{d}{dt}[B'] = -k'_2[B'] + k'_1[A] \\
 \frac{d}{dt}[C] = -k_3[C] + k_2[B] \\
 \frac{d}{dt}[C'] = -k'_3[C'] + k'_2[B']
 \end{array}
 .$$

By solving each differential equation, we obtain,

$$\begin{array}{l}
 [A] = [A]_0 e^{-(k_1+k'_1)t} \\
 [B] = \frac{k_1}{k_2 - (k_1 + k'_1)} [A]_0 \{e^{-(k_1+k'_1)t} - e^{-k_2 t}\} \\
 [B'] = \frac{k'_1}{k'_2 - (k_1 + k'_1)} [A]_0 \{e^{-(k_1+k'_1)t} - e^{-k'_2 t}\} \\
 [C] = \frac{k_1 k_2}{(k_3 - k_2)[k_2 - (k_1 + k'_1)][(k_1 + k'_1) - k_3]} [A]_0 \{(k_2 - k_3)e^{-(k_1+k'_1)t} \\
 + [k_3 - (k_1 + k'_1)]e^{-k_2 t} + [(k_1 + k'_1) - k_2]e^{-k_3 t}\} \\
 [C'] = \frac{k'_1 k'_2}{(k'_3 - k'_2)[k'_2 - (k_1 + k'_1)][(k_1 + k'_1) - k'_3]} [A]_0 \{(k'_2 - k'_3)e^{-(k_1+k'_1)t} \\
 + [k'_3 - (k_1 + k'_1)]e^{-k'_2 t} + [(k_1 + k'_1) - k'_2]e^{-k'_3 t}\}
 \end{array}
 .$$

(3) Parallel Model

The six-state parallel model gives

$$\begin{array}{l}
 \begin{array}{c} k_1 \quad k_2 \quad k_3 \\ A \rightarrow B \rightarrow C \rightarrow \end{array} \\
 \begin{array}{c} k'_1 \quad k'_2 \quad k'_3 \\ A' \rightarrow B' \rightarrow C' \rightarrow \end{array} \\
 \frac{d}{dt}[A] = -k_1[A] \\
 \frac{d}{dt}[A'] = -k'_1[A'] \\
 \frac{d}{dt}[B] = -k_2[B] + k_1[A] \\
 \frac{d}{dt}[B'] = -k'_2[B'] + k'_1[A'] \\
 \frac{d}{dt}[C] = -k_3[C] + k_2[B] \\
 \frac{d}{dt}[C'] = -k'_3[C'] + k'_2[B']
 \end{array}$$

By solving each differential equation, we obtain,

$$\begin{array}{l}
 [A] = r[A]_0 e^{-k_1 t} \\
 [A'] = (1-r)[A]_0 e^{-k'_1 t} \\
 [B] = \frac{k_1}{k_2 - k_1} r[A]_0 (e^{-k_1 t} - e^{-k_2 t}) \\
 [B'] = \frac{k'_1}{k'_2 - k'_1} (1-r)[A]_0 (e^{-k'_1 t} - e^{-k'_2 t}) \\
 [C] = \frac{k_1 k_2}{(k_3 - k_2)(k_2 - k_1)(k_1 - k_3)} r[A]_0 \{ (k_2 - k_3)e^{-k_1 t} + (k_3 - k_1)e^{-k_2 t} \\
 \quad + (k_1 - k_2)e^{-k_3 t} \} \\
 [C'] = \frac{k'_1 k'_2}{(k'_3 - k'_2)(k'_2 - k'_1)(k'_1 - k'_3)} (1-r)[A]_0 \{ (k'_2 - k'_3)e^{-k'_1 t} \\
 \quad + (k'_3 - k'_1)e^{-k'_2 t} + (k'_1 - k'_2)e^{-k'_3 t} \}
 \end{array}$$

The kinetic model $\{p_i\}$ is given by convolution of the concentration curves with instrumental response function.

$$p_i(t) = [i] * \text{IRF}$$

Appendix F

Adiabatic Approximation

F.1 Separability of Molecular Hamiltonian

The ultrafast electron-nuclear motion, observed in femtosecond time-resolved spectroscopies, is theoretically described by molecular wavefunctions. Since it is impossible to calculate perfect wavefunctions for many-body systems, the separation of electronic and vibrational motions is often used as an approximation in the calculation. This idea is well-known as adiabatic approximation which is achieved in a few ways in literature.^{14,15} However, the slight differences of the methods have led to significant ambiguities on the usage of the word, and they are sometimes used in wrong way.^{35,124} As a result, the theoretical description of ultrafast electron-nuclear motion and their physical meanings are often hard to understand for experimental researcher. Here, the definitions of Born-Huang approximation^{15,16} and Born-Oppenheimer approximation¹⁴ are introduced to describe some optical phenomena appearing in the time-resolved experiment.

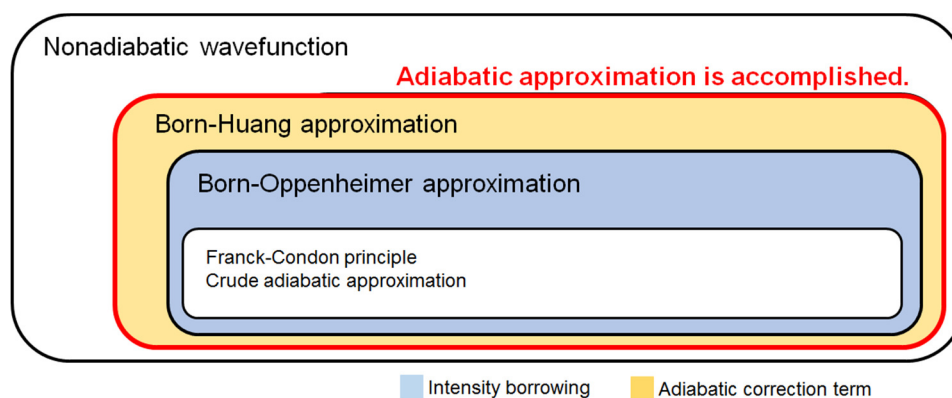


Figure F.1: The approximations often used to calculate molecular wavefunctions are depicted in the groups. The physical phenomena observed in optical experiments are equivalent with the differences between the approximations.

The idea of adiabatic approximation, which is the separability of electronic and vibrational motions, is realized by Born-Huang approximation. Figure F.1 shows the relationship between the approximations. Each method contains certain region in nonadiabatic wavefunctions to calculate approximated wavefunctions. While the idea of adiabatic approximation is already realized in Born-Huang approximation, the word of adiabatic approximation often means Born-Oppenheimer approximation due to chronological and practical reason. In the groups below Born-Huang approximation, the potential-energy surfaces consist of electronic states and vibrational states. Thus, each *vibronic* (*vibrational* + *electronic*) wavefunction in Born-Huang approximation can be described by a product of an electronic wavefunction and a vibrational wavefunction.

To understand the functions of natural pigments, it is important to prove the interactions between the electronic states. The most part of the interactions between the electronic states are equivalent with the derivative coupling which spreads beyond the Born-Huang approximation as shown in Figure 3.11. Interestingly, the effect induced by derivative coupling is expected to be stronger in degenerate energy levels around conical intersection which is often observed by ultrafast time-resolved spectroscopies. Thus, it is necessary to take account of the derivative coupling to reveal the nature of the potential-

energy surfaces observed in experiments. Since derivative coupling contains the elements out of the adiabatic approximation, the potential-energy surface in such case consists of vibronic levels having vibronic coupling between the energy levels.

In this appendix, the formulation of the approximations and the coupling are shown.

F.2 Born-Huang Approximation

In this section, it is shown that the idea of ‘‘adiabatic’’ is achieved by Born-Huang approximation. The general vibroelectronic Hamiltonian $\hat{H}(r, Q)$ for a molecular system can be written as the sum of the electronic part of the Hamiltonian \hat{H}_{el} and the nuclear kinetic energy operator \hat{T}_{nu} ,

$$\hat{H}(r, Q) = \hat{H}_{\text{el}}(r, Q) + \hat{T}_{\text{nu}}(Q) = \hat{H}_{\text{el}}(r, Q) + \frac{\hat{P}^2}{2m_\alpha} \quad , \quad (\text{F1})$$

where r and Q are the electronic and nuclear coordinates, \hat{P} is the nuclear momentum operator, m_α is the reduced mass of the nuclear coordinate Q_α (sum over all the nuclear coordinates α will be implicit throughout). The molecular wavefunctions Ψ can be expressed as sum of the products of the basis functions $\{\psi_n(r; Q)\}$, which are the electronic wavefunctions with fixed nuclear coordinate, and expansion coefficients (nuclear equation) $\chi_i(Q)$,

$$\Psi(r, Q) = \sum_i \psi_i(r; Q) \chi_i(Q) \quad . \quad (\text{F2})$$

Substituting this expression in the time-independent Schrödinger equation, we get

$$\hat{H}(r, Q) \sum_i \psi_i(r; Q) \chi_i(Q) = E \sum_i \psi_i(r; Q) \chi_i(Q) \quad , \quad (\text{F3})$$

$$\frac{1}{2m_\alpha} \sum_i [\psi_i(r; Q) \hat{P}^2 \chi_i(Q) + 2\hat{P}\psi_i(r; Q) \hat{P}\chi_i(Q) + \chi_i(Q) \hat{P}^2 \psi_i(r; Q)] \quad . \quad (\text{F4})$$

$$+ \sum_i \hat{H}_{\text{el}}(r, Q) \psi_i(r; Q) \chi_i(Q) = E \sum_i \psi_i(r; Q) \chi_i(Q)$$

Multiplying to the left by $\psi_j^*(r; Q)$ and integrating with respect to electronic coordinate r , we get

$$\begin{aligned} \hat{T}_{\text{nu}}\chi_j(Q) + V_{jj}\chi_j(Q) + \frac{1}{2m_\alpha} \sum_{i \neq j} [2\langle \psi_j | \hat{P} | \psi_i \rangle \hat{P}\chi_i(Q)] \\ + \frac{1}{2m_\alpha} \sum_i [\chi_i(Q) \langle \psi_j | \hat{P}^2 | \psi_i \rangle] = E\chi_j(Q) \end{aligned} \quad , \quad (\text{F5})$$

with

$$V_{ij} = \langle \psi_j | \hat{H}_{\text{el}} | \psi_i \rangle \quad , \quad (\text{F6})$$

$$\sum_i \langle \psi_j | \hat{P} | \psi_i \rangle = \begin{cases} = 0 & (i = j) \\ \neq 0 & (i \neq j) \end{cases} \quad . \quad (\text{F7})$$

The separation of the diagonal elements of Eq.(F5) on the left-hand side and the off-diagonal elements on the right-hand side leads to

$$\begin{aligned} & \left[\hat{T}_{\text{nu}} + V_{jj} + \frac{\langle \psi_j | \hat{P}^2 | \psi_j \rangle}{2m_\alpha} - E \right] \chi_j(Q) \\ & = -\frac{1}{2m_\alpha} \sum_{i \neq j} [2\langle \psi_j | \hat{P} | \psi_i \rangle \hat{P} + \langle \psi_j | \hat{P}^2 | \psi_i \rangle] \chi_i(Q) \end{aligned} \quad . \quad (\text{F8})$$

Concerning Eq.(F8), it is important to note that the suffix of i and j distinguish electronic states. In the sense of “adiabatic”, which gives rise to the separation of electronic motion and nuclear motion, a function of $\chi_j(Q)$ should be determined by a function of ψ_j . As long as there are some connection between an electronic wavefunction ψ_j and the other electronic wavefunctions ψ_i , it is impossible to achieve the separability of electronic and vibrational motions.

Thus, the Born-Huang approximation is given by neglecting all matrix elements connecting $\psi_j(r, Q)$ with other electronic states (the off-diagonal elements), the resulting nuclear equation takes the Schrödinger form,

$$\left[\hat{T}_{\text{nu}} + V_{jj} + \frac{\langle \psi_j | \hat{P}^2 | \psi_j \rangle}{2m_\alpha} \right] \chi_j(Q) = E \chi_j(Q) \quad . \quad (\text{F9})$$

Now, the idea of “adiabatic” is achieved, and an expansion coefficients $\chi_j(Q)$ is determined by an electronic wavefunction ψ_j . In other words, the Eq.(F2) in adiabatic approximation can be simply expressed as

$$\Psi(r, Q) = \psi_j(r; Q) \chi_j(Q) \quad . \quad (\text{F10})$$

It is important to note that there are many combinations of the eigenvalues and the wavefunctions which can satisfy the time-independent Schrödinger equation. By using suffix ν to distinguish each combination in Eq.(F10), we get

$$\Psi_j^\nu(r, Q) = \psi_j(r; Q) \chi_j^\nu(Q) \quad . \quad (\text{F11})$$

Now it is clear that the vibronic wavefunction $\Psi_j^\nu(r, Q)$ of the vibrational state ν belongs to the j -th electronic state is given by the product of the electronic wavefunction of the j -th electronic state and the wavefunction $\chi_j^\nu(Q)$ of the vibrational (nuclear motion) state ν on the j -th electronic state.

The Born-Huang adiabatic approximation is employed for accurate computations on small diatomic molecules for which very good electronic wavefunctions and energies are known.

F.3 Born-Oppenheimer Approximation

The Born-Oppenheimer approximation is widely used in chemistry and in physics. In this approximation, derivative coupling is often defined as

$$T'_{ij} = \langle \psi_j | \frac{\partial}{\partial Q} | \psi_i \rangle \quad (\text{derivative coupling}), \quad (\text{F12})$$

$$T''_{ij} = \langle \psi_j | \frac{\partial^2}{\partial Q^2} | \psi_i \rangle \quad . \quad (\text{F13})$$

By use of the definitions, the Eq.(F5) is expressed as

$$\hat{T}_{\text{nu}} \chi_j(Q) + V_{jj} \chi_j(Q) + \frac{-\hbar^2}{2m_\alpha} \sum_i \left[2T'_{ij} \frac{\partial}{\partial Q} + T''_{ij} \right] \chi_i(Q) = E \chi_j(Q) \quad . \quad (\text{F14})$$

For the comparison with Born-Huang approximation, the Eq. (F8) is expressed as

$$\left[\hat{T}_{\text{nu}} + V_{jj} - \frac{\hbar^2}{2m_\alpha} T''_{jj} - E \right] \chi_j(Q) = \frac{\hbar^2}{2m_\alpha} \sum_{i \neq j} \left[2T'_{ij} \frac{\partial}{\partial Q} + T''_{ij} \right] \chi_i(Q) \quad . \quad (\text{F15})$$

In Born-Oppenheimer approximation, the terms T' and T'' in Eq.(14) and Eq. (15) are totally neglected. Thus, the Born-Oppenheimer approximation is expressed as

$$[\hat{T}_{\text{nu}} + V_{jj}] \chi_j(Q) = E \chi_j(Q) \quad . \quad (\text{F16})$$

The Eq.(F16) can be interpreted as the Schrödinger equation for the wavefunction of nuclear motion in the potential energy $V_{jj}(Q)$. Each nuclear wavefunction is determined by one electronic wavefunction (adiabatic). Therefore, the Born-Oppenheimer wavefunctions are simply the product of an electronic wavefunction and a vibrational wavefunction.

Appendix G

Nonadiabtic Process

G.1 Derivative Coupling

The derivative coupling is a part of the interactions left out in order to make the molecular Hamiltonian separable in adiabatic approximation. Therefore, the effects induced by the term is known and described as “non-adiabatic”. The definition of the term is shown in Eq.(F12) in Appendix F.3. The derivative coupling between two quantum states has unique dependence on their energy difference. Since the Eq.(F12) obeys to the Hellman-Feynman-type formula¹⁰⁸ (Appendix H), we get

$$\langle \psi_j(r; Q) | \frac{\partial}{\partial Q} | \psi_i(r; Q) \rangle = \frac{\langle \psi_j(r; Q) | \frac{\partial \hat{H}_{el}(r; Q)}{\partial Q} | \psi_i(r; Q) \rangle}{V_{ii}(Q) - V_{jj}(Q)} \quad (G1)$$

Obviously, the derivative coupling tends to diverge for a small or vanishing energy. In other words, the adiabatic approximations breaks down, or electronic and vibrational motions are dynamically not separated, in the process occurring o the quantum states with small energy gap. Therefore, an alternative approach for the separability of electron and nuclear motions is required. This is achieved by use a set of diabatic basis¹²⁵, $\{\psi_i^{(D)}\}$, for which derivative couplings vanish,

$$\langle \psi_i^D(r; Q) | \frac{\partial}{\partial Q_\alpha} | \psi_j^D(r; Q) \rangle = 0 \quad (G2)$$

The diabatic basis can be obtained by the unitary transformation of the adiabatic Born-Oppenheimer basis¹⁸ although it is impossible to express a diabatic basis by use of a truncated set of adiabatic basis¹²⁶. Due to such difficulty, recent theoretical researches often employ the definition of quasidiabatic bases that are not strictly diabatic, but have derivative couplings that are as small as possible. In addition, the $\{\psi_i^D\}$ are no longer eigenfunctions of electronic Hamiltonian. Therefore, here, we discuss nonadiabatic process by use of vibronic states.

G.2 Vibronic Effects in Carotenoids

In literatures^{23,127}, the effects of vibronic interactions on the frequencies of coupled states has been considered by the basic formulas describing the frequency change and the Duschinsky effect¹²⁸ associated to vibronic coupling. Here, the idea is applied for the photosynthetic polyenes.

Now we consider two electronic states $|\phi_i\rangle$ and $|\phi_j\rangle$ with a totally symmetric mode with the coordinate Q for polyenes. If we assume these states are eigenstates of the electronic Hamiltonian \hat{H}_{el} and V_{ii} becomes minimum at the reference geometry of Q_0 ¹²⁹, they have diabaticity^{125,130} and belong to the class of diabatic states.

In the following we consider a case of one vibrational mode (Q), where the diabatic basis exists in a strict sense (curl condition). We take $W_{ij}(Q)$ as follows:

$$\mathbf{W}(Q) = \begin{bmatrix} W_{11}(Q) & W_{12}(Q) \\ W_{21}(Q) & W_{22}(Q) \end{bmatrix} = \begin{bmatrix} \frac{1}{2}\Omega^2 Q^2 & \gamma_{ij}Q \\ \gamma_{ji}Q & \frac{1}{2}\Omega^2 Q^2 + BQ + \Delta_{ji} \end{bmatrix} \quad . \quad (\text{G3})$$

where

$$W_{ij}(Q) = \langle \phi_j | \hat{H}_{\text{el}}(r, Q) | \phi_i \rangle \quad ,$$

Ω is the diabatic frequency taken to be the same in both states for simplicity, B denotes the displacement parameter between the two states and ΔE_{ji} is the vertical energy gap.

The transformation from the diabatic states $|\phi_i\rangle$ to the adiabatic states $|\psi_i\rangle$ is given by

$$\begin{aligned} \psi_1 &= \phi_1 \cos\left(\frac{\theta(Q)}{2}\right) + \phi_2 \sin\left(\frac{\theta(Q)}{2}\right) \\ \psi_2 &= -\phi_1 \sin\left(\frac{\theta(Q)}{2}\right) + \phi_2 \cos\left(\frac{\theta(Q)}{2}\right) \end{aligned} \quad . \quad (\text{G4})$$

Thus, we obtain

$$V_{12}(Q) = -\frac{1}{2}(W_{11}(Q) - W_{22}(Q)) \sin(\theta(Q)) - W_{12}(Q) \cos(\theta(Q)) \quad . \quad (\text{G5})$$

From the definition ($V_{12}(Q) = 0$) and assuming that $\Delta \gg BQ, \gamma_{12}Q$, we can approximate $\theta(Q)$ as

$$\begin{aligned} \tan(\theta(Q)) &= \frac{2W_{12}(Q)}{W_{11}(Q) - W_{22}(Q)} \quad , \\ \theta(Q) &= \arctan\left(\frac{2\gamma_{12}Q}{BQ + \Delta}\right) \quad , \\ \theta(Q) &= \arctan\left(\frac{2\gamma_{12}Q}{\Delta}\right) \quad . \quad (\text{G6}) \end{aligned}$$

In the approximation²³ by use of small displacement parameter B , the two roots of this Hamiltonian are expressed as

$$\varepsilon_{\pm} = \frac{1}{2}\Omega^2 Q^2 + \frac{1}{2}\Delta_{ji} \pm \sqrt{\frac{\Delta_{ji}^2}{4} + \gamma_{ij}^2 Q^2} \quad . \quad (\text{G7})$$

The coupling affects the frequencies in the adiabatic representations expressed as¹³¹

$$\omega_i = \Omega \sqrt{1 - \frac{2\gamma_{ij}^2}{\Delta_{ji}\Omega^2}} \approx \Omega \left(1 - \frac{\gamma_{ij}^2}{\Delta_{ji}\Omega^2}\right) \quad , \quad (\text{G8})$$

$$\omega_j = \Omega \sqrt{1 + \frac{2\gamma_{ij}^2}{\Delta_{ji}\Omega^2}} \approx \Omega_i \left(1 + \frac{\gamma_{ij}^2}{\Delta_{ji}\Omega^2}\right) \quad . \quad (\text{G9})$$

In conclusion, the vibronic coupling in the diabatic picture decreases the vibrational frequencies in the lower state and increases the frequencies of the higher state. It is easily generalized to the case in which the state S_0 is coupled by the totally symmetric mode to several electronic state S_1 .²⁴

Appendix H

Hellmann-Feynman Theorem for Electronic Hamiltonian

The commutation relation is expressed as

$$\begin{aligned} \left[\frac{\partial}{\partial Q}, \hat{H}_{\text{el}}(r; Q) \right] &= \frac{\partial}{\partial Q} \hat{H}_{\text{el}}(r; Q) - \hat{H}_{\text{el}}(r; Q) \frac{\partial}{\partial Q} \\ &= \frac{\partial \hat{H}_{\text{el}}(r; Q)}{\partial Q} + \hat{H}_{\text{el}}(r; Q) \frac{\partial}{\partial Q} - \hat{H}_{\text{el}}(r; Q) \frac{\partial}{\partial Q} = \frac{\partial \hat{H}_{\text{el}}(r; Q)}{\partial Q} \end{aligned} \quad . \quad (\text{H1})$$

Thus,

$$\frac{\partial}{\partial Q} \hat{H}_{\text{el}}(r; Q) - \hat{H}_{\text{el}}(r; Q) \frac{\partial}{\partial Q} = \frac{\partial \hat{H}_{\text{el}}(r; Q)}{\partial Q} \quad . \quad (\text{H2})$$

Multiplying to the left by $\psi_j(r; Q)$, to the right by $\psi_i(r; Q)$ and integrating with respect to electronic coordinate r , we get

$$\langle \psi_j | \frac{\partial}{\partial Q} \hat{H}_{\text{el}} | \psi_i \rangle - \langle \psi_j | \hat{H}_{\text{el}} \frac{\partial}{\partial Q} | \psi_i \rangle = \langle \psi_j | \frac{\partial \hat{H}_{\text{el}}}{\partial Q} | \psi_i \rangle \quad . \quad (\text{H3})$$

The Hermitian operator obeys following relationship,

$$\hat{H}_{\text{el}} | \psi_i \rangle = V_{ii} | \psi_i \rangle \leftrightarrow \langle \psi_j | \hat{H}_{\text{el}}^\dagger = \langle \psi_j | \hat{H}_{\text{el}} = \langle \psi_j | V_{jj} \quad . \quad (\text{H4})$$

Thus,

$$V_{ii} \langle \psi_j | \frac{\partial}{\partial Q} | \psi_i \rangle - V_{jj} \langle \psi_j | \frac{\partial}{\partial Q} | \psi_i \rangle = \langle \psi_j | \frac{\partial \hat{H}_{\text{el}}}{\partial Q} | \psi_i \rangle \quad , \quad (\text{H5})$$

$$\langle \psi_j(r; Q) | \frac{\partial}{\partial Q} | \psi_i(r; Q) \rangle = \frac{\langle \psi_j(r; Q) | \frac{\partial \hat{H}_{\text{el}}(r; Q)}{\partial Q} | \psi_i(r; Q) \rangle}{V_{ii}(Q) - V_{jj}(Q)} \quad . \quad (\text{G1})$$

where

$$\begin{aligned} V_{ii}(Q) &= \langle \psi_j(r; Q) | \hat{H}_{\text{el}}(r; Q) | \psi_i(r; Q) \rangle \quad , \\ V_{jj}(Q) &= \langle \psi_j(r; Q) | \hat{H}_{\text{el}}(r; Q) | \psi_j(r; Q) \rangle \quad . \end{aligned}$$

References

- (1) Cao, J.; Ihee, H.; Zewail, A. H. *Proc. Natl. Acad. Sci.* **1999**, *96*, 338.
- (2) Zewail, A. H. In *Nobel Lecture*; California Institute of Technology: Pasadena, USA, 1999, p 274.
- (3) Rondonuwu, F. S.; Yokoyama, K.; Fujii, R.; Koyama, Y.; Cogdell, R. J.; Watanabe, Y. *Chem. Phys. Lett.* **2004**, *390*, 314.
- (4) Birge, R. R.; Einterz, C. M.; Knapp, H. M.; Murray, L. P. *Biophys. J.* **1990**, *53*, 367.
- (5) Hayashi, S.; Tajkhorshid, E.; Schulten, K. *Biophys. J.* **2003**, *85*, 1440.
- (6) McClung, F. J.; Hellwarth, R. W. *Appl. Opt.* **1962**, *1*, 103.
- (7) Jr., W. E. L. *Phys. Rev.* **1964**, *134*, A1429.
- (8) Hargrove, L. E.; Fork, R. L.; Pollack, M. A. *Appl. Phys. Lett.* **1964**, *5*, 4.
- (9) Hentschel, M.; Kienberger, R.; Spielmann, C.; Reider, G. A.; Milosevic, N.; Brabec, T.; Corkum, P.; Heinzmann, U.; Drescher, M.; Krausz, F. *Nature* **2001**, *414*, 509.
- (10) Paul, P.-M.; Toma, E. S.; Breger, P.; Mullot, G.; Augé, F.; Balcou, P.; Muller, H. G.; Agostini, P. *Science* **2001**, *292*, 1689.
- (11) Corkum, P. B.; Krausz, F. *Nature Phys.* **2007**, 381.
- (12) Krausz, F.; Ivanov, M. *Rev. Mod. Phys.* **2009**, *81*, 163.
- (13) Moulton, P. F. *J. Opt. Soc. Am. B* **1986**, *3*, 125.
- (14) Born, M.; Oppenheimer, R. *Annalen der Physik* **1927**, *389*, 457.
- (15) Born, M.; Huang, K. *Dynamical Theory of Crystal Lattices*; Oxford Univ. Press: London, 1954.
- (16) Domcke, W.; Köppel, H.; Cederbaum, L. S. *Mol. Phys.* **1981**, *43*, 851.
- (17) Worth, G. A.; Cederbaum, L. S. *Annu. Rev. Phys. Chem.* **2004**, *55*, 127.
- (18) Nagae, H.; Kakitani, Y.; Koyama, Y. *Chem. Phys. Lett.* **2009**, *474*, 342.
- (19) Komainda, A.; Lefrancois, D.; Dreuw, A.; Köppel, H. *Chem. Phys.* **2017**, *482*, 27.
- (20) Hudson, B. S.; Kohler, B. E. *Chem. Phys. Lett.* **1972**, *14*, 299.
- (21) Hudson, B. S.; Kohler, B. E. *Annu. Rev. Phys. Chem.* **1974**, *24*, 437.
- (22) Schaffer, H. E.; Chance, R. R.; Silbey, R. J.; Knoll, K.; Schrock, R. R. *J. Chem. Phys.* **1991**, *94*, 4161.
- (23) Orlandi, G.; Zerbetto, F. *Chem. Phys.* **1986**, *108*, 187.
- (24) Orlandi, G.; Zerbetto, F.; Zgierski, M. Z. *Chem. Rev.* **1991**, *91*, 867.
- (25) Sashima, T.; Koyama, Y.; Yamada, T.; Hashimoto, H. *J. Phys. Chem. B* **2000**, *104*, 5011.
- (26) Niedzwiedzki, D. M.; Kosciielecki, J. F.; Cong, H.; Sullivan, J. O.; Gibson, G. N.; Birge, R. R.; Frank, H. A. *J. Phys. Chem. B* **2007**, *111*, 5984.
- (27) Buckup, T.; Hauer, J.; Möhring, J.; Motzkus, M. *Arch. Biochem. Biophys.* **2009**, *483*.
- (28) Polívka, T.; Sundström, V. *Chem. Phys. Lett.* **2009**, *477*, 1.
- (29) Hunter, G. *Int. J. Quant. Chem.* **1975**, 237.
- (30) Cederbaum, L. S. *J. Chem. Phys.* **2013**, *138*, 224110.
- (31) Shreve, A. P.; Trautman, J. K.; Owens, T. G.; Albrecht, A. C. *Chem. Phys.* **1991**, *154*, 171.
- (32) Ritz, T.; Damjanović, A.; Schulten, K.; Zhang, J.-P.; Koyama, Y. *Photosynthesis Research* **2000**, *66*, 125.
- (33) Akahane, J.; rondonuwu, F. S.; Fiedor, L.; Watanabe, Y.; Koyama, Y. *Chem. Phys. Lett.* **2004**, *393*, 184.
- (34) Polívka, T.; Sundström, V. *Chem. Rev.* **2004**, *104*, 2021.
- (35) Azumi, T.; Matsuzaki, K. *Photochem. Photobiol.* **1977**, *25*, 315.
- (36) Zhang, J.-P.; Inaba, T.; Watanabe, Y.; Koyama, Y. *Chem. Phys. Lett.* **2000**, *332*, 351.
- (37) Rondonuwu, F. S.; Watanabe, Y.; Fujii, R.; Koyama, Y. *Chem. Phys. Lett.* **2003**, *376*, 292.
- (38) Cerullo, G.; Polli, D.; Lanzani, G.; Silvestri, S. D.; Hashimoto, H.; Cogdell, R. J. *Science* **2002**, *298*, 2395.
- (39) Shimada, R.; Hamaguchi, H.-o. *J Chem Phys* **2014**, *140*, 204506.
- (40) Mandal, A.; Tokmakoff, A. *J.Chem. Phys.* **2015**, *143*, 194501.

- (41) Mukamel, S. *Principles of Nonlinear Optical Spectroscopy*; Oxford University Press: New York, 1995.
- (42) Motzkus, M.; Pedersen, S.; Zewail, A. H. *J. Phys. Chem.* **1996**, *100*, 5620.
- (43) Meyer, S.; Engel, V. *J. Phys. Chem. A* **1997**, *101*, 7749.
- (44) Zou, S.; Kondorskiy, A.; Mil'nikov, G.; Nakamura, H. *J. Chem. Phys.* **2005**, *122*, 084112.
- (45) Nakamura, H. *Mol. Sci.* **2007**, *1*, A0011.
- (46) Mukamel, S.; Loring, R. F. *J. Opt. Soc. Am. B* **1986**, *3*, 595.
- (47) Backup, T.; Motzkus, M. *Annu. Rev. Phys. Chem.* **2014**, *65*, 39.
- (48) Albert, J.; Falge, M.; Gomez, S.; Sola, I. R.; Hildenbrand, H.; Engel, V. *J. Chem. Phys.* **2016**, *143*, 041102.
- (49) Koyama, Y.; Kakitani, Y.; Miki, T.; Christiana, R.; Nagae, H. *Int. J. Mol. Sci.* **2010**, *11*, 1888.
- (50) Mory, S.; Leupold, D.; König, R. *Opt. Comm.* **1972**, *6*, 394.
- (51) Penzkofer, A.; Falkenstein, W.; Kaiser, W. *Chem. Phys. Lett.* **1976**, *44*, 82.
- (52) Venkateswarlu, P.; George, M. C.; Rao, Y. V.; Jagannath, H.; Chakrapani, G.; Miahnahri, A. *Pramana J. Phys.* **1987**, *28*, 59.
- (53) Chen, W.-G.; Braiman, M. S. *Photochem. Photobiol.* **1991**, *54*, 905.
- (54) Tauler, R.; Izquierdo-Ridorsa, A.; Casassas, E. *Chemom. Intell. Lab. Syst.* **1993**, *18*, 293.
- (55) Tauler, R.; Smilde, A.; Kowalski, B. *J. Chemom.* **1995**, *9*, 31.
- (56) Yamaguchi, S.; Hamaguchi, H.-o. *J. Chem. Phys.* **1998**, *109*, 1397.
- (57) Zhang, J.-P.; Inaba, T.; Watanabe, Y.; Koyama, Y. *Chem. Phys. Lett.* **2000**, *331*, 154.
- (58) Stokkum, I. H. M. v.; Larsen, D. S.; Grondelle, R. v. *Biochim. Biophys. Acta* **2004**, *1657*, 82.
- (59) Cogdell, R. J.; Frank, H. A. *Biochemica et Biophysica Acta* **1987**, *895*, 63.
- (60) Koyama, Y.; Kuki, M.; Andersson, P. O.; Gillbro, T. *Photochem. Photobiol.* **1996**, *63*, 243.
- (61) Frank, H. A.; Chynwat, V.; Desamero, R. Z. B.; Farhoosh, R.; Erickson, J.; Bautista, J. *Pure. Appl. Chem.* **1997**, *68*, 2117.
- (62) Hofmann, E.; Wrench, P. M.; Sharples, F. P.; Hiller, R. G.; Welte, W.; Diederichs, K. *Science* **1996**, *272*, 1788.
- (63) Farhoosh, R.; Chynwat, V.; Gebhard, R.; Lugtenburg, J.; Frank, H. A. *Photosynth. Res.* **1994**, *42*, 157.
- (64) Angerhofer, A.; Bornhäuser, F.; Gall, A.; Cogdell, R. J. *Chem. Phys.* **1995**, *15*, 259.
- (65) Young, A. J.; Frank, H. A. *J. Photochem. Photobio. B* **1996**, *36*, 3.
- (66) Farhoosh, R.; Chynwat, V.; Gebhard, R.; Lugtenburg, J.; Frank, H. A. *Photochem. Photobiol.* **1997**, *66*, 97.
- (67) Ermakov, I. V.; Sharifzadeh, M.; Ermakova, M.; Gellermann, W. *J. Biomed. Opt.* **2005**, *10*, 064028.
- (68) Foote, C. S.; Denny, R. W. *J. Am. Chem. Soc.* **1968**, *90*, 6233.
- (69) Gregory, A. R.; Siebrand, W.; Zgierski, M. Z. *J. Chem. Phys.* **1976**, *64*, 3145.
- (70) Koyama, Y. In *Carotenoids, Vol. 1B: Spectroscopy*; Britton, G., Liaaen-Jensen, S., Pfander, H., Eds.; Birkhäuser: Basel, 1995, p 135.
- (71) Frank, H. A.; Christensen, R. L. In *The Carotenoids, vol 4: Natural Functions*; Britton, G., Liaaen-Jensen, S., Pfander, H., Eds.; Birkhauser Verlag: Basle, 2008, p 167.
- (72) Hashimoto, H.; Koyama, Y. *Chem. Phys. Lett.* **1989**, *162*, 523.
- (73) Hashimoto, H.; Koyama, Y. *Chem. Phys. Lett.* **1989**, *163*, 251.
- (74) Tavan, P.; Schulten, K. *J. Chem. Phys.* **1986**, *85*, 6602.
- (75) Furuichi, K.; Sashima, T.; Koyama, Y. *Chem. Phys. Lett.* **2002**, *356*, 547.
- (76) Tavan, P.; Schulten, K. *Phys. Rev. B* **1987**, *36*, 4337.
- (77) Kleinschmidt, M.; Marian, C. M.; Waletzke, M.; Grimme, S. *J. Chem. Phys.* **2009**, *130*, 044708.
- (78) Schulten, K.; Karplus, M. *Chem. Phys. Lett.* **1972**, *14*, 305.
- (79) Pariser, R. *J. Chem. Phys.* **1956**, *24*, 250.
- (80) Callis, P. R.; Scott, T. W.; Albrecht, A. C. *J. Chem. Phys.* **1983**, *78*, 16.
- (81) Shreve, A. P.; Trautman, J. K.; Owens, T. G.; Albrecht, A. C. *Chem. Phys. Lett.* **1991**, *178*, 89.
- (82) Kandori, H.; Sasabe, H.; Mimuro, M. *J. Am. Chem. Soc.* **1994**, *116*, 2671.

- (83) Andersson, P. O.; Gillbro, T. *J. Chem. Phys.* **1995**, *103*, 2509.
- (84) Wasielewski, M. R.; Kispert, L. D. *Chem. Phys. Lett.* **1986**, *128*, 238.
- (85) Abramavicius, D.; Palmieri, B.; Voronine, D. V.; Šanda, F.; Mukamel, S. *Chem. Rev.* **2009**, *109*, 2350.
- (86) Zhang, Q.; Kandel, S. A.; Wasserman, T. A. W.; Vaccaro, P. H. *J. Chem. Phys.* **1992**, *96*, 1640.
- (87) Hauer, J.; Backup, T.; Motzkus, M. *J. Phys. Chem. A* **2007**, *111*, 10517.
- (88) Ruhman, S.; Hou, B.; Friedman, N.; Ottolenghi, M.; Sheves, M. *J. Am. Chem. Soc.* **2002**, *124*, 8854.
- (89) Bismuth, O.; Komm, P.; Friedman, N.; Eliash, T.; Sheves, M.; Ruhman, S. *J. Phys. Chem. B* **2010**, *114*, 3046.
- (90) Kraack, J. P.; Backup, T.; Motzkus, M. *Phys. Chem. Chem. Phys.* **2012**, *14*, 13979.
- (91) Ostroumov, E. E.; Müller, M. G.; Marian, C. M.; Kleinschmidt, M.; Holzwarth, A. R. *Phys. Rev. Lett.* **2009**, *103*, 108302.
- (92) Kakitani, Y.; Miki, T.; Koyama, Y.; Nagae, H.; Nakamura, R.; Kanematsu, Y. *Chem. Phys. Lett.* **2009**, *477*, 194.
- (93) Miki, T.; Backup, T.; Krause, M. S.; Southall, J.; Cogdell, R. J.; Motzkus, M. *Phys. Chem. Chem. Phys.* **2016**, *18*, 11443.
- (94) Orlandi, G.; Siebrand, W. *Chem. Phys. Lett.* **1972**, *15*, 465.
- (95) Herzberg, G.; Teller, E. In *Zeitschrift für physikalische Chemie. Abteilung B, Chemie der Elementarprozesse, Aufbau der Materie 21 (5/6)*, Akademische Verlagsgesellschaft: Leipzig, 1933.
- (96) Koyama, Y.; Kubo, K.; Komori, M.; Yasuda, H.; Mukai, Y. *Photochem. Photobiol.* **1991**, *54*, 433.
- (97) Marek, M. S.; Backup, T.; Motzkus, M. *J. Phys. Chem. B* **2011**, *115*, 8328.
- (98) Marek, M. S.; Backup, T.; Southall, J.; Cogdell, R. J.; Motzkus, M. *J Chem Phys* **2013**, *139*, 074202.
- (99) Kraack, J. P.; Backup, T.; Motzkus, M. *J. Phys. Chem. Lett.* **2013**, *4*, 383.
- (100) Lenzer, T.; Ehlers, F.; Scholz, M.; Oswald, R.; Oum, K. *Phys. Chem. Chem. Phys.* **2010**, *12*, 8832.
- (101) Ehlers, F.; Scholz, M.; Schimpfhauser, J.; Bienert, J.; Oum, K.; Lenzer, T. *Phys. Chem. Chem. Phys.* **2015**, *17*, 10478.
- (102) Kraack, J. P.; Motzkus, M.; Backup, T. *J. Chem. Phys.* **2011**, *135*, 224505.
- (103) Rondonuwu, F. S.; Watanabe, Y.; Zhang, J.-P.; Furuichi, K.; Koyama, Y. *Chem. Phys. Lett.* **2002**, *357*, 376.
- (104) Rondonuwu, F. S.; Kakitani, Y.; Tamura, H.; Koyama, Y. *Chem. Phys. Lett.* **2006**, *429*, 234.
- (105) Hayashi, H.; Noguchi, T.; Tasumi, M.; Atkinson, G. H. *Biophys. J.* **1991**, *60*, 252.
- (106) Kraack, J. P.; Wand, A.; Backup, T.; Motzkus, M.; Ruhman, S. *Phys. Chem. Chem. Phys.* **2013**, *15*, 14487.
- (107) Mielke, S. L.; Schwenke, D. W.; Schatz, G. C.; Garrett, B. C.; Peterson, K. A. *J. Phys. Chem. A* **2009**, *113*, 4479.
- (108) Feynman, R. P. *Phys. Rev.* **1939**, *56*, 340.
- (109) Herrick, D. R. *J. Chem. Phys.* **1981**, *74*, 1239.
- (110) Nagae, H.; Kuki, M.; Zhang, J.-P.; Sashima, T.; Mukai, Y.; Koyama, Y. *J. Phys. Chem. A* **2000**, *104*, 4155.
- (111) Andersson, P. O.; Gillbro, T.; Ferguson, L.; Cogdell, R. J. *Photochem. Photobiol.* **1991**, *54*, 353.
- (112) Maiuri, M.; Polli, D.; Brida, D.; Luer, L.; LaFountain, A. M.; Fuciman, M.; Cogdell, R. J.; Frank, H. A.; Cerullo, G. *Phys. Chem. Chem. Phys.* **2012**, *14*, 6312.
- (113) Ostroumov, E. E.; Müller, M. G.; Hundsdörfer, C.; Stahl, W.; Marian, C. M.; Holzwarth, A. R. *Chem. Phys.* **2010**, *373*, 137.
- (114) Hauer, J.; Backup, T.; Motzkus, M. *J. Chem. Phys.* **2006**, *125*, 061101.
- (115) Hauer, J.; Skenderovic, H.; Kompa, K.-L.; Motzkus, M. *Chem. Phys. Lett.* **2006**, *421*, 523.
- (116) Kakitani, Y.; Fujii, R.; Koyama, Y.; Nagae, H.; Walker, L.; Salter, B.; Angerhofer, A. *Biochemistry* **2006**, *45*, 2053.

- (117) Eckbreth, A. C. *Appl. Phys. Lett.* **1978**, 32, 421.
- (118) Kubin, R. F.; Fletcher, A. N. *J. Lumine.* **1982**, 27, 455.
- (119) Hildebrandt, P.; Stockburger, M. *J. Phys. Chem.* **1984**, 88, 5935.
- (120) Smith, B. C. *Infrared Spectral Interpretation: A Systematic Approach*; CRC Press: New York, 1998.
- (121) Koyama, Y.; Miki, T.; Wang, X.-F.; Nagae, H. *Int. J. Mol. Sci.* **2009**, 10.
- (122) Boeij, W. P. d.; Pshenichnikov, M. s.; Wiersma, D. A. *Chem. Phys. Lett.* **1996**, 253, 53.
- (123) Boeij, W. P. d.; Pshenichnikov, M. s.; Wiersma, D. A. *Annu. Rev. Phys. Chem.* **1998**, 49, 99.
- (124) Ballhausen, C. J.; Hansen, A. E. *Annu. Rev. Phys. Chem.* **1972**, 23, 15.
- (125) Smith, F. T. *Phys. Rev.* **1969**, 179, 111.
- (126) Mead, C. A.; Truhlar, D. G. *J. Chem. Phys.* **1982**, 77, 6090.
- (127) Narva, D. L.; McClure, D. S. *Chem. Phys.* **1975**, 11, 151.
- (128) Duschinsky, F. *Acta Physicochimica U.R.S.S.* **1937**, 7, 551.
- (129) Baer, M. *Chem. Phys. Lett.* **1975**, 35, 112.
- (130) Lichten, W. *Phys. Rev.* **1963**, 131, 229.
- (131) Negri, F.; Orlandi, G.; Zerbetto, F.; Zgierkski, M. Z. *J. Chem. Phys.* **1989**, 91, 6215.

List of Scientific Contributions since 2011

Articles in Scientific Journals

Vibronic coupling in the excited-states of carotenoids

Takeshi Miki, Tiago Buckup, Marie S. Krause, June Southall, Richard J. Cogdell and Marcus Motzkus, *Phys. Chem. Chem. Phys.*, **18** (2016) 11443 – 11453

Multimodal Time-Resolved Spectroscopy: Combining Pump-probe and pump-degenerate Four-wave Mixing Experiments

Takeshi Miki, Marcus Motzkus, and Tiago Buckup, *in preparation*

Contributions in Conference Talk

Ultrafast Interaction of Dark and Bright Electronic States in Open-Chain Carotenoids Investigated by Pump-DFWM

Takeshi Miki, Tiago Buckup, Marie Marek, Richard Cogdell, and Marcus Motzkus, International Conference on Ultrafast Phenomena 2014

Ultrafast coupling dynamics between the excited states of open chain carotenoids observed by fs time-resolved nonlinear vibrational spectroscopy

Takeshi Miki, Richard J. Cogdell, Tiago Buckup, and Marcus Motzkus, Frühjahrstagung der Deutschen Physikalischen Gesellschaft (79th Annual Meeting and Spring Meeting of the German Physical Society), Heidelberg, March 2015

Multimodal Time-Resolved Spectroscopy of Vibrational Coherence and Population Dynamics in the Excited State

Takeshi Miki, Marcus Motzkus, and Tiago Buckup, Frühjahrstagung der Deutschen Physikalischen Gesellschaft (80th Annual Meeting and Spring Meeting of the German Physical Society), Hannover, March 2016

Contributions in Poster Presentations

Open chain carotenoids with $N = 9 - 13$ conjugated double bonds studied by multidimensional spectroscopy

Takeshi Miki, Marie S.Marek, Tiago Buckup, and Marcus Motzkus, Frühjahrstagung der Deutschen Physikalischen Gesellschaft (77th Annual Meeting and Spring Meeting of the German Physical Society), Hannover, March 2013

Multimodal Time-Resolved Spectroscopy: Combining Transient Absorption and Fifth-order Spectroscopies

Takeshi Miki, Marcus Motzkus and Tiago Buckup, Frühjahrstagung der Deutschen Physikalischen Gesellschaft (79th Annual Meeting and Spring Meeting of the German Physical Society), Heidelberg, March 2015

Acknowledgements

Here, I would like to express my acknowledgement for the people who have supported, helped and encouraged me during my study in Germany.

I would like to thank Prof. Dr. Marcus Motzkus for providing me the opportunity and wonderful environments for my PhD study. His great breadth of mind and thorough instructions allow me to grow up as a scientist. He has always encouraged me by preparing the best environment of the research. Especially, the investments on the chemical laboratory allow me to extract and to purify carotenoids which are the principal samples in my research. The extremely nice laser system always provides wonderful data with high resolutions. In addition, the opportunities to attend (inter-)national conferences inspired me to proceed the projects. I am really happy that I can work in his group.

I would like to appreciate Prof. Dr. Andreas Dreuw for accepting this work as a co-supervisor.

I am sincerely grateful to Dr. Tiago Buckup for giving great instructions of multi-pulse optical techniques, relevant theories and the things which were necessary to proceed the research projects on the correct direction. Although many of discussions in the mathematics and chemical theories were tough topics, his supports were essential to develop the research. I have learned many of the technique and knowledge from him during my PhD study. In addition, it was great help to prepare my living environment in the beginning of the study in Germany. I am sure that all pieces of the studies will be great treasures in my life.

Prof. Dr. Hiroyoshi Nagaie has personally supervised me about the quantum mechanics from my bachelor study. Many discussions on theories and mathematics led to the innovative idea in my research. I hope I could continue to learn from him and hand the knowledge to the next generation.

Prof. Dr. Richard J. Cogdell has also supported me since my bachelor study for the sample preparation. The purple bacteria, which are well-characterized and kept in high purity in his group, are the principal samples in the research of the photosynthesis.

Prof. Dr. Hans-Robert Volpp motivated me by giving critical questions and interesting comments in seminars. Especially, the safety instructions in English were very helpful, and I didn't get injured during the research in Germany.

Klaus Schmitt and his team (Heidelberg) from the mechanics workshop support us by their excellent works to make a metallic connector of the optical experiment. Their work will be used in our laboratory.

Secretaries Sylvia Boganski, Angelika Neuner and Annette Lischer always supported me to prepare documents for the research activities and to stay in Germany. Especially, Frau. Boganski managed many documents before my coming to German.

Mr. Gerhard Kryzer and the team (Hausing and facility management, Heidelberg) have helped me a lot to stay in student house and to fix some broken things.

My special thanks to all my colleagues from the Motzkus group.

The members working in 152 lab, Dr. Marie S. Krause (Marek), Dr. Jan Philip Kraack, Dr. Julia Herz, Partha Pratim Roy, Andreas Ludwig are really excellent people. Marie helped me a lot about the carotenoid project, by introducing the laser system and the measurement programs. Philip supported me not only in the experiments but also many discussions about my questions. He was an excellent roommate. Julia helped me a lot by giving advice on the research and turning on the laser early in the morning. The group traveling and other events that she prepared were great memories for me. Partha and Andreas are great members for the FWM projects. I am sure that their excellent techniques to manage the measurements will be fruitful in the research.

The previous members, Dr. Lukas Brückner, Jiang Man (JJ), Dr. Alexander Wipfler, Dr. Christoph Pohling, Dzmitry Starukhin, Dr. Alex Duarte, Dr. Jean Rehbinder, Dr. Hrvoje Skenderovic, Dr. Jens Möhring and Ellen Bruce always supported me when I had some problems. Lukas and JJ were great colleague who encouraged me a lot to write the thesis. Alex and Christoph supported me to register in the city office and write other social documents. Jean, Dzmitry and Alex are wonderful friends to enjoy the life in the university. The current members, Elisabeth Brühl, Partha Pratim Roy, Dr. Nicholas Paul supported me to finish my thesis by checking my English in great detail, giving nice instructions and encouraging me a lot. I am sure that their helps greatly improved my English proficiency. In addition, it was a great pleasure to learn from their interesting projects in seminars and conferences.

Finally, I am very grateful to my parents and my brothers for their understanding, encouragement, supports and patience.

Eidesstattliche Erklärung

Ich erkläre hiermit, dass bei der vorliegenden Dissertation handelt es sich um meine eigenständig erbrachte Leistung. Ich habe nur die angegebenen Quellen und Hilfsmittel benutzt und mich keiner unzulässigen Hilfe Dritter bedient. Insbesondere habe ich wörtlich oder sinngemäß aus anderen Werken übernommene Inhalte als solche kenntlich gemacht.

Diese Dissertation wurde im Sinne der "Promotionsordnung der Universität Heidelberg für die Naturwissenschaftlich-Mathematische Gesamtfakultät" ab 01. August 2011 von Prof. Dr. Marcus Motzkus betreut.

Heidelberg, 11.04.2017

Takeshi Miki

Lebenslauf

Persönliche Daten

Name: Takeshi Miki
Geburtsdatum: 30.03.1984
Geburtsort: Yamaguchi (Japan)
Anschrift: Kikari 3-15-8, Inzai-shi, 270-1359 Chiba-ken, Japan
Nationalität: Japanisch

Studium

08/2011 - PhD study in Chemistry, Heidelberg University, Heidelberg (Germany)
04/2006 - 03/2008 M.S. in Chemistry, Kwansei Gakuin University, Hyogo (Japan)
04/2002 - 03/2006 B.S. in Chemistry, Kwansei Gakuin University, Hyogo (Japan)

**Eidesstattliche Versicherung gemäß § 8 der Promotionsordnung
der Naturwissenschaftlich-Mathematischen Gesamtfakultät
der Universität Heidelberg**

1. Bei der eingereichten Dissertation zu dem Thema

Third- and Fifth-order Nonlinear Time-resolved
Spectroscopies for Ultrafast Molecular Dynamics
in Carotenoids

handelt es sich um meine eigenständig erbrachte Leistung.

2. Ich habe nur die angegebenen Quellen und Hilfsmittel benutzt und mich keiner unzulässigen Hilfe Dritter bedient. Insbesondere habe ich wörtlich oder sinngemäß aus anderen Werken übernommene Inhalte als solche kenntlich gemacht.

3. Die Arbeit oder Teile davon habe ich wie folgt/bislang nicht¹⁾ an einer Hochschule des In- oder Auslands als Bestandteil einer Prüfungs- oder Qualifikationsleistung vorgelegt.

Titel der Arbeit: _____

Hochschule und Jahr: _____

Art der Prüfungs- oder Qualifikationsleistung: _____

4. Die Richtigkeit der vorstehenden Erklärungen bestätige ich.

5. Die Bedeutung der eidesstattlichen Versicherung und die strafrechtlichen Folgen einer unrichtigen oder unvollständigen eidesstattlichen Versicherung sind mir bekannt.

Ich versichere an Eides statt, dass ich nach bestem Wissen die reine Wahrheit erklärt und nichts verschwiegen habe.

Heidelberg, 20.04.2017
Ort und Datum

Yasuhiko Miki
Unterschrift

¹⁾ Nicht Zutreffendes streichen. Bei Bejahung sind anzugeben: der Titel der andernorts vorgelegten Arbeit, die Hochschule, das Jahr der Vorlage und die Art der Prüfungs- oder Qualifikationsleistung.